

A Two-Stage Rotary Blood Pump Design to Reduce Blood Trauma

vorgelegt von
Bente Kristina Thamsen,
M.Sc.
geb. in Braunschweig

von der Fakultät V – Verkehrs- und Maschinensysteme
der Technischen Universität Berlin
zur Erlangung des akademischen Grades

Doktor der Ingenieurwissenschaften
- Dr.-Ing. -

genehmigte Dissertation

Promotionsausschuss:

Vorsitzender: Prof. Dr.-Ing. Marc Kraft
Gutachter: Prof. Dr.-Ing. C. Oliver Paschereit
Prof. Dr.-Ing. Klaus Affeld
Prof. Dr. rer. medic. Tim A. S. Kaufmann

Tag der wissenschaftlichen Aussprache: 4. Juli 2016

Berlin 2016

Acknowledgements

This thesis developed during my time as a research associate in the Biofluid Mechanics Laboratory of the Charité – Universitätsmedizin Berlin. I am very grateful to Prof. Dr.-Ing. Klaus Affeld and Dr.-Ing. Ulrich Kertzsch for giving me the opportunity to join their working group. Without Prof. Affeld's pioneering and innovative ideas this project would not have been possible and his assistant advice was greatly appreciated. Ulrich Kertzsch helped me with his caring support, encouragement and guidance.

Furthermore, I would like to thank Prof. Dr.-Ing. Christian Oliver Paschereit for his support and cooperativeness in conducting this thesis.

Many warm thanks go to all my colleagues and the students from the Biofluid Mechanics Laboratory for an always friendly, collegial and constructive atmosphere. Fruitful discussions with the other research associates and technical staff and their willingness to support me made this work possible. I am also grateful for the active and dedicated support of my students and student coworkers.

From the working group of Prof. Paschereit, I want to thank Bastian Blümel for his effort and enthusiasm.

To the team of the department of fluid system dynamics at the Technische Universität Berlin I owe gratitude for their great hospitality and helpfulness during the concept and experimental phase of this project.

Further thanks I want to express to my project partners for a constructive and reliable collaboration: In particular, Friedrich Kaufmann and his team from the Deutsches Herzzentrum Berlin who provided the explanted rotary blood pumps and assistance from the clinical perspective, and David Busch and his colleagues from the DUALIS MedTech GmbH who aided in the manufacturing of the prototype.

Last but not least, I am deeply grateful to my family and friends for their support and their belief in me. Especially, my father without whom I would have never taken this path, and who provided me with guiding advice and assistance on my way, and my boyfriend, who has been very supportive during the development process of this thesis.

Abstract

Currently used ventricular assist devices (VADs) are implantable miniature centrifugal pumps, referred to as rotary blood pumps. Survival rates with these devices increased substantially during the last decades. Nevertheless, despite extensive research and new technologies the clinical benefit of such systems is still limited due to a high incidence of severe adverse events. Frequent serious complications observed in VAD patients are strokes, infections, pump thrombosis, and bleeding. A major part of the complications can be linked to blood trauma induced by the devices. Important factors for blood damage are flow characteristics inside these pumps, the particular flow patterns, and shear stress levels. Thus, the aim of this thesis was to investigate the flow in clinical rotary blood pumps experimentally and numerically to provide insights into the major causes of blood damage. Based on these findings, a new less traumatic rotary blood pump design was developed.

This thesis includes three publications: two papers deal with the flow characteristics in established rotary blood pumps. In the third paper a less traumatic rotary blood pump design is presented and compared to the previously investigated pumps.

In a first step, computational fluid dynamics (CFD) was utilized to compare the two most widely used rotary blood pumps: the axial HeartMate II pump and the radial Heartware HVAD pump. The flow fields were simulated for one typical state of operation and analyzed, especially regarding potential blood trauma. Since blood damage is connected to high shear stresses, volumetric proportions exposed to different shear stress levels were calculated. Furthermore, a hemolysis index based on a revised Eulerian transport approach was computed. **(Paper I)**

Second, flow measurement and visualization methods were used to investigate the flow inside the HeartMate II. An experimental setup with an upscaled model was built which was optically accessible. The wall Particle Image Velocimetry (wall-PIV) method was employed for flow measurements close to the outer wall while the paint erosion method gave insight into flow patterns on the inner surfaces of pump components. Overall good agreement of CFD and experimental results was observed and critical regions with regard to blood damage and thrombus formation were identified. **(Paper II)**

The final objective of this thesis was to develop and investigate a novel pump design with decreased shear stresses to reduce blood trauma. For this purpose, a two-stage pump design was introduced. By using two diagonal stages, lower circumferential velocities compared to the two established blood pumps were possible which led to lower shear stresses as shown by CFD. This reduces blood trauma and might therefore decrease the likelihood of adverse events in VAD patients. **(Paper III)**

Kurzfassung

Moderne Herzunterstützungssysteme (engl.: ventricular assist devices (VADs)) sind kleine, implantierbare Kreislumpen. Die Überlebensraten mit diesen Geräten sind während der letzten Jahrzehnte erheblich gestiegen. Trotz umfangreicher Forschung und neuer Technologien ist der klinische Nutzen dieser Systeme jedoch durch eine hohe Inzidenz von Komplikationen begrenzt. Zu den häufigsten Komplikationen von VAD-Patienten zählen Schlaganfälle, Infektionen, Pumpenthrombosen und Blutungen. Ein Großteil dieser Komplikationen kann mit einer durch die Pumpen verursachten Blutschädigung in Zusammenhang gebracht werden. Dies wird vor allem durch die bestimmte Strömungsstrukturen und hohe Schubspannungsniveaus in der Pumpenströmung verursacht. Folglich war es das Ziel dieser Arbeit, die Strömung in Herzunterstützungspumpen experimentell und numerisch zu untersuchen, um die Hauptursachen für die Blutschädigung zu identifizieren. Basierend auf diesen Ergebnissen wurde eine neue, weniger schädigende Blutpumpe entwickelt.

Es werden drei Publikationen präsentiert, welche die Strömungseigenschaften von klinisch etablierten Blutpumpen untersuchen und ein blutschonenderes Pumpenkonzept beschreiben.

Im ersten Schritt wurden die zwei klinisch am häufigsten implantierten Blutpumpen mit Hilfe numerischer Simulation verglichen: die HeartMate II (HM II) und das Heartware HVAD. Die Pumpenströmungen wurden für einen typischen Betriebspunkt simuliert und besonders im Hinblick auf eine mögliche Blutschädigung analysiert. Da diese von der Höhe der Schubspannungen abhängt, wurden Volumenanteile, die bestimmten Schubspannungsbereichen ausgesetzt sind, berechnet. Außerdem wurde ein Hämolyse-Index basierend auf einem weiterentwickelten Eulerschen Transportansatz ermittelt. (**Paper I**)

Als Zweites wurden Methoden der Strömungsmesstechnik und -sichtbarmachung eingesetzt, um die Strömung in der HM II zu untersuchen. Dafür wurde ein experimenteller Aufbau mit einem vergrößerten, optisch zugänglichen Modell der Pumpe entwickelt. Mit dem Wand-Particle Image Velocimetry (PIV)-Verfahren wurde die Strömung nahe der äußeren Gehäusewand erfasst, während das Farbanstrichverfahren Einblicke in die Strömung auf der Oberfläche der inneren Pumpenkomponenten lieferte. Dabei wurde eine gute Übereinstimmung von experimentellen und numerischen Ergebnissen beobachtet und es konnten kritische Regionen für Blutschädigung und Thrombenbildung identifiziert werden. (**Paper II**)

Das abschließende Ziel dieser Dissertation war die Entwicklung und Untersuchung eines neuen Pumpenkonzepts mit reduzierten Schubspannungen zur Verringerung von Blutschädigung. Dies konnte mit dem Konzept einer zweistufigen halbaxialen Pumpe erreicht werden, bei der der nötige Druckaufbau auf die einzelnen Stufen verteilt wird, sodass geringere Umfangsgeschwindigkeiten möglich waren. Auf diese Weise wurden die Schubspannungen in der Pumpe reduziert, wodurch folglich die Blutschädigung verringert und möglicherweise die Wahrscheinlichkeit für Komplikationen bei VAD-Patienten verringert wird. (**Paper III**)

Table of contents

1	Introduction.....	1
1.1	The cardiovascular system	1
1.1.1	The heart and the circulation.....	1
1.1.2	Cardiac failure.....	4
1.2	Implantable rotary blood pumps.....	6
1.2.1	The Thoratec HeartMate II.....	8
1.2.2	The HeartWare HVAD.....	9
1.2.3	New rotary blood pump technologies	10
1.3	Blood properties	11
1.4	Blood damage in rotary blood pumps	13
1.4.1	Damage of erythrocytes	13
1.4.2	Effects on platelets.....	14
1.4.3	Degradation of von Willebrand factor.....	15
1.5	The fluid mechanics principles of rotary blood pumps	16
1.6	Experimental methods to investigate rotary blood pumps	21
1.6.1	Similarity laws	21
1.6.2	The wall-PIV measurement technique.....	21
1.6.3	The paint erosion method.....	23
1.6.4	Measurement of characteristic curves	24
1.7	Computational fluid dynamics in rotary blood pumps	26
1.7.1	Mesh generation	26
1.7.2	Numerical simulation of flow in rotating regions	27
1.7.3	Modeling turbulence.....	27
1.7.4	Modeling blood trauma.....	29
1.8	Aim of this thesis.....	31
2	Publications.....	32
2.1	Paper I: Numerical Analysis of Blood Damage Potential of the HeartMate II and HeartWare HVAD Rotary Blood Pumps.....	32
2.2	Paper II: Experimental and numerical investigation of an axial rotary blood pump.....	42
2.3	Paper III: A two-stage rotary blood pump design with potentially lower blood trauma: a computational study.....	54
3	Discussion	61
3.1	Investigation of established pumps	61
3.1.1	Shear stresses, platelet activation and blood trauma.....	61
3.1.2	Flow patterns and thrombosis	63
3.1.3	Critical view on the used methods.....	65
3.2	A design for a less-traumatic rotary blood pump	66
3.2.1	Possible configurations.....	68
3.2.2	Pump design.....	70
3.2.3	Operating behavior.....	72

3.2.4	The bearing concept.....	74
3.2.5	Manufacturability	76
3.2.6	Efficiency	76
3.2.7	Blood trauma in the two-stage pump	77
3.3	Summary and outlook.....	78
References	79
List of figures	86
List of tables	89

1 Introduction

Heart failure is a major cause of death in developed countries. During the last decades, ventricular assist devices (VADs) have become an established therapy for patients suffering from heart failure. Mainly, these are small centrifugal pumps that are implanted into the patient's body to assist the failing heart. In the field of medicine and biomedical engineering these pumps are commonly referred to as rotary blood pumps. Although survival rates with rotary blood pumps improved substantially compared to earlier pulsatile devices and reached 85 % during the first year after implantation (see section 1.2), serious complications related to the non-physiological flow conditions within these pumps remain a major issue. In particular, high shear stresses caused by the high circumferential velocities of the rotating impeller in combination with small gaps to the housing wall lead to blood damage. Thus, the aim of this thesis was to investigate current rotary blood pumps and identify related flow characteristics and shear stress levels. On this basis, a two-stage pump design was suggested that allows for a reduction of circumferential velocities compared to single-stage pumps and is therefore less traumatic.

In the first part of this thesis, an overview of the cardiovascular system is given. Furthermore, the state-of-the-art rotary blood pumps are described and the topic blood damage is introduced. A brief description of methods used to investigate the flow inside established blood pumps leads over to the second part, where three publications that were published in the framework of this thesis are presented. Finally, a discussion of the achieved results follows and a conclusion is drawn.

1.1 The cardiovascular system

The cardiovascular system transports nutrients and waste products as well as hormones inside the body. The main drive is the heart that pumps the blood through the circulation.

1.1.1 The heart and the circulation

The heart is a muscular pumping organ which consists of two pulsatile pumps that work in series: the left ventricle pushes blood through the systemic circulation and the right ventricle serves the pulmonary circulation [1]. Pressure levels on the two sides are different: The same amount of blood needs to overcome the high systemic resistance resulting in high pressures in the left ventricle, whereas the low pulmonary resistance requires low pressures in the right ventricle.

Because of the difference in pressure, the anatomy of the left and right hand side of the heart consequently differ, however, the working principle is the same:

Blood returned to the heart by the lung and body is stored by the atria and forwarded to the ventricles during the filling phase, the diastole. This happens when the pressure in the ventricle

drops below the atrium's level, so that the atrioventricular valves open. The atrioventricular valve in the left ventricle is called mitral valve and the corresponding valve in the right ventricle is called tricuspid valve. At the end of the diastole, the atria contract and transmit more blood into the ventricles. During the following contraction phase, the systole, the ventricles contract so that ventricular pressure increases and the atrioventricular valves close. When the pressure in the ventricles exceeds the pressure in the aorta and the pulmonary artery respectively, the aortic valve and the pulmonary valve open leading blood into the aorta and the pulmonary artery.

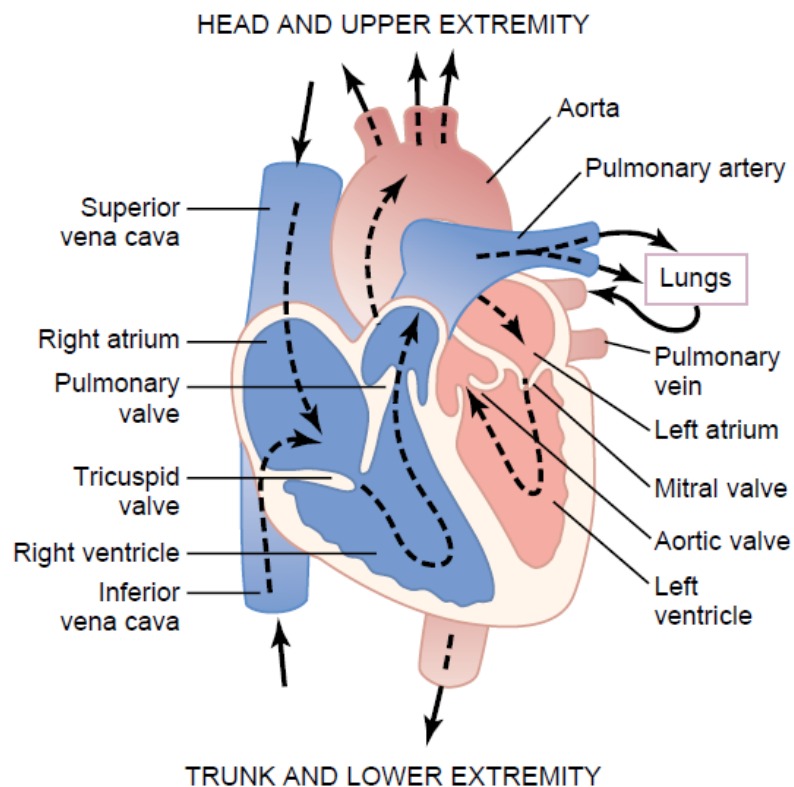


Figure 1: Schematic overview of the heart with the left and right ventricles and atria, the four valves and major vessels [1]. The direction of the blood flow is indicated as well: Blood from the body returns to the right heart through the vena cava, is then pumped through the lung to the left heart and further pumped into the aorta back to the tissues.

The time course of the pressure in the left atrium and ventricle and in the aorta through the cardiac cycle is shown in Figure 2 along with the left ventricular volume and the electric as well as acoustic signals of the heart which can be detected. The moments when the valves open are indicated as well.

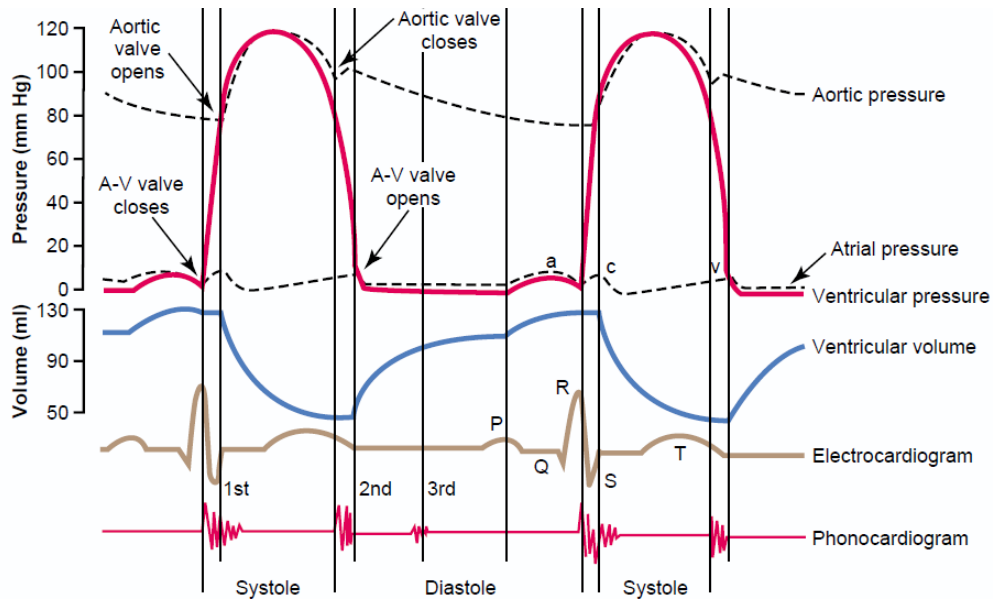


Figure 2: Time courses of pressures and volumes of the left heart and aorta during two cardiac cycles [1]. At the end of diastole, the atria contract and transmit the rest of blood into the ventricles. During systole, the ventricles contract so that the atrioventricular (A-V) valve closes and pressure increases. When pressures are high enough, the aortic valve opens and blood flows into the aorta until the aortic pressure exceeds the ventricular pressure and the aortic valve closes. After that the ventricle relaxes and diastole begins again. The electrocardiogram (ECG) and heart tones are also shown.

The circulation system is composed of different types of vessels with different tasks. In general, arteries transport blood away from the heart, while veins return blood to the heart. The course of pressure through the different parts of the circulation system is shown in Figure 3. In the arterial system there is a high pressure while the venous system is a low pressure system. The aorta with its compliance functions like a “Windkessel” that serves as a high pressure blood reservoir and stores about 50 % of the stroke volume in systole [2]. During diastole, the elastic forces of the arterial wall forward the blood volume to the periphery so that blood flow in the arteries is continuous through the entire cardiac cycle. Moreover, the pressure in the arterial system drops down to values around 80 mmHg during diastole in healthy humans.

Due to the high pressures in the arteries these vessels have stronger vascular walls and blood is transported at high velocities. The arteries further subdivide into the arterioles which have diameters between 10 to 15 μm and strong muscular walls giving them the capability to control blood flow through the tissues by contracting. In the capillaries, the exchange of nutrients, electrolytes, hormones and other substances takes place. Therefore, capillaries are very thin with diameters of 5 to 9 μm and have permeable walls. Deoxygenated blood from the capillaries is collected by the venules and forwarded to progressively larger veins which lead back to the heart. The thin walls of the veins are muscular to adjust the venous reservoir to the needs of the circulation [3,4].

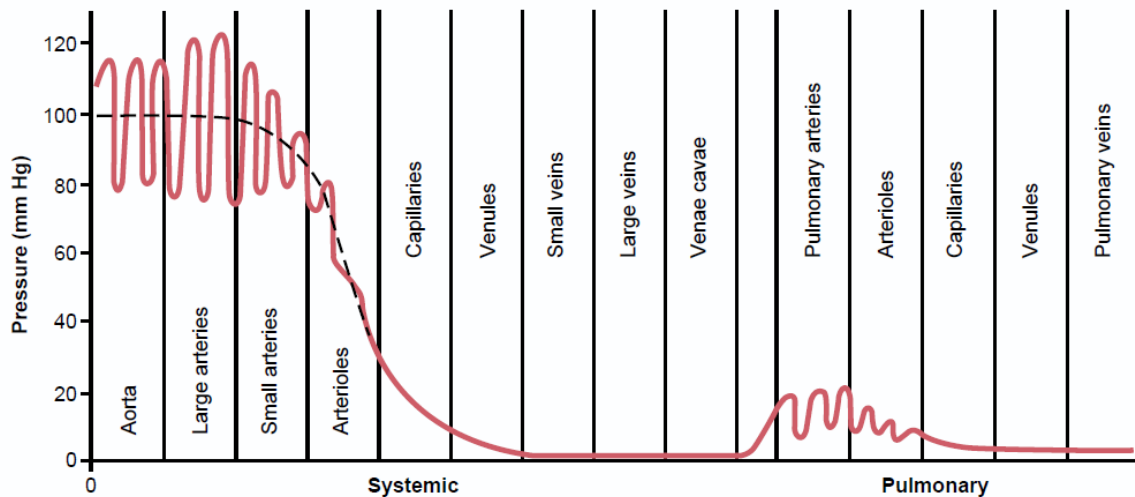


Figure 3: Normal blood pressures in the circulation [3]. Pressures in the aorta and large and small arteries are high and pulsatile between 80-120 mmHg, falling to much lower and non-pulsatile pressures in capillaries and veins. The pulmonary arteries leaving the right heart have pulsatile low pressure in the range of 10-20 mmHg.

Depending on the function, the vessel wall is differently composed. All vessels are lined by endothelium which are flattened cells that form a smooth inner layer [5]. The endothelium is not a passive membrane between blood flow and other tissue, but interacts with the blood and participates in processes like thrombosis or inflammation [6].

Further structural components of the vessel walls are collagen fibers which give strength to the vessel wall, elastin fibers which are highly elastic and stretch more than 100 %, and smooth muscle tissue, which is found to a lesser or greater extent in all vessels except for capillaries. The smooth muscle lining allows the vessels to contract [5].

1.1.2 Cardiac failure

Cardiac failure or heart failure is an abnormality of the heart's structure and function leading to an undersupply of the tissues with oxygen and nutrients [7]. Heart failure may follow a sudden event like a myocardial infarction or may be a consequence of a chronic degradation of cardiac function. It can be divided into two types: diastolic heart failure which is the impaired filling of the heart, and systolic failure which is the impaired discharging of the heart. The differentiation of these and the classification of severity of systolic heart failure is based on the ventricular ejection fraction – the stroke volume divided by the end-diastolic ventricular volume. While a normal ejection fraction is between 60 to 80 %, systolic heart failure is characterized by an ejection fraction of less than 40 % [7].

For instance, an aortic insufficiency might be the underlying cause of a systolic heart failure. In that case, the aortic valve is not sufficiently closed during diastole and blood from the aorta is flowing back to the ventricle. In order to compensate the volume overload and subsequent

higher pressure during diastole the ventricular diameter increases. This dilatation of the heart is stimulated by an elevated cardiac wall tension which can be described by the law of Laplace:

$$\sigma \propto \frac{p \cdot r}{s} \quad \text{Eq. 1}$$

Although this law captures the circumstances in a sphere, it can be adapted for the ventricle and explains that the wall tension σ rises when the radius r increases. Subsequently, in typical dilated cardiomyopathy patients, the wall thickness s decreases leading to even higher wall tension and dilation of the heart is further stimulated. Altogether, compensatory mechanisms in heart failure lead to an increased workload of the heart so that progression and decompensation may occur [7].

1.2 Implantable rotary blood pumps

Cardiovascular diseases including a myocardial infarct and heart failure are the cause of death in 38.9 % of cases in Germany [8]. Heart transplantation to replace the diseased heart muscle is the therapy of choice. However, the number of patients on the waiting list exceeds the number of organs available for transplantation so that this therapy is not available for all patients: The European foundation Eurotransplant reported 1152 patients on the waiting list for a donor heart in 2014, while only 626 heart transplants were performed [9]. The shortage of donor organs promoted the development of mechanical circulatory support systems.

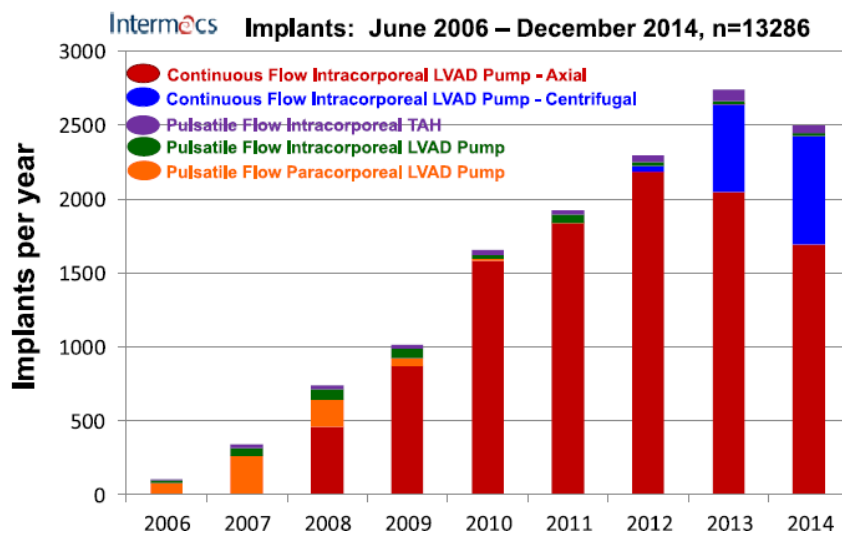


Figure 4: Distribution of left ventricular assist device (LVAD) types by year of implant, from the seventh Intermacs (Interagency Registry for Mechanically Assisted Circulatory Support) report [10]. Today, continuous flow LVADs (rotary blood pumps) are the mainly implanted devices compared to pulsatile positive displacement pumps. A further distinction is made between axial and radial (centrifugal) pumps, intracorporeal (pump implanted inside the body), paracorporeal (pump placed outside the body), and total artificial heart (TAH).

In 2001, the milestone Randomized Evaluation of Mechanical Assistance in the Treatment of Congestive Heart Failure (REMATCH) trial demonstrated that the implantation of a left ventricular assist device (LVAD) as a bridge to transplantation was superior to an optimal medical management (pharmacological) in patients with end-stage heart failure [11]. Now, these systems have become the standard of care for those patients [12]. In most cases, the left ventricle is supported because it is more prone to failure due to the higher pressures in the systemic body circulation.

Current clinically established LVADs are rotary blood pumps which deliver a continuous flow to support the failing ventricle. Rotary blood pumps are smaller, thus better implantable and more durable than their pulsatile predecessors which were positive displacement pumps. This shift has been a development of the last decade which can be observed by the distribution of

used devices by year reported by the InterMACS (Interagency Registry for Mechanically Assisted Circulatory Support) as presented in Figure 4. Although, there is some controversy in the scientific community about the necessity of a pulsatile blood flow and pressure for the human cardiovascular system, e.g. through authors who observed that endothelial function is impaired at absence of pulsatility [13], the advantages of rotary blood pumps still outweigh the risks. Actually, the one-year-survival with rotary blood pumps has reached 85 % as stated in the seventh InterMACS report, see Figure 5.

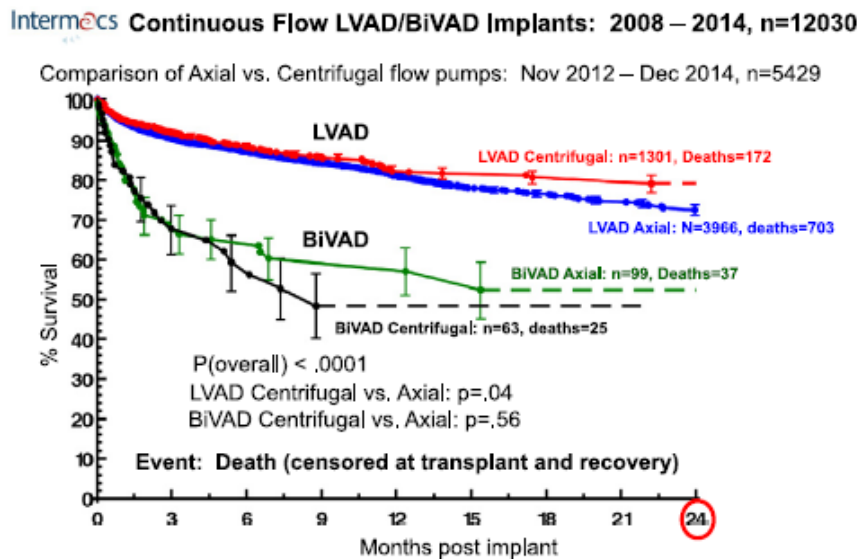


Figure 5: Actuarial Survival of patients with axial or radial (centrifugal) continuous flow LVAD (rotary blood pump) or BiVAD (Bi-Ventricular Assist Device), from the seventh InterMACS report [10]. One-year survival with a rotary blood pump is around 85 % with slightly better values for radial (centrifugal) pumps. The survival rates with BiVADs are worse.

LVADs may be used to bridge the time until a donor heart becomes available, which is called Bridge To Transplant (BTT), or until the heart recovers, which is named Bridge To Recovery (BTR). BTR only applies to 1-2 % of the patients. Since some patients are not eligible for a donor organ and, moreover, the shortage of donor organs does not demonstrate any tendency to regress, LVAD implantation may even be the Destination Therapy (DT). Also Bridge To Candidacy until the patients are put on the waiting list for heart transplantation or Bridge To Decision, where survival of the patient is secured until a decision for a therapy strategy is made, are possible variants of LVAD use [12].

Marseille [14] summarized requirements for rotary blood pumps for left ventricular support. Hydraulically, blood pumps have to work in a physiological range so that a volume flow up to 8 L/min and a pressure head of 150 mmHg are required. High technical reliability and safety are most important for a long-term application. Hence, systems have to be safe from degradation and no additional fluids for instance in the bearing should be used. At the same

time, energy consumption should be low. Furthermore, an adaption to physiological conditions is desirable for optimal support of the cardiac muscle. Finally, such devices have to be biocompatible and sterilisable, minimal traumatic for blood components and anti-thrombogenic.

Especially the last requirements for hemocompatibility are challenging. Thus, LVAD therapy with rotary blood pumps is still limited as patients suffer from serious complications which mainly are infections, bleeding, thrombosis and thromboembolic events, aortic valve pathologies, and right heart failure [15]. The total adverse event rate with rotary blood pumps is 0.3 per patient month during the first year after implantation [10] meaning that at least 3 adverse events occur during 10 months of cumulative support.

A variety of different rotary blood pumps have been developed and introduced into clinic. A comprehensive overview of the history of mechanical circulatory support presenting a range of different devices can be found in [15]. In the following the clinically most frequently used pumps Thoratec HeartMate II and Heartware HVAD which were also investigated during this thesis are presented.

1.2.1 The Thoratec HeartMate II

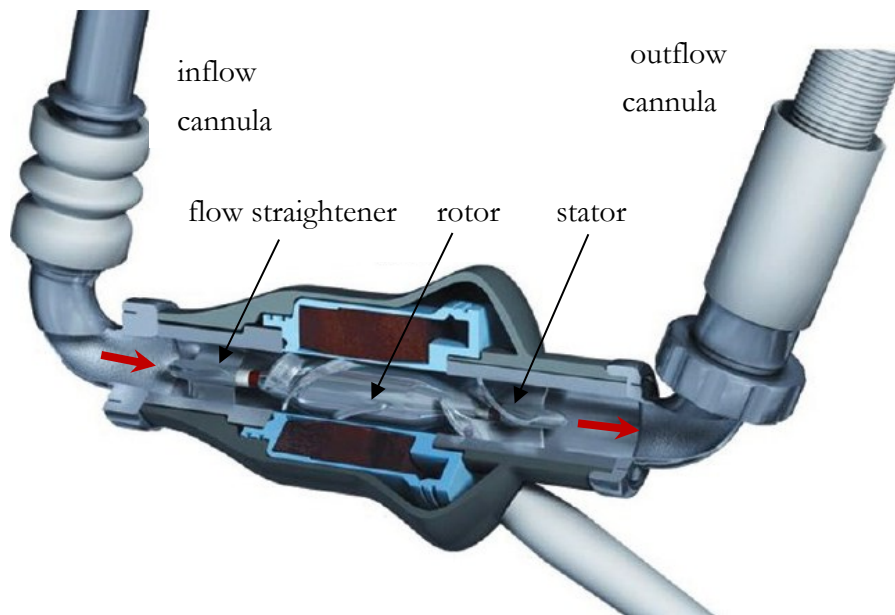


Figure 6: Split view of HeartMate II (HM II) pump along with inflow and outflow cannulae [16]. The HM II is an axial rotary blood pump composed of a flow straightener, an impeller that is mechanically suspended, and a diffuser. Possible operational speeds are between 6,000 and 16,000 rpm [17].

The HeartMate II (HMII; Thoratec Corp, Pleasanton, CA) is an axial rotary blood pump consisting of a housing, inflow and outflow cannulas, a flow straightener, an impeller and a diffuser all made from titanium. The impeller, diffuser, and flow straightener each have three blades.

The blood flow is aligned by the stationary flow straightener, accelerated by the rotating rotor, and again aligned by the stationary diffuser by deflecting the spin of the flow exiting the rotor. The magnetic rotor is driven by a brushless DC motor and supported at its fore and rear ends between the straightener and the diffuser with mechanical pivot bearings comprising of a ruby ball and a ceramic cup. The inner diameter of the housing is 12 mm with a gap of 100 μm to the rotating impeller which were manually measured at an explanted pump. The pump can be operated at rotational speeds between 6,000 and 15,000 rpm with physiological pressures and flows typically achieved at around 9,000 rpm [17]. The weight of the device is 375 g.

The HM II was first introduced into clinic in 2000, and received FDA approval for Bridge To Transplant (BTI) in 2008 [18] and for Destination Therapy in 2010 [19]. Today, more than 20,000 patients worldwide have been implanted with the device [20].

1.2.2 The HeartWare HVAD

The Heartware HVAD (Heartware International Inc., Framingham, MA) is a small radial rotary blood pump (displaced volume: 50 ml; weight: 145 g) with a wide-blade rotor in a volute casing. The casing is composed of a front housing with an integrated inlet cannula and a rear housing with a center-post. Blood contacting surfaces are made from titanium, nitrated titanium and ceramics.



Figure 7: The Heartware HVAD [21]. Left: The assembled pump with the inflow cannula and the radial outlet. Right: The wide-blade radial impeller with front and rear housing. The impeller surface is tapered to create an axial hydrodynamical bearing at rotational speeds higher than 1,800 rpm.

The blood enters the pump through the inlet cannula, is then deflected by the center-post and distributed to the four blade channels which push the blood forward to the volute casing where the blood is collected and led to the outlet. The rotor is suspended by passive magnetic and hydrodynamic forces from an axial thrust bearing between the tapered rotor top surface and the front housing. The rotor outer diameter is 34 mm and the upper and lower gap sum up to a

total of 200 μm movability which was again manually measured at an explanted pump. Each of the housings contains a hermetically sealed motor stator to drive the rotor. The rotational speed can be varied between 1,800 and 4,000 rpm while typical operating points are achieved around 2,500 rpm [22]. CE mark for the HVAD as a BTT device was received 2009 and FDA approval was attained in 2012 [23].

1.2.3 New rotary blood pump technologies

Future trends of VADs are presented by the latest pumps that have been in clinical trial just recently (HeartMate 3) or are intended to be soon (Heartware MVAD), as shown in Figure 8.

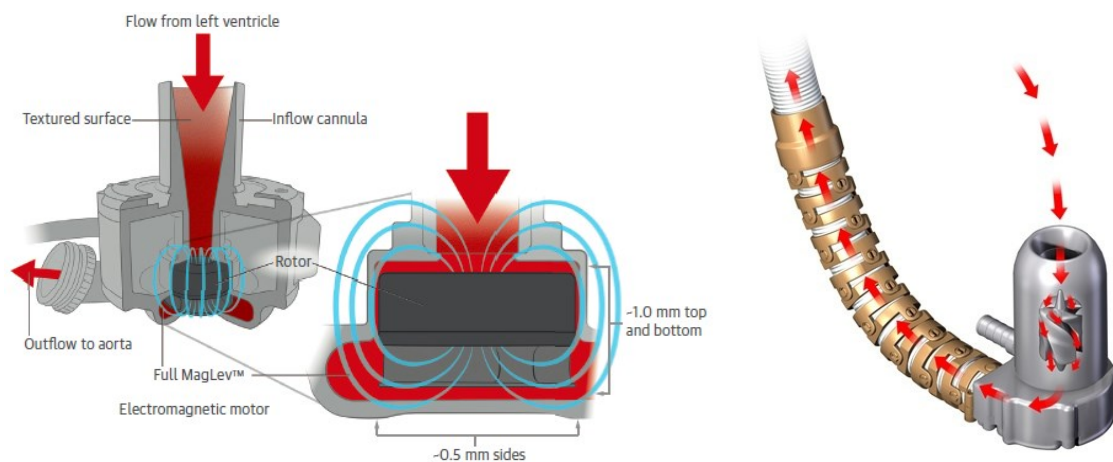


Figure 8: The HeartMate 3 (left) [24] consists of a radial impeller that is active magnetically levitated and features large gaps (0.5-1 mm). The Heartware MVAD (right) [21] has a very small axial impeller that rotates with high speeds (8,000-18,000 rpm) and uses hydrodynamic bearings in combination with passive magnetic bearings to suspend the impeller.

The HeartMate 3 (Thoratec, HM 3) is a radial pump with an active magnetically suspended rotor using large gaps between the moving rotor and stationary housing walls of 500 μm to 1 mm. Furthermore, the blood contacting surfaces of the inner and outer cannula and inner volute casing are sintered titanium to help generate a biological surface [25].

The Heartware MVAD is a miniature axial pump combined with a volute casing. The magnetically and hydrodynamically suspended rotor has a diameter of only about 10 mm. With its small size the pump is less invasive and easier to implant even in smaller patients. Rotational speeds range from 8,000 to 18,000 rpm [26].

Both systems incorporate software algorithms to mimic pulsatility. The HM 3 creates an artificial pulse by altering the rotor speed by 2,000 rpm every 2 seconds. Concerning the MVAD the speed alterations performed by the pump are called qPulse which is a reduction of speed by 5-20 % of the set speed for 5 seconds up to four times a minute [26].

1.3 Blood properties

The biggest challenge of rotary blood pumps lies in the fact that the pumped medium is blood, a body fluid composed of a liquid phase - the plasma - and different cells. The hematocrit which describes the relative amount of blood cells is 40-45 % in healthy humans [27].

Red blood cells or erythrocytes are the most abundant cells and are responsible for the transport of oxygen which is bound by carried hemoglobin. 100 milliliters of normal blood contain approximately 14-15 g of hemoglobin. Erythrocytes are shaped like biconcave discs with a diameter of about 7.8 μm and a thickness of 2.5 μm . However, they are very flexible and their shape changes when they pass through the tiny capillaries [27]. Leukocytes or white blood cells play a major role in the immune system. They are subdivided into different functional cell types which can be slightly larger than erythrocytes and sum up to a total number of about 7000 leukocytes per microliter of blood in contrast to 5 million of erythrocytes [27]. Platelets or thrombocytes are very small discs with a diameter of 1 to 4 μm existing to an amount of 150,000 to 300,000 per microliter blood and taking part in blood coagulation [27]. In case of an injured vessel wall with exposed collagen, platelets become activated. They gain in size, a high number of “arms” protrude from their outer membrane and they adhere more easily. Released adenosine diphosphate (ADP) and other mediators activate other platelets [27]. Then, they bind to collagen with the help of the plasma-protein von Willebrand factor (vWF) and to other activated platelets, subsequently forming a platelet plug which finally converts into a thrombus. Thus, the vWF plays a key role in primary hemostasis where it mediates the binding of platelets to collagen, even at high shear rates. It is a multimeric protein that is stored in and released from endothelial cells. It circulates with the plasma and is also present in platelets [28]. Its size is stated as 10 μm in a globular state while the unfolded vWF molecule can reach lengths of more than 200 μm [29].

Owing to the high number of cells the viscosity of blood is non-Newtonian and higher than the viscosity of water. The dynamic viscosity of pure plasma is approximately 1.25 mPas at 37°C (compared to 0.69 mPas water viscosity at the same temperature). The hematocrit as well as the shear rate in the blood flow have a great impact on blood viscosity, as shown in Figure 9. At low shear rates, erythrocytes form piles where they stick loosely together face-to-face called rouleaux causing a high viscosity [30]. With increasing shear rates, the rouleaux is decomposed by shear forces and viscosity decreases. This phenomenon is called shear-thinning. At shear rates higher than 100 s^{-1} , blood can be considered as a Newtonian fluid with a constant viscosity [31] which is often assumed to be about 3.5 mPas. The shear rate $\dot{\gamma}$ describes the spatial change of the velocity \mathbf{v} over a distance y and is defined as

$$\dot{\gamma} = \frac{dv}{dy} \quad \text{Eq. 2}$$

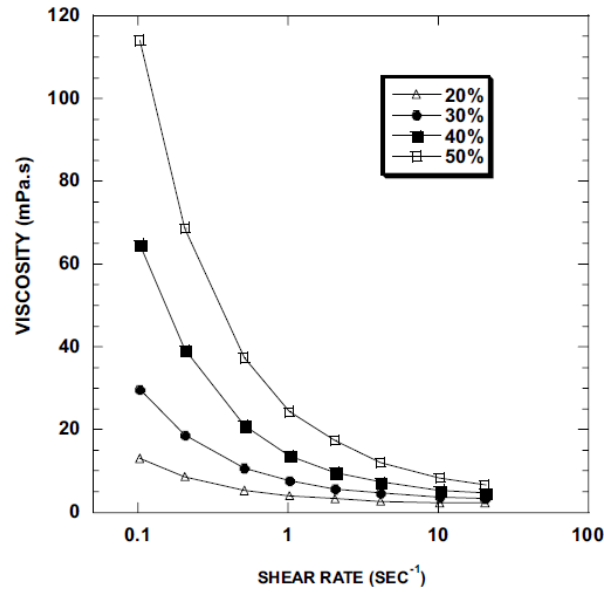


Figure 9: Effect of hematocrit and shear rate on blood viscosity [32]. Blood is non-Newtonian and its viscosity decreases with the hematocrit and with an increasing shear rate.

Another flow effect of blood is the Fåhræus-Lindqvist effect which describes the influence of the capillary diameter on viscosity which is a lower measurable viscosity at lower diameters. This is a result of the segregation of the blood components and a concentration of large cells in the center of the capillary where shear rates are lower [32].

The two-phase composition of blood also affects turbulence. Whether a flow is turbulent can be captured by the Reynolds number Re :

$$Re = \frac{v \cdot d}{\nu} \quad \text{Eq. 3}$$

with the characteristic velocity v , the characteristic length or diameter d , and the kinematic viscosity ν . At a Reynolds number of 2,300 and above flow in a tube is typically turbulent. For blood, Marseille [14] found a shift of the Reynolds number for the laminar-turbulent transition to higher values. Moreover, a decrease of the resistance coefficient and a flatter velocity profile for the turbulent blood flow compared to a flow of a single-phase fluid at the same Reynolds number was found.

1.4 Blood damage in rotary blood pumps

In rotary blood pumps, blood is exposed to many influences that may result in the damage of blood components on one hand and in thrombus formation on the other hand. Both mechanisms are of equal importance in order to prevent serious complications and preserve the function of the cardiovascular system and the device. Artificial blood wetted surfaces inside blood pumps play an important role in blood damage and thrombus formation because they lack the physiological properties of the endothelium. Furthermore, thermal influences might occur which have been found to enhance blood cell damage but are also suspected of triggering thrombus formation [33,34].

The most important influences on blood damage in view of this thesis are the effects of the pump flow, namely non-physiological flow conditions such as elevated shear stress, turbulence, and prolonged contact between blood cells and foreign surfaces. The damage mechanisms are still not well understood although they have been extensively researched in the past. The known damaging effects of the flow conditions are briefly described in the following with respect to different blood components.

1.4.1 Damage of erythrocytes

Damage of red blood cells is called hemolysis. Due to shear forces acting on the cell, the cell membrane is stretched until it becomes porous or even ruptures. The former is more common in rotary blood pumps because for a complete cell rupture extremely high shear rates for longer exposure times are necessary [34,35]. In contrast, in sublethal damage of erythrocytes, hemoglobin leaks out into the plasma and the premature loss of hemoglobin leads to a shortened life span of the cell.

A detailed review of mechanical trauma to erythrocytes is given in [36]. Most importantly, the process of hemolysis has been found to be dependent on shear stress levels as well as on exposure times. Several research groups have investigated this relation in numerous experiments using for instance blood shearing devices based on laminar Couette flow [37,38]. In this special fluid mechanics case, the velocity profile of a Newtonian fluid between a moving (velocity v) and a stationary plate of constant distance Δy is linear, leading to a constant shear stress τ in the entire flow field [39]:

$$\tau = \eta \cdot \frac{v}{\Delta y} = \text{const} \quad \text{Eq. 4}$$

Based on experiments with such flows, e.g. performed by Heuser & Opitz [38], Wurzinger [40], and Paul [41], a power law model for the calculation of hemolysis incorporating the shear stress and the exposure time as well as different empirical constants was derived. Giersiepen [42] translated Wurzinger's data into a formula for the hemolysis index, which is the ratio of the plasma-free hemoglobin ΔHb to the total hemoglobin Hb :

$$\frac{\Delta Hb}{Hb} = HI(\text{in \%}) = A \cdot t^\alpha \cdot \tau^\beta \quad \text{Eq. 5}$$

with the empirical constants $A=3.62 \cdot 10^{-5}$, $\alpha = 0.785$, and $\beta = 2.416$, the time t in seconds and the shear stress τ in Pa, whereby the values without dimensions are to be inserted. Thus, erythrocytes are much more sensitive to shear stress as to exposure time. While it is known today that the Giersiepen-Wurzinger correlation overestimates the actual damage [43], it is still considered valuable since the power constants properly reflect the mechanical characteristics of the erythrocyte membrane [44]. Thus, the correlation is used for engineering purposes. The implementation of the power law into numerical simulations is described in section 1.7.4.

Although hemolysis is not as commonly observed with modern continuous flow devices as it was with the earlier pulsatile ones [45], it is still frequently seen in VAD patients [46]. Furthermore, hemolysis is commonly used for pre-clinical testing of blood pumps. It is measured for instance based on plasma-free hemoglobin or based on the level of lactate dehydrogenase (LDH) in blood, which is a marker for cell death.

1.4.2 Effects on platelets

Other effects in the flow of a rotary blood pump are the activation or the damage of platelets. Again, platelets, together with the vWF, are essential for hemostasis. Hemostasis is influenced by three aspects, which together are known as Virchow's triad: the characteristics of the surface, the state of the blood, and the local flow environment. The natural balance in Virchow's triad between coagulation and lysis is disturbed by rotary blood pumps such that anticoagulation is required in all LVADs patients in order to prevent a thrombus inside the pump. A thrombus may either disturb the function of the device until it is interrupted or may be washed off and transported through the circulation system causing a thromboembolic event such as a stroke. Still, high stroke rates of 28.7 % and 12.1 % of patients with an HVAD and a HM II respectively within two years were reported in the Endurance trial [47].

Besides chemical agonists, elevated shear stress in the blood flow can lead to platelet activation [48]. Hellums summarized data of different authors and presented a relation between platelet activation and shear stress as well as exposure time [49].

Activated platelets have increased propensity to adhere which in turn may lead to thrombus formation when other flow conditions are present as well: stagnant, slow or recirculating flows and low shear stresses [50]. Furthermore, regions of disturbed flow are associated with platelet adhesion because a transport of platelets from the main flow to the surface is required [51].

Thus, as Bluestein summarized, "hemodynamic optimization is aimed at avoiding the formation of stagnant zones and regions of elevated stresses, while achieving good washout characteristics" [52]. Thrombus formations in the HeartMate II pump have been seen in the impeller inlet

region or around the front bearing and in the blade channels as well as in the diffuser gap region, as shown in Figure 10.

In contrast to this type of thrombus, which is a soft, red thrombus that forms quickly and in areas of low flow, the white thrombus is rather hard and takes more time to form in areas of high shear rates with the help of vWF nets that capture even not yet activated platelets [53]. Thus, high shear rates should be avoided as well.

A comprehensive overview of pump thrombosis and influencing factors is given by Blitz [54].

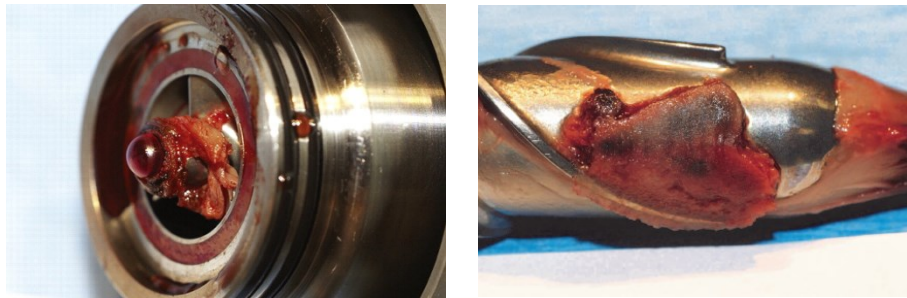


Figure 10: Thrombus formations in a HeartMate II pump. Left: A thrombus around the front bearing at the impeller inlet region [55]. Right: Attached thrombus formations in the second half of the blade channels and in the diffuser gap region [56].

1.4.3 Degradation of von Willebrand factor

Another blood component that is subject to trauma in rotary blood pumps is the von Willebrand factor (vWF). Large multimers of the vWF are necessary for proper platelet adhesion and aggregation. As vWF is subjected to elevated shear stress, the large multimers are unfolded, so that cleavage sites are exposed and in the following, proteolysis is enhanced leading to a loss of the large vWF multimers. This happens in patients with aortic stenosis [57] as well as in patients with an implanted rotary blood pump [58–60] who have a reduced concentration of large vWF multimers which is called the acquired von Willebrand's disease. In this, platelet function is decreased and the patient's susceptibility to bleed is increased.

The degradation of vWF multimers and its relation to shear stress has been studied in vitro. Siedlecki et al. [61] used a rotating disk system and found that vWF molecules are unfolding at a shear stress above around 3.5 Pa. Tsai et al. [62] showed a decrease of large vWF multimers at approximately 5 and 7 Pa in plasma flowing through capillary tubes. Di Stasio et al. [63] calculated a shear stress threshold of more than 10 Pa necessary to unfold the vWF so that the cleavage sites are exposed.

1.5 The fluid mechanics principles of rotary blood pumps

The development of rotary blood pumps relies on the theory and methods of the classic fluid-flow machine theory for centrifugal pumps as described by Gülich [64] or Pfleiderer & Petermann [65]. While the same principles apply, the terminology differs slightly between the clinical and the technical language. For instance, a clinician refers to a radial pump by the term centrifugal. However, in this thesis the technical convention is adapted and the term centrifugal pumps covers all types of pumps for which the following theory is valid.

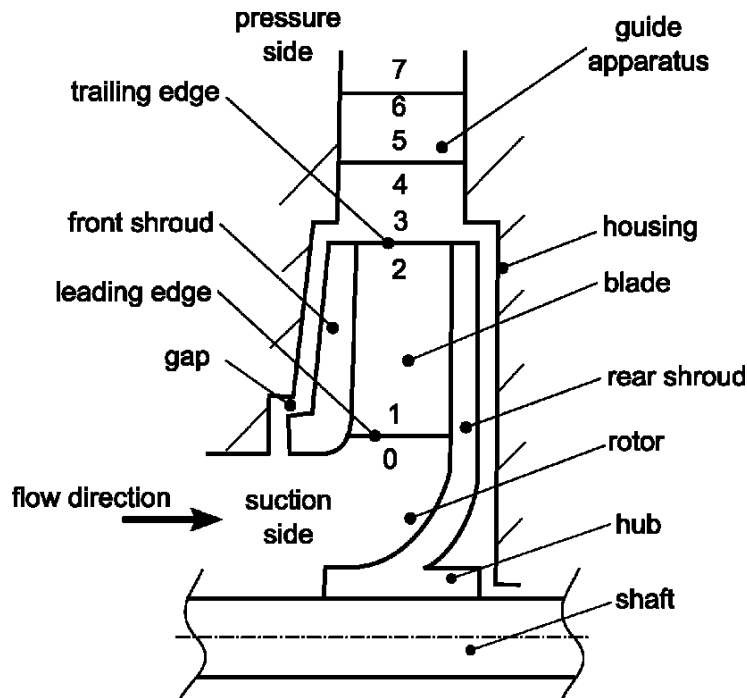


Figure 11: Basic construction of a centrifugal pump with a radial impeller. The main part is the rotor or impeller, which is composed of a front and rear shroud and the blades. The impeller rotates inside of the housing and is completed by a guide apparatus (here a diffuser with guide vanes). Furthermore, the common indexing of pumps according to the energy status of the fluid is depicted.

Centrifugal pumps are used for the transport of fluids, providing a certain volume flow at a certain pressure level. Main part of a centrifugal pump is the impeller which is revolving and has blades. The impeller transfers energy to the fluid which consequently undergoes acceleration, deceleration, and deflection. Accordingly, mechanical energy from the electric motor is transformed into kinetic and potential energy of the fluid, resulting in an increase of velocity and static pressure. Moreover, centrifugal pumps generally incorporate a stationary guide apparatus or collector, which converts the kinetic energy downstream of the rotor into additional static pressure. Thus, at the outlet of the pump, which is the pressure side, the fluid has a higher

energy level than at the inlet of the rotor, which represents the suction side. A schematic overview of a centrifugal pump is given in Figure 11. It is common to denote flow parameters inside of a centrifugal pump according to the increase of energy.

The most important parameter to describe a centrifugal pump is the specific work Y , the total useful energy transmitted to the fluid by the pump per unit of mass. It is calculated by the sum of energy differences due to a change of static pressure p , velocity v , and geodetic height z between suction side (p_s, v_s, z_s) and pressure side (p_p, v_p, z_p) [66]:

$$Y = \frac{p_p - p_s}{\rho} + \frac{v_p^2 - v_s^2}{2} + (z_p - z_s) \cdot g \quad \text{Eq. 6}$$

The specific work is independent from type and density of the medium, but generated pressure heads vary with different fluids. In blood pumps, the height differences are usually negligible. Negligible is also the velocity term when inlet and outlet nozzle diameters are equal. Therefore, mainly pressure differences are to be considered when calculating the specific work. Of similar importance are the useful power P_u , which is calculated from the specific work and the mass flow by multiplication, and the efficiency of the pump, which is the relation of pump power and motor power [66]:

$$P_u = Y \cdot \dot{m} \quad \text{Eq. 7}$$

$$\eta = \frac{P_u}{P_{el}} \quad \text{Eq. 8}$$

The calculation and design of centrifugal pumps relies on the assumption, that the flow is tangential to the blade shape. Theoretically, this would only be the case for an infinite number of infinitely thin blades, thus an approximate solution of the flow is considered.

The velocity conditions inside of the pump are captured by three types of velocity vectors: the circumferential velocity \vec{u} is derived from the rotational speed and the radius, the relative velocity \vec{w} can be observed in a moving relative reference frame; and the absolute velocity \vec{v} is the vector sum of the two [67]:

$$\vec{v} = \vec{u} + \vec{w} \quad \text{Eq. 9}$$

The relation is presented in the form of velocity triangles, as shown in Figure 12 for the in- and outlet of a blade. At the inlet, commonly a uniform, non-spinning flow is assumed so that the absolute velocity is in axial direction.

The total specific work transmitted to the fluid by the blades Y_{bl} captures the specific work Y as well as hydraulic losses Z_h [67]:

$$Y_{bl} = Y + g \cdot Z_h \quad \text{Eq. 10}$$

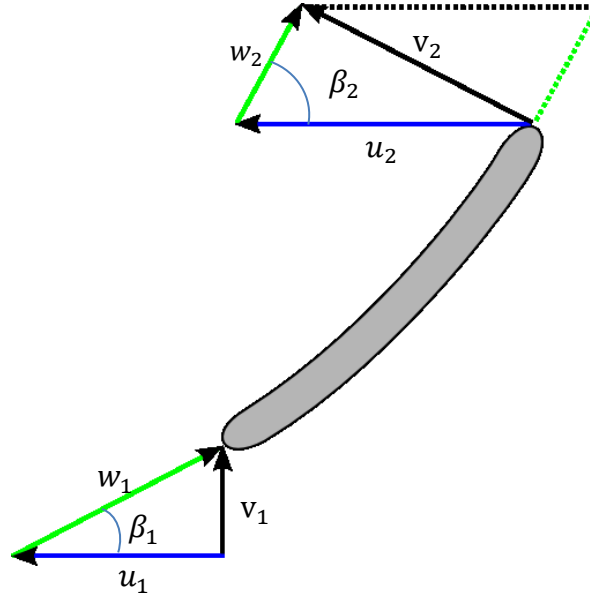


Figure 12: Velocity triangles for the inlet and outlet of a blade. The absolute velocity v is the vectorial sum of the circumferential velocity u and the relative velocity w . The relative velocity is tangential to the blade shape with the blade angle β to the circumferential direction. At the inlet, a non-spinning flow is commonly assumed and the index 1 is used, while the outlet is denoted with the index 2.

The specific blade work is calculated by the “Euler’s turbine equation” which is deduced from the conservation of angular momentum [67]. According to this, the difference of angular momentum at the inlet and outlet of the impeller equals the torque. It reveals as:

$$Y_{bl} = u_2 v_{3u} - u_1 v_{0u} \quad \text{Eq. 11}$$

where v_{0u} is usually set to zero for non-spinning inlet flow. Using the three velocities, the equation can be transformed into:

$$Y_{bl} = \frac{1}{2} (v_3^2 - v_0^2 + u_2^2 - u_1^2 + w_0^2 - w_3^2) \quad \text{Eq. 12}$$

Thereby, $(v_3^2 - v_0^2)$ corresponds to the difference of the fluid velocity in the absolute reference frame between inlet and outlet. $(u_2^2 - u_1^2)$ comprises the change of circumferential velocity, which is zero for an axial-flow pump. $(w_0^2 - w_3^2)$ includes the difference of the relative velocity in the reference frame that is moving with the impeller. Thus, the pressure build-up in the impeller is higher, the greater the increase of absolute and circumferential velocity and the greater the simultaneous decrease of the relative velocity from inlet to outlet.

Plotting the pressure head over the volume flow results in the characteristic curve, which describes the hydraulic performance of a pump. The characteristic curve can be deduced theoretically. In accordance to Eq. 11, Y_{bl} is a line with a constantly descending slope. From this, losses resulting from friction, which increase with volume flow, and shock losses caused by the imperfect flow impinging on the blades at off-design conditions must be subtracted [65] as shown in

Figure 13. The characteristic curve is very important as it indicates the behavior of a pump under changing operating conditions.

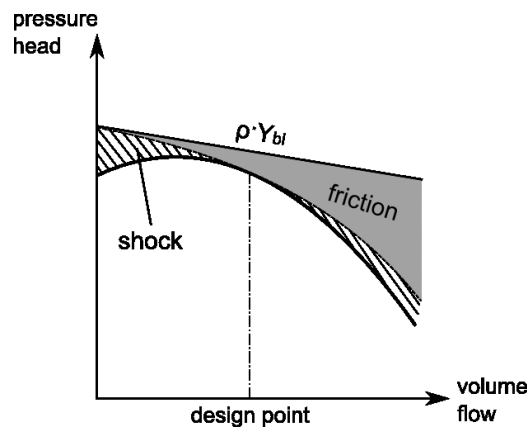


Figure 13: Composition of the characteristic curve. The ideal pressure-flow relation is linear but losses resulting from shock in off-design points and friction have to be subtracted so that a curve emerges [65].

Corresponding to numerous different fields of application, there are a number of different designs of centrifugal pumps and belonging components, as shown in Table 1.

One way of classification is by the flow direction through the impeller: axial, which is parallel to the main axis, radial, which is perpendicular to that axis, and diagonal or semi-axial.

Axial-flow pumps are generally applicable for higher volume flows, while radial pumps allow for higher and more stable pressure heads. Furthermore, an open or closed (shrouded) impeller is possible. The guide apparatus can either be designed as a diffuser, which incorporates guide vanes in axial, diagonal, or radial design, or as a volute casing, or simply as a concentric annulus. The hydrodynamic performances of axial and radial pumps are different. This can be seen in the typical characteristic curves for the different pump types. While radial pumps present a so-called flat curve where the pressure head changes only slightly over a large range of flow rates, axial pumps have a steeper curve, as illustrated in Figure 14.

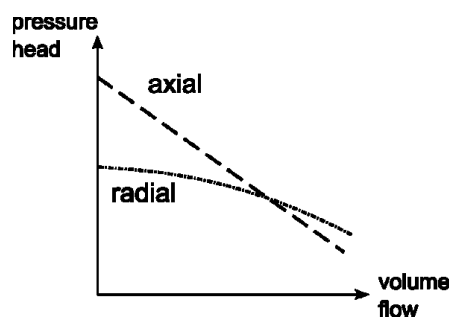
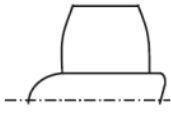
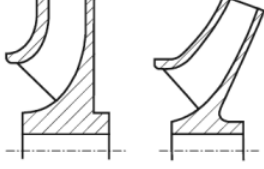
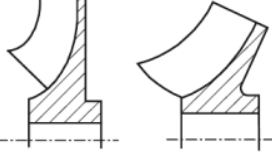
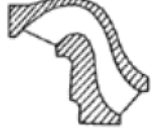
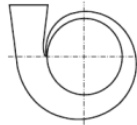
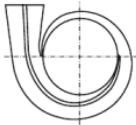
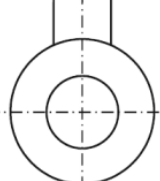
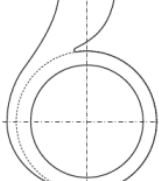


Figure 14: Typical characteristic curves for radial and axial pumps. Radial pumps have a flat curve while axial pumps have a steeper, almost linear curve.

Table 1: Pump components and designs [66]

Component or feature	Radial	Diagonal	Axial
Impeller form: Flow direction			
Impeller type	Closed (shrouded) 	Semi-open 	Open 
Diffuser: Flow direction	Radial 	Diagonal 	
Outlet casing	Single-volute  Double-volute 	Concentric annulus 	Concentric annulus plus volute 

Centrifugal pumps are optimally designed for a specific operating point defined by the customer. The specific speed builds a link between the most important parameters the volume flow \dot{V} , the pressure head Δp and the rotational speed n [65]:

$$n_q = 333 \cdot n \cdot \frac{\sqrt{\dot{V}}}{\left(\frac{\Delta p}{\rho}\right)^{3/4}} \quad \text{Eq. 13}$$

This dimensionless index characterizes the impeller shape. Thus, general practice in the development of centrifugal pumps is the selection of an impeller shape depending on a required operating point and rotational speed based on the resulting specific speed. For lowest specific speeds, radial pumps are chosen, and high specific speeds lead to axial pumps with diagonal pumps in between [64]. Usually, this approach also targets at pumps with best efficiencies. However, efficiencies of very small pumps are generally lower and fluid dynamics are influenced by wall-bounded flows to a greater extent. Furthermore, rotary blood pump designs are also subject to anatomical restrictions, usability issues and the like [14].

1.6 Experimental methods to investigate rotary blood pumps

In the following sections, the experimental methods that were used to investigate established rotary blood pumps as well as a newly developed pump are presented. First, the similarity laws essential for the development of experimental models are elucidated. Next, two experimental methods used in this thesis are introduced: Since the flow close to the surface is of great importance for blood trauma as explained earlier, the Wall PIV method and the paint erosion method were chosen to give deeper insight into flow characteristics close to the surface. These methods were also used to validate the computational fluid dynamics results which are explained later on. In addition, a technique for the acquisition of characteristic pump curves is described.

1.6.1 Similarity laws

When performing experimental flow investigations, the first step is to translate the real problem into a representative experimental model. For the investigation of rotary blood pumps it is helpful to upscale the otherwise very small pumps for better experimental accessibility. Thereby, the similarity laws have to be considered. Generally, geometric and dynamic similarity must be observed. Geometric similarity is fulfilled when all parts that are involved in conducting the flow are scaled with the same ratio from the prototype's original scale to the model. Dynamic similarity is captured by dimensionless numbers. A range of dimensionless numbers exist and a selection as well as their derivation can be found in [68]. For this thesis, mainly the Reynolds number Re , which has been introduced in section 1.3, Eq. 3, is important. For centrifugal pumps, it can be calculated based on the impeller diameter as characteristic length and the circumferential velocity as characteristic velocity [65]. The Reynolds number must then be equal for the original device and the experimental model. The Euler number Eu , which expresses the relationship between a pressure drop Δp and the kinetic energy per volume of the flow (ρv^2), enables a conversion of the pressure head from the experiment to the original scale:

$$Eu = \frac{\Delta p}{\rho v^2} \quad \text{Eq. 14}$$

The Reynolds number and the Euler number together represent the criteria of dynamic similarity for flows which are affected only by viscous, pressure and inertia forces. For pumps, the previously introduced specific speed can be considered a similarity coefficient as well. However, the specific speed is equal by default when Reynolds and Euler similarity are observed.

1.6.2 The wall-PIV measurement technique

The wall Particle Image Velocimetry (wall-PIV) technique can be used to detect velocity fields close to vaulted walls, for instance the housing of a blood pump. The idea of the wall-PIV method is described in [69], while a detailed report on the development and validation of the

technique is given by Berthe in [70]. Briefly, particles in the flow field inside of a transparent model are observed up to a predefined distance from the wall. This is accomplished by illuminating the field of interest with a diffuse, monochromatic light and adding a molecular dye to the fluid that absorbs the emitted wavelength of the light source. Thereby, the visible depth is limited to approximately 300 μm from the wall. The distribution and brightness of the light reflecting particles is then captured by a camera over a certain time period.

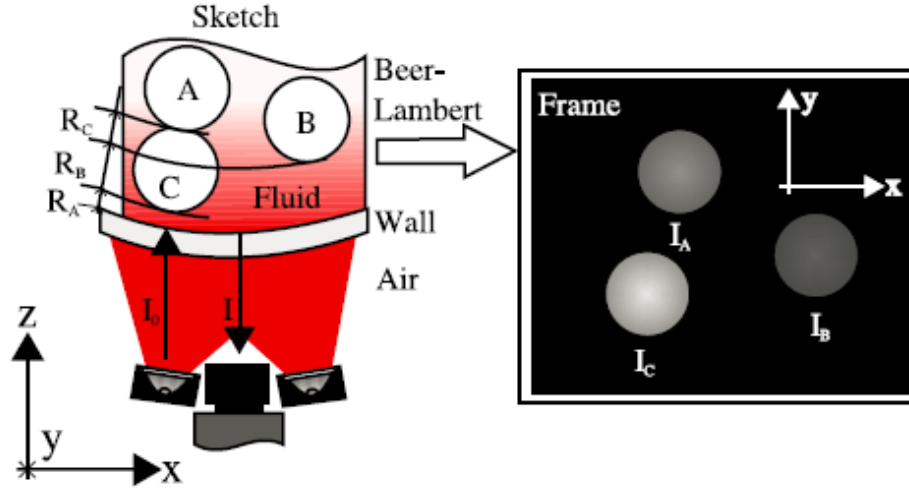


Figure 15: Principle of the wall-PIV method [71]: On the left hand side, the illuminated region of the fluid and three tracer particles A, B and C with the corresponding distances R are shown. On the right hand side, a representative image recorded by the camera with the corresponding particle intensities is displayed.

The displacement of the particles between the images can be translated into a velocity field via cross-correlation, optical flow [71] or particle tracking similar to standard PIV. In the frame of this thesis, particle tracking was used. The gray scale of the particles is used as depth information. This is accomplished by using the Beer-Lambert's law which describes the intensity I based on the distance of the particle to the surface R , the molar absorption coefficient of the dyed fluid ϵ and the concentration of the dye c :

$$I = I_p e^{-\epsilon c R} \quad \text{Eq. 15}$$

Thus, theoretically three dimensional velocity fields can be derived. On this basis, wall shear stresses can be deduced:

$$\tau_w = \eta \frac{\partial v}{\partial r} \quad \text{Eq. 16}$$

In this equation, wall shear stress τ_w is calculated based on the dynamic viscosity η multiplied with the normal gradient of the velocity v at the distance to the wall r .

Wall shear stresses are of great importance for the interaction of blood with the surface and the evaluation of blood damage.

Berthe [70] also showed how the wall-PIV method was used for investigating a pulsatile blood pump. However, in this thesis the technique has been adapted for a rotary blood pump to investigate the flow close to the housing wall in the critical gap region.

1.6.3 The paint erosion method

The paint erosion method is a technique for the visualization of flow patterns close to the surface. Also known as the oil film technique, this method has been a standard practice in wind tunnel experimenting for many years [72]. The surface is coated with a special paint consisting of oil and a color pigment. Then, frictional forces lead to streaky deposits on the surface, after the air flow was applied to the oil layer for a short time interval. The method is used to analyze the direction of the flow, the point of transition from laminar to turbulent flow, as well as the positions of flow separation and reattachment. The streaks made visible correspond to the direction of the wall shear stress, but only if pressure gradients are small which could otherwise also influence the direction in which the oil is carried. Thus, results of the paint erosion method have to be interpreted with caution. Moreover, there is no generally applicable technique and the ideal paint mixture for a specific flow problem must be developed and adjusted to the given conditions.

The method has been applied for a rotary blood pump by Sieß [73], see Figure 16. Sieß used a water-insoluble, highly viscous mixture of linseed oil, Oxide Black, Zink white pigment, and turpentine.



Figure 16: *Paint patterns on the surface of the impeller of a micro-axial blood pump [73]. The flow is entering the pump from the left side. One blade, the rear end of a second blade and a part of the hub are displayed. Except for the area on the hub close to the inlet and the blade, a uniform washout can be seen which is likely to correspond to a uniform wall shear stress.*

He stated that the remaining surface coverage gives qualitative information on the wall shear stress distribution, and areas of flow separation can be visualized as well - both aspects are important to evaluate the risk of thrombus formation in a blood pump.

1.6.4 Measurement of characteristic curves

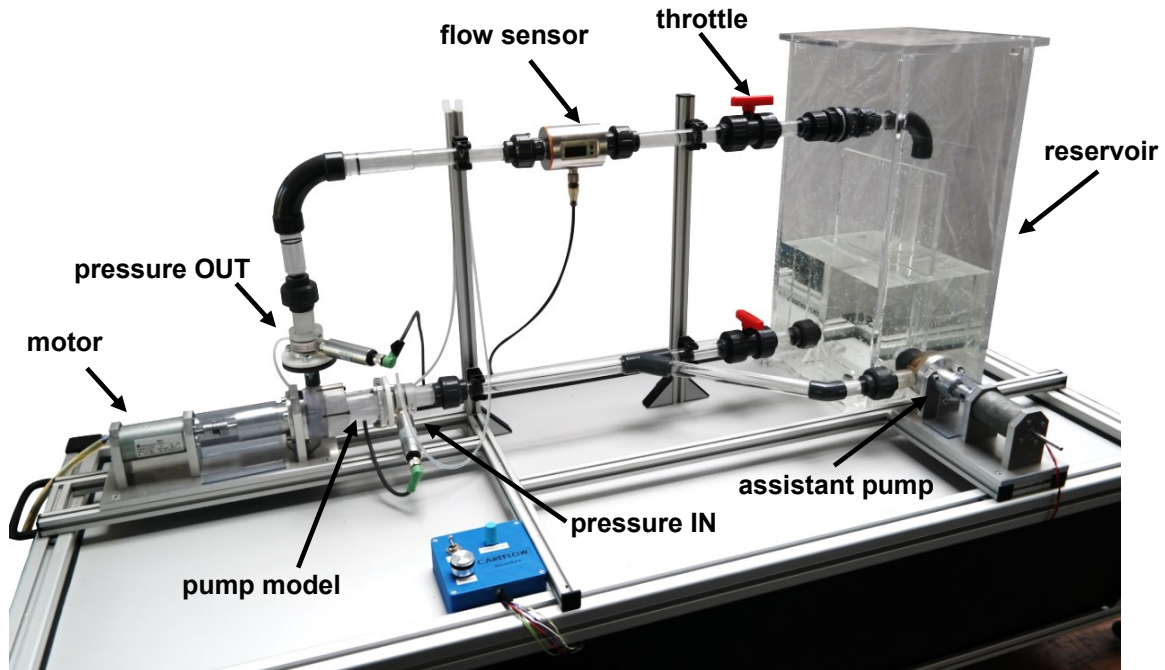


Figure 17: Test setup for the measurement of characteristic curves. The flow loop includes a long inlet tube to ensure fully developed inlet flow to the pump model. Pressures are measured via pressure transducers close to the in- and outlet, and flow is regulated with the help of a throttle and measured via a magnetic inductive flow sensor. An assistant pump overcomes the resistance of the flow loop at higher flow rates so that a wider range of flow rates is possible.

An accurate and reproducible measurement of characteristic curves is of great importance to capture the operational behavior of pumps and thus, during the development process of rotary blood pumps. Hence, a test setup has been established to acquire the pressure head over a large range of volume flows for pump prototypes. The setup is shown in Figure 17 and shall be briefly described here.

The test stand features a big reservoir for the test fluid which incorporates a vertical plate to prevent air bubbles from entering the flow loop. The connection between the reservoir and the pump inlet is a long and straight inlet tube (inner diameter: 16 mm, length: 250 mm from the T-connector to the inlet pressure sensor) to ensure uniform flow entering the pump.

The pressure head is measured via two pressure transducers at small distances to the inlet and outlet of the pump. The sensors are connected to a ring channel that is surrounding the flow tube and is flooded through four drilled holes in the wall of the flow tube. In this way the static

pressure is automatically averaged over the flow cross-section.

Flow is measured further downstream of the outlet with a magnetic-inductive flow sensor. The operating point is regulated by a throttle.

A self-constructed assistant pump is used to overcome pressure losses in the flow loop in order to increase the achievable flow range. It is connected to the reservoir and inlet tube and pumps in series with the pump model.

The model fluid was a mixture of osmotic water and glycerol, e.g. with a volumetric proportion of 37.5 % glycerol (99.5 % pure) at 24°C temperature resulting in a dynamic viscosity of 3.5 mPas. The viscosity was measured with a capillary viscosimeter (Ubbelohde, type 501-01). The mixture ratio had to be adjusted depending on the temperature to achieve the desired dynamic viscosity.

1.7 Computational fluid dynamics in rotary blood pumps

Computational fluid dynamics (CFD) is a helpful tool to support the development process of rotary blood pumps. It can already be applied in an early phase of the process and is less time and money consuming than prototyping and experiments. Moreover, commercial software gets further refined and usability as well as computer power have increased in recent years. Thus, CFD has been widely used in the field of rotary blood pumps to describe hydrodynamic performance of rotary blood pumps, to optimize pump design as well as to assess potential blood trauma [74,75]. In the following sections, a description of the principles and general procedure of numerical investigations of rotary blood pumps is given. In contrast to other numerical approaches, the complex geometries of centrifugal pumps as well as the rotation of the impeller represent challenges.

The CFD process is divided into three steps: In a first step, the pre-processing, the physical domain is discretized, which means subdivided into a finite number of nodes and cells. For the resulting mesh, the conservation equations of mass, momentum and energy, in the case of pumps the Navier-Stokes equations and the continuity equations, are to be solved. Therefore, these partial differential equations have been approximated by representative algebraic equations. Still during pre-processing, the simulation settings are defined, for instance the material properties and the boundary conditions are set on the borders of the computational mesh. This first step results into a linear system of equations for the unknown flow parameters, such as velocity and pressure, in each cell. In a second step, values for these parameters are calculated iteratively for each cell and ends up with a solution of the entire flow field. Finally, the post-processing as the last step is concerned with the critical analysis of the results.

In this thesis, two types of commercial software were used. These were Ansys CFX (ANSYS, Inc., Canonsburg, USA) and STAR CCM+ (Cd Adapco, Nuremberg, Germany). In both, the Finite Volume Method is utilized which is common in Fluid Dynamics. This approach starts with the integral form of the conservation equation that is applied to control volumes which are the finite representatives of the solution domain. In the process, volume integrals are converted into surface integrals which are then approximated by quadratic terms. The surface values are used to interpolate the centroid values of the control volumes so that an algebraic equation for each node containing the neighbor node values results. The Finite Volume Method is conservative by definition and applicable for complex geometries and any type of mesh. A detailed description can be found in [76].

1.7.1 Mesh generation

The mesh is of major importance for a CFD simulation as it influences the validity, accuracy, and stability of the solution. The quality of the mesh depends on the distribution of cells, the smoothness of the mesh, and the shape of the cells. A higher cell density is required in areas

where high gradients are present whereas in areas of even flow the number of cells can be lower to save computational cost. Transitions between cell sizes must be smooth to avoid increasing the discretization errors. Additionally, the shape of the cell may not be extremely deformed. For different types of cells, hexahedral, tetrahedral, or polyhedral, the cell deformation is described by different indicators. Different quality criteria exist also depending on the solver which is why reference is made to the user manuals of the specific software at this point.

Meshes can be structured, regularly constructed and composed of hexahedral cells only, completely unstructured and built up by tetrahedral and polyhedral cells only, or hybrid with structured layers in areas where it is advantageous. In one case of a radial type rotary blood pump Fraser et al [75] reported that specific flow phenomena could not be captured with tetrahedral cells. A hybrid mesh was necessary and is therefore in favor. Generally, a mesh independence study has to be conducted for each CFD problem. Thereby, the cell number and density is gradually refined until the solution stabilizes.

1.7.2 Numerical simulation of flow in rotating regions

There are two possibilities to simulate the flow in a rotating region like the impeller region in a centrifugal pump. In the Multiple Reference Frame (MRF) or Frozen Rotor method, different zones are defined and the velocity vectors are transformed to include the rotating effect on the rotating zone. This model is a stationary approximation of the flow field because rotating and stationary parts are in a fixed relative position. Transient effects cannot be simulated. Thus, MRF simulations are mainly performed to obtain a good starting solution for a Sliding Mesh simulation. The Sliding Mesh method, on the contrary, includes the rotation of the rotor by updating the mesh after each time step.

Sliding Mesh simulations are more accurate but also more time-consuming and require more computer storage. For a special case, Taskin et al. found a deviation of the pressure head of a radial pump of 6 % when comparing both methods [77]. Nevertheless, the quality of MRF simulations strongly depends on the degree of interaction between rotor and stator and is not in favor when transient effects are to be considered as well.

1.7.3 Modeling turbulence

The Navier-Stokes equation is a partial differential equation of second order and can be written as follows:

$$\frac{\partial v_i}{\partial t} + v_j \frac{\partial v_i}{\partial x_j} = -\frac{1}{\rho} \frac{\partial p}{\partial x_i} + \nu \frac{\partial^2 v_i}{\partial x_j^2} \quad \text{Eq. 17}$$

Turbulence is a flow phenomenon that typically develops at a critical Reynolds number (2300 for a pipe flow) and involves a cascade of eddies that take energy from the mean flow and brake

down to progressively smaller scales until they are dissipated as heat. It can be described as a mean flow field which is superimposed by stochastic fluctuations of the flow variables. When the fluctuations are taken into account in the Navier Stokes equation so that the variables are introduced as a superposition of a mean and a fluctuating term $v_i = \overline{v}_i + v'_i$, the Reynolds-Averaged Navier-Stokes (RANS) equation results in [78]:

$$\frac{\partial \overline{v}_i}{\partial t} + \overline{v}_j \frac{\partial \overline{v}_i}{\partial x_j} = -\frac{1}{\rho} \frac{\partial \overline{p}}{\partial x_i} + \nu \frac{\partial^2 \overline{v}_i}{\partial x_j^2} - \nu \frac{\partial}{\partial x_j} (\overline{v'_i v'_j}) \quad \text{Eq. 18}$$

In contrast to its origin, this equation contains additional terms which comprise the velocity fluctuations and are known as Reynolds stresses. These are additional unknowns in the equation system – the so called closure problem – so that additional equations are necessary for their solution. On this ground, turbulence models were developed. In a first attempt, Boussinesq proposed that the Reynolds stresses can be described analogous to the viscous stresses by means of a turbulent or eddy viscosity μ_t :

$$\tau_{ij} = -\rho \overline{v'_i v'_j} = \mu_t \left(\frac{\partial \overline{v}_i}{\partial x_j} + \frac{\partial \overline{v}_j}{\partial x_i} \right) - \frac{2}{3} \rho k \delta_{ij} \quad \text{Eq. 19}$$

where δ_{ij} is the Kronecker delta, which equals 1 for $i=j$ and 0 for $i \neq j$, and $k = 1/2 \cdot (\overline{v_1'^2} + \overline{v_2'^2} + \overline{v_3'^2})$ is the turbulent kinetic energy. Simple models using this approach are known as Mixing Length models. A more complex approach is made by the $k-\varepsilon$ model which incorporates transport equations for the turbulent kinetic energy k and the turbulent dissipation ε and thereby includes not only convection and diffusion but also production and dissipation of turbulence. An underlying assumption of both, the mixing length model and the $k-\varepsilon$ model is the isotropy of the eddy viscosity. The $k-\varepsilon$ model is very robust and accurate but requires high Reynolds numbers and fully developed turbulence. The $k-\omega$ model, in the contrary, contains a transport equation for the specific dissipation rate ω rather than for the dissipation, and gives good results also for lower Reynolds numbers and wall bounded flows. Based on the mean velocity calculated from the inlet diameter and a typical volume flow of 5 L/min for a blood pump, the Reynolds numbers for the HM II and the HVAD are 2650 and 2490 ($d = 12.00$ mm; $d = 12.75$ mm), respectively, which points to a flow in the low Reynolds turbulent range.

Thus, in rotary blood pumps, most often the Shear-Stress-Transport $k-\omega$ (SST $k-\omega$) model by Menter is used [75,77,79,80]. This model combines the advantages of the $k-\varepsilon$ model in the free-stream with the advantages of the $k-\omega$ model in the near wall regions for low Reynolds numbers. There are two options to calculate the flow in the boundary layer depending on the resolution of the mesh at the wall. Briefly, the y^+ value is used to describe the non-dimensional distance from the first node of the mesh to the wall based on the friction velocity v^* , the distance to the nearest wall y , and the kinematic viscosity ν :

$$y^+ = \frac{v^* \cdot y}{\nu} \quad \text{Eq. 20}$$

On one hand, the turbulent boundary layer can be directly resolved, if y^+ is around 1. On the other hand, if y^+ is above 15, wall functions are used to capture boundary layer flows. In general, it is essential to place at least ten nodes in the boundary layer.

It should be noted that RANS models, although the most widespread method amongst CFD investigations of rotary blood pumps, are not the only way to account for turbulence. Large Eddy Simulation (LES), where only small length scales are modeled and larger scales are resolved, and Direct Numerical Simulation (DNS), where the flow field including turbulent features is completely resolved, are other possibilities. However, these methods require very high mesh resolution and intense computer power which makes them prohibitive except for very simple flows. Further details on turbulence modeling can be found in [78].

1.7.4 Modeling blood trauma

As described in section 1.4, there are several processes leading to alteration of normal blood function in rotary blood pumps, such as hemolysis, platelet activation, and vWF degradation. Among them, hemolysis is the best studied. The most common practice is to calculate a hemolysis index based on the power law assumption as proposed by Giersiepen [42] or others. In a Lagrangian manner the damage index can be derived based on pathlines through the pump by simply integrating the power law using shear stress and residence time along the pathlines. This has been done by several groups and in different ways, for instance to account for the damage history of the cells as in suggestions by Goubergrits and Affeld or Grigioni et al. [44,81]. However, using computationally derived pathlines introduces problems because they are difficult to set up in areas with zero velocity as in flow separation zones and therefore do not represent the entire flow field. Thus, a Eulerian approach is advantageous as it takes the entire flow region into account. Garon and Farinas proposed a simple approach where a volumetric integration of a linearized time derivative of the power law over all cells is done [82]. This global approach is easy to implement but fails to account for altering residence times in the flow field. In contrast, a transport approach where the damage as a scalar is transported via convection and diffusion as well as produced within the flow field equally considers all flow regions, allows for the inclusion of the damage history in the production term, and even gives the opportunity to visualize the distribution of damaged blood in the field [83]. Taskin et al. compared different Lagrangian methods with a Eulerian transport approach and found the scalar transport method to be more reliable when relatively comparing different pumps [84]. In this thesis, a revised transport approach for calculating hemolysis based on the power law assumption is presented. It has to be mentioned that the power law is only strictly valid for a constant shear field as it was derived from Couette flow experiments. Though it has been extrapolated and used for

complex and altering flows as in rotary blood pumps with partially good agreement with in-vitro results, this may not reflect the real process of blood damage in such flow conditions. Furthermore, turbulent effects cannot be correctly considered so far since there is no data on how exactly turbulence leads to blood damage. Nevertheless, it is known that a turbulent flow causes additional blood damage compared to an according laminar flow which has been shown by Kameneva et al. [85]. Moreover, using Reynolds stresses results in overestimation of blood damage since Reynolds stresses do not represent a physical force acting on the cells [86,87].

The evaluation of the other types of blood damage which have not been studied as thoroughly as hemolysis, can be accomplished based on the shear stress thresholds found in literature.

1.8 Aim of this thesis

Blood trauma in rotary blood pumps is a major issue related to the therapy of end-stage heart failure. Severe complications such as thromboembolic events and bleeding can be directly linked to the damaging effects of the pump flow on blood components. Therefore, the reduction of blood trauma is a main objective in research and development of rotary blood pumps.

Clinically used pumps are different regarding working principle (radial or axial), design configuration (diffuser or volute), operating behavior (flat or steep characteristic curve) and bearing concept (mechanical contact bearings or contactless hydrodynamic or magnetic levitation). While survival rates are similar amongst the devices (Figure 5) with similar total adverse event rates, the clinically observed blood damage profile is slightly different [88,89].

Although the clinical effects have been well investigated and reported, fluid dynamics inside the pumps were hardly examined or at least not accessible for the scientific community. Therefore, a correlation of clinical findings and flow characteristics was not possible.

Thus, the aim of this thesis was to investigate state-of-the-art rotary blood pumps with the previously described methods to identify flow characteristics and potential links to blood damage. These findings should further be used to develop a less traumatic rotary blood pump design. The novel approach to achieve this was a multistage design that allows for a reduction of rotational speed and consequently circumferential velocities and shear stress.

2 Publications

In the subsequent sections of this chapter, the three publications, which emerged within the framework of this thesis, are presented following a brief summary of the objective, methods, and most important results.

2.1 Paper I:

Numerical Analysis of Blood Damage Potential of the HeartMate II and HeartWare HVAD Rotary Blood Pumps

In this work, CFD technique was utilized to compare the two most widely clinically used rotary blood pumps: the axial HeartMate II and the radial Heartware HVAD. The pump geometries were reconstructed based on manually taken dimensions from explanted devices. The flow fields were simulated on high resolution structured meshes, considering a constant viscosity for blood and using the Sliding Mesh approach and the k - ω SST turbulence model for one typical state of operation at 4.5 L/min and 80 mmHg. The rotational speed has therefore been adjusted for both pumps leading to 10,500 rpm for the HM II and 2,840 rpm for the HVAD which is in good agreement with measured operating points. The resulting flow fields were then analyzed regarding potential blood trauma, first by looking into global features of the flow to identify vortices or areas of high velocities, and second by examining the occurring shear stresses, since blood damage is connected to high shear stresses. Therefore, volumetric proportions of the flow domains exposed to certain viscous shear stress thresholds, below which no trauma was assumed (von Willebrand factor cleavage: 9 Pa, platelet activation: 50 Pa, and hemolysis: 150 Pa), and associated residence times were calculated. In addition, a hemolysis index based on a revised Eulerian transport approach was computed.

In both pumps, vortex formations were identified. In the HVAD, such a zone was observed in each blade channel. In the HM II, a vortex with a strong back flow was seen between the flow straightener and the impeller. Regarding shear stress distributions, in the HVAD the volumetric portion exposed to shear stress above 9 Pa was larger, while for the other thresholds the differences between the two pumps were not substantial. The calculation of hemolysis revealed that especially the gap regions in both pumps as well as the leading edges of the impeller and diffuser blades in the HM II and the volute tongue in the HVAD are areas of high hemolysis. Since the calculated hemolysis index was almost equal for the two pumps, it is reasonable to conclude an overall similar tendency to blood trauma in both pumps. Based on these findings, the actual state of the art was captured and a potential for improvements with a less-traumatic pump design was determined.



Numerical Analysis of Blood Damage Potential of the HeartMate II and HeartWare HVAD Rotary Blood Pumps

*Bente Thamsen, †Bastian Blümel, *Jens Schaller, †Christian O. Paschereit,
*Klaus Affeld, *Leonid Goubergrits, and *Ulrich Kertzscher

**Biofluid Mechanics Laboratory, Charité-Universitätsmedizin Berlin; and †Chair of Fluid Dynamics,
Hermann-Föttinger-Institut, Technische Universität Berlin, Berlin, Germany*

Abstract: Implantable left ventricular assist devices (LVADs) became the therapy of choice in treating end-stage heart failure. Although survival improved substantially and is similar in currently clinically implanted LVADs HeartMate II (HM II) and HeartWare HVAD, complications related to blood trauma are frequently observed. The aim of this study was to compare these two pumps regarding their potential blood trauma employing computational fluid dynamics. High-resolution structured grids were generated for the pumps. Newtonian flow was calculated, solving Reynolds-averaged Navier–Stokes equations with a sliding mesh approach and a $k-\omega$ shear stress transport turbulence model for the operating point of 4.5 L/min and 80 mm Hg. The pumps were compared in terms of volumes subjected to certain viscous shear stress thresholds, below which no trauma was assumed (von Willebrand factor cleavage: 9 Pa, platelet activation: 50 Pa, and hemolysis: 150 Pa), and associated residence times. Additionally, a hemolysis index was calculated based on a

Eulerian transport approach. Twenty-two percent of larger volumes above 9 Pa were observed in the HVAD; above 50 Pa and 150 Pa the differences between the two pumps were marginal. Residence times were higher in the HVAD for all thresholds. The hemolysis index was almost equal for the HM II and HVAD. Besides the gap regions in both pumps, the inlet regions of the rotor and diffuser blades have a high hemolysis production in the HM II, whereas in the HVAD, the volute tongue is an additional site for hemolysis production. Thus, in this study, the comparison of the HM II and the HVAD using numerical methods indicated an overall similar tendency to blood trauma in both pumps. However, influences of turbulent shear stresses were not considered and effects of the pivot bearing in the HM II were not taken into account. Further in vitro investigations are required. **Key Words:** Blood trauma—Left ventricular assist devices—Rotary blood pumps—Computational fluid dynamics—Blood damage.

Continuous flow left ventricular assist devices (LVADs) became the therapy of choice for treating patients with end-stage heart failure, even for destination therapy (1). However, remaining limitations result from adverse events like thrombosis, bleeding, and infections (2). Some are directly related to the adverse effects of the pump flow on the blood:

thrombosis and thromboembolic events, hemolysis, and bleeding. Currently, the most frequently clinically implanted LVADs are the HeartMate II (HM II; Thoratec Corp., Pleasanton, CA, USA) and the HeartWare HVAD (HeartWare International, Inc., Framingham, MA, USA), which received approval as bridge-to-transplant therapy by the Food and Drug Administration (FDA) of the USA in 2008 and 2012, respectively (3,4).

These devices differ regarding geometric and functional properties: while the HM II is an axial pump with pivot bearings to stabilize the impeller, the HVAD contains a centrifugal impeller that is supported with contactless magnetic and hydrodynamic bearings. This leads to completely different pump designs. Nevertheless, clinical outcome is comparable with both devices. In the HM II post-FDA

doi:10.1111/aor.12542

Received December 2014; revised April 2015.

Address correspondence and reprint requests to Mrs. Bente Thamsen, Biofluidmechanics Laboratory, Charité Universitaetsmedizin Berlin, Augustenburger Platz 1, Forum 4, Berlin, Berlin 13353, Germany. E-mail: bente.thamsen@charite.de

Presented in part at the 22nd Congress of the International Society for Rotary Blood Pumps held September 25–27, 2014 in San Francisco, CA, USA.

approval trial, a 1-year survival rate of 85% was achieved (5). The same percentage is reported for the HVAD in the bridge-to-transplant and continued-access protocol trial (6). But differences in adverse events profiles and coagulation are also reported. Lalonde et al. compared 33 HM II and 13 HVAD recipients and found that patients supported with the HVAD had a significantly higher incidence of gastrointestinal bleeding (31% vs. 0%) and stroke (44% vs. 10%) (7). Birschmann et al. analyzed 10 HM II and 10 HVAD patients and detected significantly higher levels of fibrin-split products indicating a higher activation of the coagulation system in HVAD patients, whereas in HM II patients the levels of lactate dehydrogenase (LDH) were significantly higher, indicating increased hemolysis (8).

However, the underlying causes are unclear. One method to provide insight in hemocompatibility is computational fluid dynamics (CFD). CFD has been widely used in the development process of rotary blood pumps: to describe hydrodynamic performance, to optimize pump design as well as to assess potential blood trauma (9–11). In that context, Fraser et al. presented a detailed comparison of numerical blood damage parameters in three implantable axial pumps and two extracorporeal centrifugal pumps (12).

In this study, CFD is used to compare the HVAD and the HM II pumps. To the authors' knowledge, these two implantable LVADs have not been compared in terms of flow fields, shear stresses, and hemolysis so far.

Therefore, the aim of this study was to investigate and compare the flow features of the HM II and the HVAD associated with blood damage. On that account, two different approaches were taken: first,

the distribution of shear stresses in the flow fields in the two pumps was investigated. Similar to Fraser et al., the results were compared regarding different shear stress levels below which no trauma of a specific blood component was assumed. Also, residence times were computed as a rough measure for exposure times to these shear stresses.

In addition and as a second approach, hemolysis indices for both pumps were calculated following Goubergrits (13). Thereby, damage that is experienced by the blood on its way through the pump is integrated using a new Eulerian transport equation. This approach is beneficial because it allows the visualization of damage sites in the pump, has the same resolution as the CFD solution, and takes the whole numerical domain into account.

MATERIALS AND METHODS

Geometry

Because the details of the geometry of the HM II and HVAD are not open to public access, dimensions of the two pumps were derived from explanted pumps. Manual measurements were performed to capture the geometry. Computer-aided design models were generated using SolidWorks software (SolidWorks, Dassault Systems, Walton, MA, USA), resulting in detailed geometries of both pumps (Fig. 1).

A summary of geometric and functional parameters of the two pumps is given in Table 1. The HM II consists of a flow straightener, an axial impeller, and a diffuser with three blades each. The HVAD has a centrifugal four-blade impeller and a volute casing. In vivo, the position of the magnetically and hydrodynamically levitated rotor depends on the specific

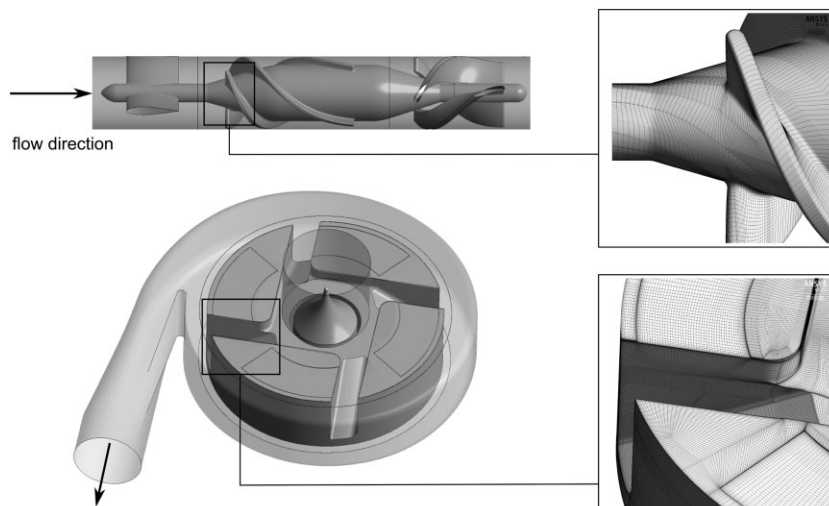


FIG. 1. Reverse engineered computer-aided design (CAD) models of the HM II (top left) and the HVAD LVAD (bottom left). Additionally, details of the surface mesh at the blade inlet area of the HM II (top right) and at the blade channel and upper bearing gap of the HVAD (bottom right) are shown.

TABLE 1. Geometric and functional properties of the HM II and the HVAD LVAD

	Pump type	Bearing type	Fluid volume	Rotor diameter	Gap	Speed range
HM II	Axial	Cup-socket ruby bearing	7.7 mL	12 mm	100 μm	6000–15 000 rpm
HVAD	Radial	Magnetic and hydrodynamic	11.8 mL	34 mm	40 μm (top)/160 μm (bottom)	1800–4000 rpm

operating point and adjusts itself passively in a way that the resulting force of the bearing balances the weight of the rotor. For a typical operating point in this study, the rotor position was fixed and assumed so that a top bearing gap between 40 and 230 μm emerged due to the tapered surface and the bottom gap was 160 μm .

CFD

Structured, hexagonal meshes for each pump geometry were created using commercial grid generator software ICEM (ANSYS ICEM CFD, Inc., Canonsburg, PA, USA) resulting in 14.5 million nodes for the HVAD. In order to economize the computational calculations, we took advantage of the 120° rotational symmetry of the HM II's axial design and generated a periodic mesh with 3.5 million nodes matching a third of the full geometry. Because areas of high shear are of special interest, adequate grid refinements were provided at the walls to resolve the near wall flow. Mesh quality criteria like orthogonal angle, mesh expansion factor, and aspect ratio were monitored to be in the demanded range for the solver. The dimensionless distance from the wall Y_{plus} (14) is below 2 for all cells adjacent to a wall. To investigate grid independence, three coarser grids for the HM II with 2.8, 1.9, and 1.4 million nodes were created by global scaling of the cell size while keeping the initial spacing at the walls constant.

The calculations were conducted using a commercial CFD solver (ANSYS CFX, ANSYS, Inc., Canonsburg, PA, USA). Blood was modeled as a Newtonian fluid with a constant density of 1050 kg/m^3 and a dynamic viscosity of 3.5 mPas. The $k-\omega$ shear stress transport model was used to simulate turbulence (15).

As boundary conditions at the pump inlet, a mass flow inlet with a fixed flow rate was set and fully developed turbulence was assumed with the zero gradient condition set. The outlet was configured as an opening with a relative pressure in the order of the pump pressure head.

We focused our comparative study on the same operating point for both pumps, namely 4.5 L/min at 80 mm Hg, as a typical operating point for LVADs. The appropriate rotor speed was determined by stationary simulations with various rotor speeds using

the frozen rotor approach. Thereby, the pressure head had to reach a nearly constant value equal to the desired pressure head with an accuracy of 1 mm Hg. The stationary solution was then used to initialize the subsequent transient simulation. We applied the transient rotor–stator interface that allowed an actual rotation of the rotor domain relative to the static domains of the pumps as can be found in the ANSYS CFX-Solver Theory Guide (14). The time step was adjusted with respect to the rotational speed to yield a 2° rotation per step (HVAD: 0.118 ms; HM II: 0.032 ms). The transient simulation was run using second-order schemes in space and time until the pressure head showed a smooth periodic behavior with a constant mean pressure head. Velocity, pressure, and turbulent viscosity were averaged over at least five rotations after the flow field stabilized.

Validation

To validate the numerical results, the characteristic curves of the HM II and HVAD pumps were measured experimentally for a specific speed of each pump. A distilled water–glycerol mixture (37.5% of 99.5% pure glycerin) was used to simulate the blood viscosity of 3.5 mPas at room temperature of 24°C. The flow rate was obtained with an in-line ultrasonic flow probe (Transonic, Inc., Ithaca, NY, USA) and pressures at a small distance to the inflow and outflow cannula were acquired via disposable pressure transducers (ASensTec GmbH, Inning, Germany). The measured values at 4.5 L/min had to be in agreement with the computational operating point of 80 mm Hg.

Volumetric analysis

For the investigation of the flow fields with regard to blood damage, two parameters are of main importance: the shear stress level on the one hand and the exposure time to these shear stresses on the other hand. Scalar representative viscous shear stresses τ in the flow field were computed using the shear strain rate ssr defined as $ssr = \sqrt{2 \cdot S_{ij} S_{ij}}$, where S_{ij} is the strain rate tensor, and the dynamic viscosity μ :

$$\tau = ssr \cdot \mu.$$

The impact of turbulent features, namely the equivalent scalar shear stress for a certain turbulent

flow that is acting on the blood cells, is still unclear (16,17). Nevertheless, to investigate turbulence, the eddy viscosity μ_{eddy} was used instead of the dynamic viscosity to calculate a turbulent parameter τ_{turb} with the dimension of shear stress

$$\tau_{turb} = SSR \cdot \mu_{eddy}$$

The eddy viscosity used here is calculated based on the turbulence model by the solver as described in the ANSYS CFX-Solver Theory Guide (14). The residence time as a rough measure for exposure time for each computational cell was approximated using the velocity magnitude u in a cell and the cell size defined as the cubic root of the cell volume V , so that

$$t = \frac{\sqrt[3]{V}}{u}$$

For both pumps, shear stresses and residence times were computed for the chosen operating point and then analyzed using volumetric histograms. Subsequently, the results were interpreted regarding different viscous shear stress levels below which no trauma of a specific blood component is assumed. According to Fraser et al. (12), three shear stress thresholds for three different types of blood trauma occurring in LVADs were used.

For von Willebrand factor (vWF) cleavage, which is seen in patients supported with LVADs (18–20), the threshold was set to 9 Pa. The threshold for platelet activation, which is essential for thrombus formation and hemostasis, was set to 50 Pa. Hemolysis was included in the analysis with a threshold of 150 Pa. Therefore, the absolute volume fractions of the pumps in which blood was exposed to these specified shear stress levels were computed to compare the pumps.

Hemolysis indices

The calculation of hemolysis indices is of great interest for the evaluation of potential blood trauma. A common practice is to calculate a damage index based on power law models like that from Giersiepen et al. based on data of Wurzinger et al. (21). Although it is well known that the use of this equation leads to overestimation of damage and does not reflect the real situation, it is still considered helpful for engineering tasks where devices are compared and optimized. The formula describes the amount of released hemoglobin ΔHb in relation to the total hemoglobin Hb , while it takes the exposure time and the shear stress acting on the red blood cells into

account. The data basis has been derived for laminar shear stresses in a range of 57–255 Pa during exposure times of 7–700 ms (22):

$$\frac{\Delta Hb}{Hb} = HI = A \cdot t^\alpha \cdot \tau^\beta \quad (1)$$

with $A = 3.62 \cdot 10^{-7}$, $\alpha = 0.785$, $\beta = 2.416$ where t is in s, τ in Pa, and HI ranges from 0 to 1.

The distribution of plasma-free hemoglobin was computed by solving a Eulerian transport equation as previously described in Garon and Farinas and Farinas et al. (23,24) in which the entire flow field is considered and which has been shown to be more reliable when relatively comparing different devices (25). For the implementation, we revised the proposal by Goubergrits (13). The power law (Eq. 1) was differentiated in time to obtain the rate of change of hemolysis. The time Δt on the right hand side is replaced by rearranging the power law to $\Delta t = \sqrt[3]{HI/(A \cdot \tau^\beta)}$. In this way, a production term for the hemolysis is derived that incorporates the shear stress and the damage from the previous time step.

$$\frac{dHI}{dt} = \tilde{A} \cdot \tau^{\tilde{\beta}} \cdot HI^{\tilde{\gamma}}, \text{ where } \tilde{A} = \alpha \sqrt[3]{A}, \quad (2)$$

$$\tilde{\beta} = \beta/\alpha, \text{ and } \tilde{\gamma} = 1 - \frac{1}{\alpha}$$

This accounts for the non-linear dependency of the blood damage on the exposure time t . Eq. 2 was implemented in CFX as a source term for a mass transport and solved using the viscous shear stresses on the pre-calculated instantaneous flow field until the amount of calculated plasma-free hemoglobin reached a steady state. The HI was defined as the integral of the production over the entire domain in relation to the mass flow of undamaged blood entering the pump.

RESULTS

Mesh independence

The pressure head of 80 mm Hg at 4.5 L/min of flow was achieved at 10 500 rpm for the HM II and 2835 rpm for the HVAD. The difference between the finest and the next coarser grids was only 0.6% in pressure head and 2% regarding volumes that were exposed to viscous shear stresses above 150 Pa.

Validation

The numeric simulations were validated by comparison with the measurements in an experimental mock circuit. The characteristic curves are shown in

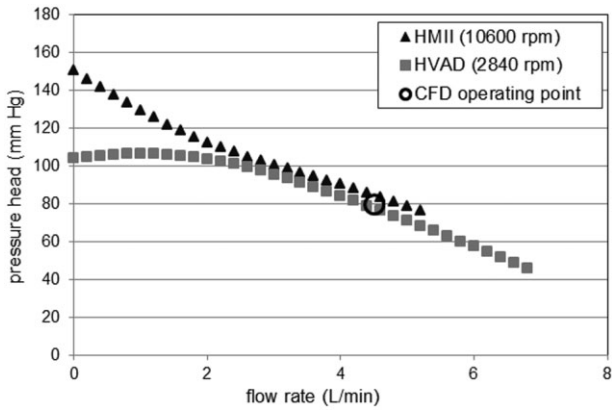


FIG. 2. Measured head curves of the HM II and HVAD and the computational operating point. The percentage difference to the computational operating point was at maximum 5%.

Fig. 2. The HM II curve has a steep progression over the entire flow range, which is typical for axial pumps, while the centrifugal HVAD shows a flatter trend at lower flow rates. In the area of the chosen operating point, the curves are almost parallel. The measured pressure head for the operating flow rate of 4.5 L/min was 83 mm Hg and 76 mm Hg for the

HM II and the HVAD, respectively. Thus, the percentage difference to the computational operating point was at most 5%.

Flow field

Figure 3 shows 30 exemplary streamlines in the HM II and the HVAD. Typical flow structures in the two pumps were revealed: in the HM II, a recirculation zone between the flow straightener and the rotor inlet was seen. Furthermore, a strong backflow in the hub area of the diffuser was identified. In the HVAD, vortices developed in the blade channels.

Viscous and turbulent shear stresses

Volumetric histograms of the viscous and turbulent shear stresses in the pumps were computed and are presented in Fig. 4. The volumetric distribution of shear stresses differs in both pumps. In the HVAD, volumes that are subjected to viscous shear stresses lower than 100 Pa are larger. In the HM II, slightly larger volumes are exposed to shear stresses above this value.

The volumetric distribution of the turbulent shear stresses shows a large difference between the two pumps. Larger volumetric portions in the HVAD are

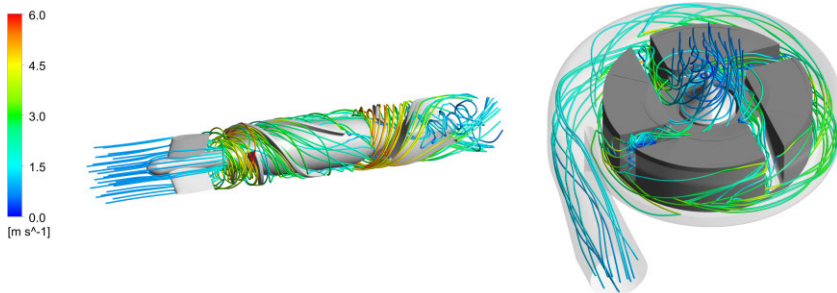


FIG. 3. Thirty exemplary streamlines in the HM II (left) and the HVAD (right). The scale refers to velocity in the range of 0 to 6 m/s (for color figures please refer to online version). In the HM II, a vortex was seen at the diffuser outlet. In the HVAD, vortices developed in the blade channels.

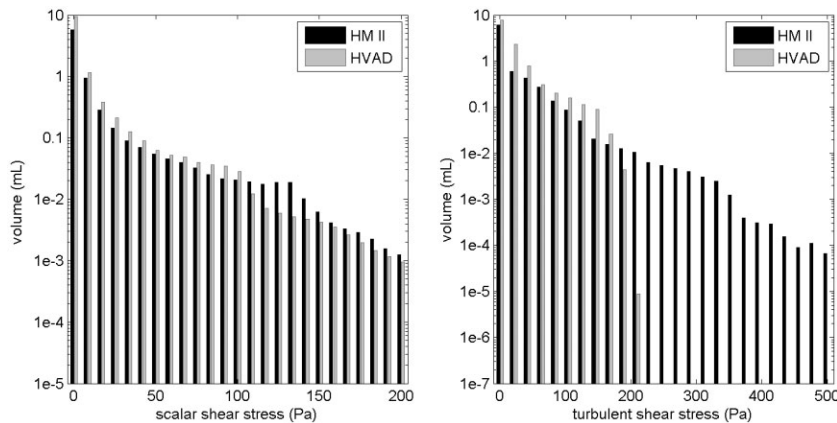


FIG. 4. Volumetric histograms for viscous shear stresses and for turbulent shear stresses computed using the eddy viscosity in the HM II and the HVAD at 4.5 L/min and 80 mm Hg. For better illustration, the y-axis is scaled logarithmically. The figure allows a comparison of the shear stress distributions in the two pumps.

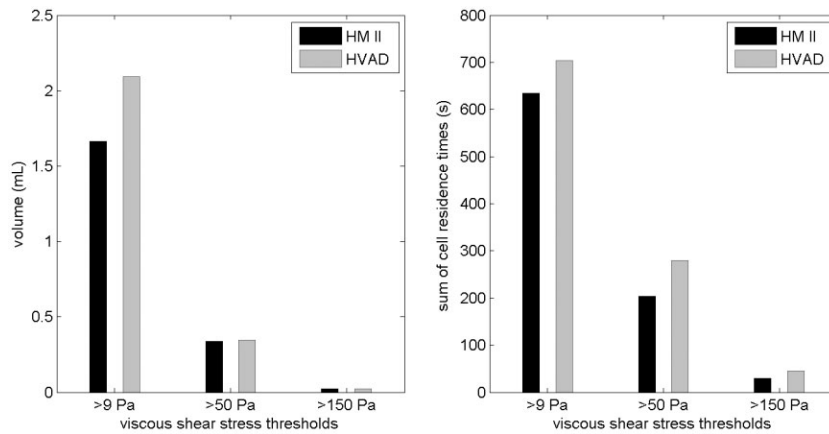


FIG. 5. Volume fractions (left) subjected to specified viscous shear stress thresholds for vWF damage (9 Pa), platelet activation (50 Pa), and hemolysis (150 Pa) and corresponding sums of cell residence times (right).

exposed to turbulent shear stresses below 170 Pa, but no turbulent shear stresses beyond 210 Pa occur. In contrast, the HM II has a much broader distribution with values reaching slightly above 500 Pa.

Volumes and residence times with specified shear stress thresholds

In Fig. 5, the volume fractions of the pumps are displayed in which blood was exposed to viscous shear stresses above the specified shear stress levels. There is a difference for shear stresses beyond the 9 Pa threshold, so that the HVAD seems to have larger areas with vWF damage. For the higher shear stresses, which correspond to potential hemolysis and platelet activation, both pumps have a very similar volume fraction. The sum of the cell residence times at these shear stresses is higher for the HVAD for all thresholds.

Hemolysis indices

With the Eulerian approach based on Goubergrits' suggestion (13), the hemolysis indices are nearly equal for both pumps, namely 3.75×10^{-5} for the HVAD and 3.85×10^{-5} for the HM II. The sites of hemolysis production in each pump are depicted in Fig. 6. It can be seen that the gap regions are particularly prone to producing hemolysis. In the HM II, the inlet regions of the rotor blades and the diffuser

blades also have a high hemolysis production. Moreover, the near blade region at the outer housing wall in the diffuser and the outlet blade edge seem to be sites for red blood cell damage. In the HVAD, in addition to the gap region, the volute tongue is a site for hemolysis production.

DISCUSSION

In this study, the flow fields of the HVAD and the HM II and potential differences in hemocompatibility were investigated. First, the pumps were compared in terms of volumetric distribution of shear stresses and residence times, as well as with regard to specified thresholds for blood damage. These thresholds were adopted from Fraser et al. (12) and are based on literature (vWF cleavage [26,27], platelet activation [28], hemolysis [29]). However, other values for vWF cleavage (30,31), platelet activation (32), and red blood cell damage (33,34) were also reported. It must be noted that the choice of the threshold level may influence the results. For the sake of comparability, we followed the suggestion by Fraser's group. A single threshold value certainly fails to account for the real damaging effects, but this method of classification still remains a simple and expressive approach for characterizing and comparing devices and might provide an indication regarding blood damage potential.

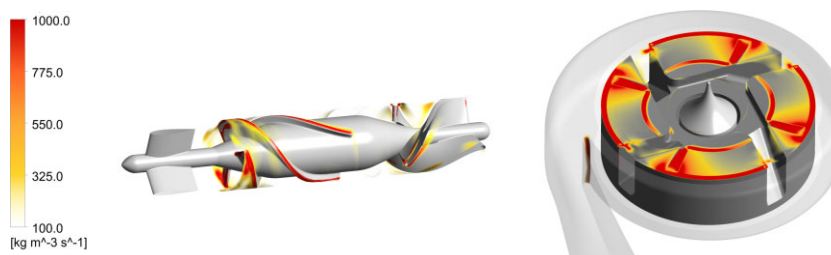


FIG. 6. Sites of high hemolysis production in the HM II (left) and HVAD pump (right) based on the source term from the Eulerian model. The gap regions are particularly prone to producing hemolysis, as well as the leading edges of the blades in the HM II and the volute tongue in the HVAD. For color figures please refer to online version.

Larger volumes that are exposed to viscous shear stresses above 9 Pa can be seen in the HVAD. Thus, vWF cleavage might happen to a greater degree in the radial pump. However, no significant differences in relation to vWF damage among HM II and HVAD were found *in vivo* (35). Regarding shear stresses above 50 Pa and above 150 Pa, the volumetric differences between the two pumps are marginal. However, the overall residence times are longer in the HVAD for all thresholds, which consequently suggests higher tendencies to platelet activation and hemolysis in the HVAD. The clinical findings of Lalonde et al., who reported a significantly higher incidence of gastrointestinal bleeding and strokes for the HVAD (7), and Birschmann et al., whose results indicated a higher activation of the coagulation system in HVAD patients (8), would support these findings. However, Birschmann et al. also reported significantly higher levels of LDH in HM II patients. Both studies include only a small group of patients (46 and 20 patients, respectively).

It may seem unfair that absolute and not relative volumes were compared, as the HVAD has a larger total volume. However, as the flow rate is the same for both pumps and consequently the same amount of blood passes the entire pump volume during the same time, it is justified to compare the absolute volumes.

Differences in shear stress distribution may be due to the different bearing technology used in the pumps: due to the hydrodynamic bearing of the HVAD, the gap area between rotor blades and housing is much wider. The HM II, in contrast, uses a contact bearing where no additional gaps emerge that may have an impact on blood damage. It has to be mentioned that the gap sizes in the HVAD were assumed to be typical for the studied operating point but were not measured *in vitro* or *in vivo*. The good accordance of the computational results with the measured curves is affirming this assumption. Regarding the contact bearing of the HM II, the heat generation, which may influence the blood components, is not considered in the study.

The Eulerian transport leads to quite similar values for the hemolysis index of both pumps. This result indicates a similar tendency to cause blood trauma. The visualization of the hemolysis production sites thereby reveals a considerable influence of the gap areas in both pumps. Additional sites for high blood damage are the leading edges of the blades as well as the rotor and diffusor inlet regions in the HM II and the volute tongue in the HVAD.

As an important issue, only viscous shear stresses were considered for the derivation of the hemolysis

index, although turbulent shear stresses differ substantially in both pumps. This approach is supported by Taskin's suggestion to disregard the turbulent Reynolds stresses on the grounds that this is a rather statistical quantity that does not directly reflect physical forces on the blood cells (36). Arvand et al. also did not include turbulent shear stresses and argued with the high sensitivity of simulated turbulence on the specific way of numerical implementation (37). Contrarily, turbulence has an impact on blood damage (38–40) and should be included in an analysis. Here, the blood damage resulting from turbulent effects may be much higher in the HM II pump as the range of turbulent stresses is twice as high as in the HVAD. This gap of knowledge about the turbulent effects on blood damage requires further investigation.

Some limitations have to be mentioned. The CFD method is associated with a number of uncertainties. First of all, the geometry was manually measured, which could lead to deviations compared with the original designs. The gap in the HVAD was assumed and set to a constant value in order to fix the vertical rotor position for the simulations.

Furthermore, the study was performed for a single operating point only, which was assumed to be a typical operating point for LVADs. Also, simplified flow conditions, such as a constant mass flow rate, were used for the simulations but do not reflect the real situation of pumps implanted into a beating heart. Moreover, the non-Newtonian characteristics of blood were not considered. Additionally, errors may result from the numerical method that requires discretization of the physical domain and the governing equations.

Finally, important factors contributing to hemocompatibility of LVADs cannot be included in a CFD study. For instance, biochemical properties and structure of blood-contacting surfaces are not considered. Additionally, therapeutic strategies and patient selection play a crucial role in hemocompatibility of such devices.

CONCLUSIONS

This study provides novel insights into the hemocompatibility properties of currently clinically used blood pumps. The employed methods and findings may contribute to the development process of next-generation devices with reduced blood trauma. The comparison of the HeartMate II and the HeartWare using computational fluid dynamics revealed a larger volume exposed to shear stresses above 9 Pa in the HVAD, which may indicate a

higher tendency to von Willebrand factor cleavage. For platelet activation and hemolysis criteria, the volumes were almost equal in the two pumps. Residence times were higher in the HVAD, but the hemolysis index calculated with a new Eulerian transport approach was similar for the two pumps, too. Thus, the results might indicate an overall similar tendency to cause blood trauma for the HVAD and the HM II. In both pumps, the highest damage was seen in the gap regions and furthermore at the leading edges of the blades in the HM II and the volute tongue in the HVAD. Further in vitro investigation is encouraged to support the findings.

Acknowledgments: This work was supported by a grant from the Investitionsbank Berlin (IBB) (10153412) supported by the “Europäischer Fond für regionale Entwicklung” (EFRE).

REFERENCES

- McMurray JJV, Adamopoulos S, Anker SD, et al. ESC guidelines for the diagnosis and treatment of acute and chronic heart failure 2012. *Eur Heart J* 2012;33:1787–847.
- Molina EJ, Boyce SW. Current status of left ventricular assist device technology. *Semin Thorac Cardiovasc Surg* 2013;25:56–63.
- Pagani FD, Miller LW, Russell SD, et al. Extended mechanical circulatory support with a continuous-flow rotary left ventricular assist device. *J Am Coll Cardiol* 2009;54:312–21.
- Aaronson KD, Slaughter MS, Miller LW, et al. Use of an intrapericardial continuous-flow, centrifugal pump in patients awaiting heart transplantation. *Circulation* 2012;125:3191–200.
- Starling RC, Naka Y, Boyle AJ, et al. Results of the post-U.S. Food and Drug Administration-approval study with a continuous flow left ventricular assist device as a bridge to heart transplantation: a prospective study using the INTERMACS (Interagency Registry for Mechanically Assisted Circulatory Support). *J Am Coll Cardiol* 2011;57:1890–8.
- Slaughter MS, Pagani FD, McGee EC, et al. HeartWare ventricular assist system for bridge to transplant: combined results of the bridge to transplant and continued access protocol trial. *J Heart Lung Transplant* 2013;32:675–83.
- Lalonde SD, Alba AC, Rigobon A, et al. Clinical differences between continuous flow ventricular assist devices: a comparison between HeartMate II and HeartWare HVAD. *J Card Surg* 2013;28:604–10.
- Birchmann I, Dittrich M, Eller T, et al. Ambient hemolysis and activation of coagulation is different between HeartMate II and HeartWare left ventricular assist devices. *J Heart Lung Transplant* 2014;33:80–7.
- Behbahani M, Behr M, Hormes M, et al. A review of computational fluid dynamics analysis of blood pumps. *Eur J Appl Math* 2009;20:363–97.
- Su B, Chua LP, Lim TM, Zhou T. Evaluation of the impeller shroud performance of an axial flow ventricular assist device using computational fluid dynamics. *Artif Organs* 2010;34:745–59.
- Chiu W-C, Slepian MJ, Bluestein D. Thrombus formation patterns in the HeartMate II ventricular assist device: clinical observations can be predicted by numerical simulations. *ASAIO J* 2014;60:237–40.
- Fraser KH, Zhang T, Taskin ME, et al. A quantitative comparison of mechanical blood damage parameters in rotary ventricular assist devices: shear stress, exposure time and hemolysis index. *J Biomech Eng* 2012;34:081002–1–11.
- Goubergrits L. Numerical modeling of the blood damage: current status, challenges and future prospects. *Expert Rev Med Devices* 2006;3:527–31.
- ANSYS, Inc. ANSYS CFX-Solver Theory Guide, Release 15.0, 2013. Available at: <http://148.204.81.206/Ansys/150/ANSYS%20CFX-Solver%20Theory%20Guide.pdf>.
- Menter FR. Two-equation eddy-viscosity turbulence models for engineering applications. *AIAA J* 1994;32:1598–605.
- Quinlan NJ, Dooley PN. Models of flow-induced loading on blood cells in laminar and turbulent flow, with application to cardiovascular device flow. *Ann Biomed Eng* 2007;35:1347–56.
- Antiga L, Steinman DA. Rethinking turbulence in blood. *Biorheology* 2009;46:77–81.
- Geisen U, Heilmann C, Beyersdorf F, et al. Non-surgical bleeding in patients with ventricular assist devices could be explained by acquired von Willebrand disease. *Eur J Cardiothorac Surg* 2008;33:679–84.
- Steinlechner B, Dworschak M, Birkenberg B, et al. Platelet dysfunction in outpatients with left ventricular assist devices. *Ann Thorac Surg* 2009;87:131–7.
- Crow S, Chen D, Milano C, et al. Acquired von Willebrand syndrome in continuous-flow ventricular assist device recipients. *Ann Thorac Surg* 2010;90:1263–9.
- Giersiepen M, Wurzingler LJ, Opitz R, Reul H. Estimation of shear-related blood damage in heart valve prostheses—in vitro comparison of 25 aortic valves. *Int J Artif Organs* 1990;13:300–6.
- Wurzingler LJ, Opitz R, Blasberg P, Schmid-Schönbein H. Platelet and coagulation parameters following millisecond exposure to laminar shear stress. *Thromb Haemost* 1985;54:381–6.
- Garon A, Farinas M-I. Fast three-dimensional numerical hemolysis approximation. *Artif Organs* 2004;28:1016–25.
- Farinas M-I, Garon A, Lacasse D, N’dri D. Asymptotically consistent numerical approximation of hemolysis. *J Biomech Eng* 2006;128:688–96.
- Taskin ME, Fraser KH, Zhang T, Wu C, Griffith BP, Wu ZJ. Evaluation of Eulerian and Lagrangian models for hemolysis estimation. *ASAIO J* 2012;58:363–72.
- Tsai HM, Sussman II, Nagel RL. Shear stress enhances the proteolysis of von Willebrand factor in normal plasma. *Blood* 1994;83:2171–9.
- Di Stasio E, De Cristofaro R. The effect of shear stress on protein conformation. Physical forces operating on biochemical systems: the case of von Willebrand factor. *Biophys Chem* 2010;153:1–8.
- Hellums JD. 1993 Whitaker Lecture: biorheology in thrombosis research. *Ann Biomed Eng* 1994;22:445–55.
- Leverett LB, Hellums JD, Alfrey CP, Lynch EC. Red blood cell damage by shear stress. *Biophys J* 1972;12:257–73.
- Siedlecki CA, Lestini BJ, Kottke-Marchant K, et al. Shear-dependent changes in the three-dimensional structure of human von Willebrand factor. *Blood* 1996;88:2939–50.
- Vergauwe RMA, Uji-i H, De Ceunynck K, et al. Shear-stress-induced conformational changes of von Willebrand factor in a water-glycerol mixture observed with single molecule microscopy. *J Phys Chem B* 2014;118:5660–9.
- Alemu Y, Bluestein D. Flow-induced platelet activation and damage accumulation in a mechanical heart valve: numerical studies. *Artif Organs* 2007;31:677–88.
- Nevaril CG, Lynch EC, Alfrey CP, Hellums JD. Erythrocyte damage and destruction induced by shearing stress. *J Lab Clin Med* 1968;71:784–90.
- Paul R, Apel J, Klaus S, Schügner F, Schwindke P, Reul H. Shear stress related blood damage in laminar coquette flow. *Artif Organs* 2003;27:517–29.
- Frumkin A. Entwicklung des Von-Willebrand-Syndroms und sein Einfluss auf Blutungskomplikationen bei Patienten

- mit verschiedenen nicht-pulsatilen linksventrikulären Kreislaufunterstützungssystemen. *Dissertation at the German Heart Institute (DHZB)*. 2014.
36. Taskin ME, Fraser KH, Zhang T, et al. Computational characterization of flow and hemolytic performance of the UltraMag blood pump for circulatory support. *Artif Organs* 2010;34:1099–113.
 37. Arvand A, Hormes M, Reul H. A validated computational fluid dynamics model to estimate hemolysis in a rotary blood pump. *Artif Organs* 2005;29:531–40.
 38. Sallam AM, Hwang NHC. Human red blood cell hemolysis in a turbulent shear flow: contribution of Reynolds shear stresses. *Biorheology* 1984;21:783–97.
 39. Kameneva MV, Burgreen GW, Kono K, Repko B, Antaki JF, Umezu M. Effects of turbulent stresses upon mechanical hemolysis: experimental and computational analysis. *ASAIO J* 2004;50:418–23.
 40. Yen J-H, Chen S-F, Chern M-K, Lu P-C. The effect of turbulent viscous shear stress on red blood cell hemolysis. *J Artif Organs* 2014;17:178–85.

2.2 Paper II: Experimental and numerical investigation of an axial rotary blood pump

The scope of this paper was to investigate the flow characteristics at the wall, where the interaction between blood and artificial surface takes place, in the HM II. Therefore, the experimental methods described in chapters 1.6.2 and 1.6.3 were adapted. Hence, an experimental setup with a three times upscaled model of the HM II pump was built which was optically accessible. The Wall Particle Image Velocimetry (Wall PIV) method was used for flow measurements close to the inner housing wall and inside the impeller gap region. On this basis, wall shear stresses (WSS) were derived for 13 different operation points. The maximum WSS were above 150 Pa, occurred in the gap region at the upstream third of the impeller blades and increased linearly with pressure head. The paint erosion method was performed for only one operation point and gave insight into the flow patterns on the surfaces of the flow straightener, impeller, and diffuser. The paint streak images were further post-processed in a way that the paint distribution on the surface was color-mapped from blue (still a thick layer of paint) to red (no paint). In this way, areas with bad washout, which are critical regions with regard to thrombus formation, and regions with good washout and thus potentially high shear stresses critical for blood damage were identified.

The experimental results were directly compared to results of a CFD simulation using the previously described method for an enlarged model of the pump.

Overall good agreement of CFD and experimental results was observed which includes the location, magnitude, and direction of the maximum and minimum wall shear stresses, and the presence of recirculation zones on the pump stators. Thus, RANS-CFD, seems to be a valid tool for the assessment of flow fields in axial rotary blood pumps.

Experimental and Numerical Investigation of an Axial Rotary Blood Pump

*Chan Yong Schüle, *Bente Thamsen, †Bastian Blümel, *Michael Lommel,
*Tamer Karakaya, †Christian Oliver Paschereit, *Klaus Affeld, and *Ulrich Kertzscher

**Biofluid Mechanics Laboratory, Charité–Universitätsmedizin Berlin; and †Chair of Fluid Dynamics, Hermann-Föttinger-Institut, Technische Universität Berlin, Berlin, Germany*

Abstract: Left ventricular assist devices (LVADs) have become a standard therapy for patients with severe heart failure. As low blood trauma in LVADs is important for a good clinical outcome, the assessment of the fluid loads inside the pump is critical. More specifically, the flow features on the surfaces where the interaction between blood and artificial material happens is of great importance. Therefore, experimental data for the near-wall flows in an axial rotary blood pump were collected and directly compared to computational fluid dynamic results. For this, the flow fields based on unsteady Reynolds-averaged Navier–Stokes simulations-computational fluid dynamics (URANS-CFD) of an axial rotary blood pump were calculated and compared with experimental flow data at one typical state of operation in an enlarged model of the pump. The focus was set on the assessment of wall shear stresses (WSS) at the housing wall and rotor gap region by means of the wall-particle image velocimetry technique, and the visualization of near-wall flow structures on the inner pump surfaces by a paint erosion method. Additionally, maximum WSS and tip

leakage volume flows were measured for 13 different states of operation. Good agreement between CFD and experimental data was found, which includes the location, magnitude, and direction of the maximum and minimum WSS and the presence of recirculation zones on the pump stators. The maximum WSS increased linearly with pressure head. They occurred at the upstream third of the impeller blades and exceeded the critical values with respect to hemolysis. Regions of very high shear stresses and recirculation zones could be identified and were in good agreement with simulations. URANS-CFD, which is often used for pump performance and blood damage prediction, seems to be, therefore, a valid tool for the assessment of flow fields in axial rotary blood pumps. The magnitude of maximum WSS could be confirmed and were in the order of several hundred Pascal. **Key Words:** Axial blood pump—HeartMate II—Wall shear stress—Unsteady Reynolds-averaged Navier—Stokes simulations—Computational fluid dynamics—Flow visualization—Paint erosion method—Wall-particle image velocimetry.

Intracorporeal rotary blood pumps are widely used for ventricular support of patients with left heart failure. The main purpose of an implanted blood pump is threefold: supporting the natural recovery of a dysfunctional heart, bridging the time until transplantation, or destination therapy if organ transplantation is impossible (1).

Global properties of blood pumps, such as the dependency of blood flow rate on pressure head and

rotational speed, as well as the hydrodynamic efficiency, can be easily characterized experimentally and are essential for the appropriate (regulated) heart support. It is however also important to understand the flow inside a blood pump in detail in order to avoid complications related to blood damage, because blood damage was experimentally shown to be strongly linked to shear stress loading and residence time of the blood (2). The consequences of blood damage (3) can be thrombus formation due to the activation of platelets, hemolysis, and interference with the coagulation system (e.g., by cleavage of the von Willebrand factor).

For this reason, several experimental studies on flow fields in ventricular assist devices (VADs), especially in terms of possible pump design

doi: 10.1111/aor.12725

Received October 2015; revised December 2015.

Address correspondence and reprint requests to Chan Yong Schüle, Biofluid Mechanics Laboratory, Charité–Universitätsmedizin Berlin, Augustenburger Platz 1, 13353 Berlin, Germany. E-mail: chan-yong.schuele@charite.de

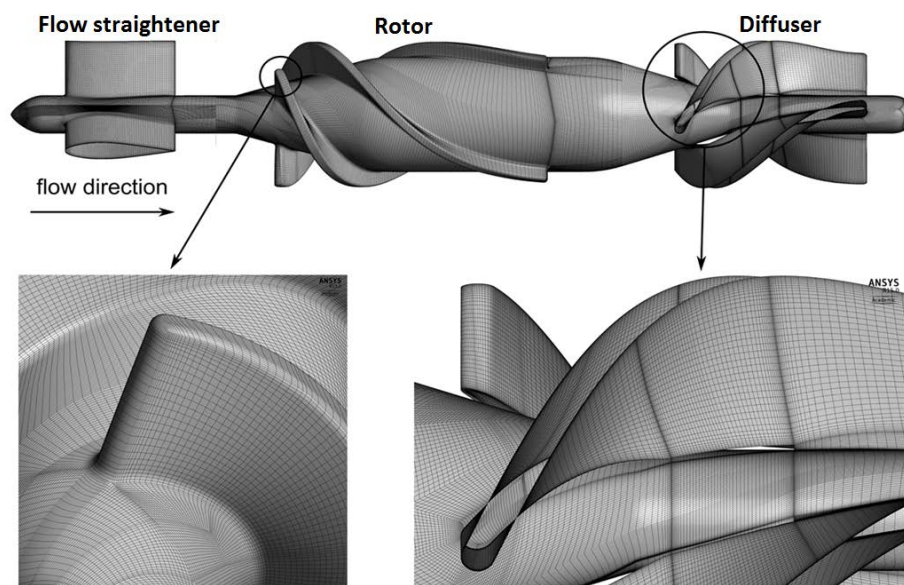


FIG. 1. Surface imprint of the numerical grid for RANS simulations.

improvement, have been published. For radial pumps, data can be found on the qualitative estimation of wall shear stress (WSS) and recirculation zones based on flow visualizations (4), direct measurements of impeller gap flow rates and WSS in a 5:1 enlarged model with intrusive hot or cold wire anemometry (5), or noninvasive direct WSS measurements with surface-mounted hot film sensors (6). Optical velocity measurements such as the laser Doppler velocimetry (7) or particle image velocimetry (PIV) (8) were also performed. The database for axial rotary blood pumps is less broad, though. Some publications exist on velocity profiles derived from PIV measurements on prototype axial blood pumps (9,10). Semiquantitative data from oil dot surface flow visualization were presented by Wu et al. (11), also on a prototype mixed-flow blood pump. Comparisons of computational fluid dynamics (CFD) with experimentally obtained particle tracks in a microaxial blood pump were presented by Apel et al. (12) and qualitative visualization with particle tracking by Kerrigan et al. (13) or Sieß (14). To the authors' knowledge, there are no publications regarding WSS measurements of currently implanted pumps such as the axial HeartMate II (HMII; Thoratec Corp., Pleasanton, CA, USA). At present the HMII is the most frequently implanted pump with >15 000 implants worldwide (1). It has been in clinical use since the beginning of the century and was approved by the Food and Drug Administration as a bridge to transplant in 2009 (15). Therefore,

data about pump performance (16), pump thrombosis (17,18), clinical outcome (15,19), as well as numerical investigations (20,21) can be found in the literature for comparison and evaluation. Hence, the HMII geometry was chosen for this work in order to (i) discuss critical flow features with respect to blood damage and thrombus formation and (ii) supply the community with experimental flow data for comparison with CFD. CFD is one of the main methods used in the development and optimization processes of rotary blood pumps in terms of flow fields and inferred sources of blood damage.

In VADs, the largest viscous mechanical blood loading and therefore sources of damage occur in the proximity of solid surfaces. Therefore, shear stress measurements at the pump housing and the rotor blade tips were performed using the wall-PIV method (22). With the same method, zones of reversed or recirculating flow on the pump housing were detected. Recirculating zones on surfaces besides the housing were visualized by a paint erosion method. Then, an unsteady Reynolds-averaged Navier–Stokes simulation-computational fluid dynamics (URANS-CFD) simulation of the HMII was performed. It allows the application of state of the art blood damage models such as Lagrangian (23) or Eulerian (24) approaches. Especially, the calculation of hemolysis or platelet lysis indices based on those models is of great interest to the evaluation of pump hemocompatibility and hemodynamic performance.

The scope of this work is therefore to:

1. Identify regions of critical low/high shear stresses and recirculation zones;
2. Investigate the dependence of WSS on states of operation;
3. Compare experimental results with CFD.

MATERIALS AND METHODS

Geometry

The HMII is an axial pump that consists of a flow straightener, an impeller, and a diffuser (see Fig. 1). The entire pump geometric dimensions were taken manually with a sliding gage (0.005 mm readability) from an explanted device which had been implanted for 1.5 months. In order to obtain the blade curvature, the blade tips were dyed with ink and rolled over a sheet of paper. The imprints on the sheet were then digitized. The cylindrical housing inner diameter is 12 mm and the clearance gap between the impeller blades and the housing is measured at 100 μm .

Experimental setup

The pump parts were enlarged three times for easier optical accessibility of the wall-PIV measurements and manufactured by a 3D printer (Ultimaker 1, Ultimaker B.V., Geldermalsen, The Netherlands) with a maximum layer resolution of 20 μm from polylactide. For a smooth surface finish, fine sand paper (P1200) was used for polishing the surface and an automotive coating layer (Ral-lye-Klarlack (aerosol can), Dupli-Color, MOTIP DUPLI GmbH, Hassmersheim, Germany) was sprayed on the surface. The impeller was mounted on a shaft with 6 mm diameter which was guided through the diffuser hub and connected to a DC motor via a claw clutch. A tube made of acrylic glass with an inner diameter of 36 mm was used as transparent pump housing. The tip gap size was ~ 0.45 mm. The circular inlet of the acrylic tube was equipped with an inlet lip to ensure an inlet flow without flow separation. The pump was then placed in wall proximity in vertical position inside a transparent acrylic fluid tank. In order to create an optimal optical access, the space between the tube and the tank wall was filled with transparent silicone (Elastosil RT 601, Wacker-Chemie GmbH, München, Germany). The difference in height between the reservoir level and the pump outlet defined the pressure head. The flow rate was measured with a vane anemometer.

All operational parameters for the enlarged model were calculated with respect to Reynolds and Euler similarity laws. The Reynolds number is defined as $Re = UL_c/\nu$ and the Euler number as $Eu = \Delta p/(U^2\rho)$ with U , characteristic velocity; L_c , characteristic length; ν , viscosity; Δp , pressure head; and ρ , fluid density. When the pump is scaled up three times, the rotational speed, the pressure head, and shear stresses are 1/9 of the 1:1 sized model. The volume flow for the 3:1 model is increased threefold. The specific speed which is a dimensionless quantity used in turbomachinery to characterize pumps (25) is then equal for the original pump and model as well.

All pressures and flow rates in this paper will be, if stated in 3:1 scale, followed in brackets by the corresponding values of the 1:1 scale.

The fluid is a mixture of 62.5 vol. % osmotic water and 37.5 vol. % glycerol mimicking the properties of blood. It results in a kinematic viscosity of $3.65 \times 10^{-6} \text{ m}^2/\text{s}^{-1}$ at 22°C ambient temperature which approximates the viscosity of blood for typical flows in most arteries (26).

Wall-PIV method

The wall-PIV method is an optical technique based on particle tracking to measure velocity fields up to 300 μm above plane and curved surfaces. The wall-PIV method was developed at the Charité Biofluid Mechanics Laboratory. In wall-PIV, the fluid medium is dyed with Patent Blue V (Schumann und Sohn, Karlsruhe, Germany), a molecular dye, and a nearly monochromatic light source at the absorption peak is used to illuminate the particles through the transparent casing. The depth information of the tracked particles is then obtained from the brightness of the light reflected by the spherical tracer particles. Bright particles are located close to the transparent surface whereas particles away from the casing wall appear darker due to the absorption of the light based on Beer–Lambert’s law. By knowing the tangential velocity components at the measured wall normal height and the assumption of no-slip at the wall, WSS can be estimated. A more detailed description including a validation of this measurement technique can be found in the work of Berthe et al. (22), Kertzscher et al. (27), and Affeld et al. (28).

Silver-coated hollow glass spheres (Conduct-o-fil AGSL-150-30-TRD, Potters Industries LLC, Carlstadt, NJ, USA) with 75 μm diameter were used as tracer particles in this work. The light sources were two red light-emitting diode arrays and diffusive screens for homogeneous lighting. A MotionPro Y4 high-speed camera (Integrated Design Tools, Inc., Tallahassee, FL, USA)

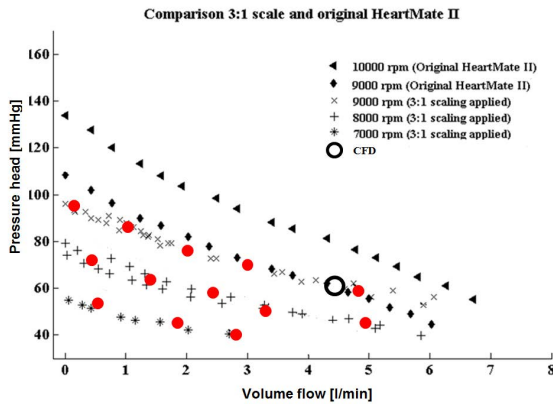


FIG. 2. Pump performance curves of the HeartMate II pump. Comparison between measured data of the 3:1 and the original-scale models (Original HeartMate II). The black circle represents the condition under which the CFD simulation was performed. The light gray dots represent the states of operation at which wall-PIV data were taken.

with 1024×1024 pixels resolution at a frame rate of 5000 frames/s was used for the high-speed particle tracking. The image processing and data analysis are performed with MATLAB (The MathWorks, Inc., Natick, MA, USA).

WSS from wall-PIV data can be calculated when the particle-wall distances are within the linear viscous sublayer and partially in the buffer layer (dimensionless wall distance $y^+ < 5 \dots 10$) of the turbulent boundary layer (29) and a no-slip condition at the wall is assumed. The thickness of this viscous sublayer can be estimated based on the expected WSS occurring in the flow field. These are between 5 and 15 Pa and result in linear sublayer thicknesses of approximately 500 and 300 μm (29). Because most detected particles are detected at wall distances $< 200 \mu\text{m}$, the linear assumption holds indeed valid. However, this assumption is not valid in the impeller tip gap which has a width of $\sim 450 \mu\text{m}$. The tip gap flow is dominated by viscous forces and external pressure gradients. Here, a parabolic velocity profile is derived from the Navier-Stokes equations. This is considered to be a first-order approximation when calculating the WSS from wall-PIV data for the tip gap.

WSS data are presented based on the averaging over five rotations on a virtually unwrapped inner surface of the pump casing. The virtual unwrapping is generated during data postprocessing by shifting the field of view (marked as red shaded area in the inset of Fig. 4) by the same distance as the rotor moves in between two picture frames. Then, spatial averaging was performed for smoothing the data by using square bins of $2 \times 2 \text{ mm}^2$ with an overlap of

1 mm in each direction. A total of 1200 images were taken for each state of operation.

Measurements were performed at 13 states of operation for $777 (7000) < \omega < 1000 (9000)$ rpm with impeller Reynolds numbers between 15800 and 20400 ($Re_{\text{imp}} = 2r^2\omega/\nu$, with r , pump radius; and ω , rotational speed). A summary of the data points is depicted in Fig. 2 as gray dots.

Pump performance curves

Pump performance curves of the 3:1 model were measured by using a vane anemometer. Based on the anemometer impeller blade slope and the rotational speed, the flow rate can be calculated. The same fluid mixture as described in the experimental setup section was used.

Pump performance curves of the 1:1 model were measured in the same setup for an explanted HMII pump as described by Thamsen et al. (20).

Near-wall flow visualization

The near-wall flow on surfaces inside the pump housing can be assessed experimentally with the paint erosion and surface oil flow methods, respectively (14,30,31). A high-viscous, water-insoluble paint consisting of three parts of white oil paint and one part of turpentine is applied with a fine paint brush to all pump components. During pump operation, the paint is partially washed away due to the local flow in wall proximity. As it was tried to cover the experimental model surface with an almost equally thick visualization layer, the thickness of the remaining surface paint is considered to correspond to the average WSS acting on the surface. The streaks visible after each experiment show the direction of mean near-wall flow relative to the surface.

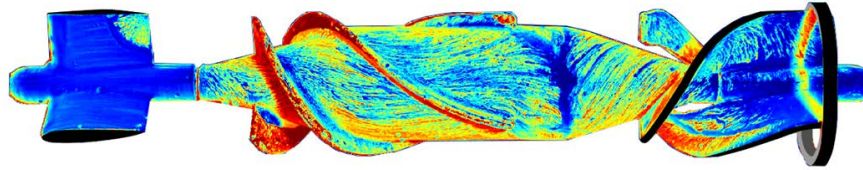
Each run was recorded for 6 min with a high-speed camera which was triggered at a specific rotor angle. The presented flow visualization image was then chosen from the recorded images based on the best visibility of all flow structures before most paint was washed away. Repeatability and thus independence of variations in the applied paint mixture thickness was shown by applying the flow visualization fluid mixture five times without seeing any meaningful differences in the resulting surface flow patterns.

CFD

A hexahedral mesh was created using ANSYS ICEM (Ansys Inc., Canonsburg, PA, USA) for one third of the rotationally symmetric pump model, resulting in 10^6 nodes. Boundary layers were resolved by at least 10 nodes with a high near-wall resolution ($y^+ < 1$). This allows the use of a low Reynolds

Volume flow 13.5 (4.5) l/min, $\Delta p = 6.6$ (59) mmHg

(a) Experiment: Near wall flow visualization, pseudo-colored



(b) CFD: Surface line integral convolution and wall shear stresses

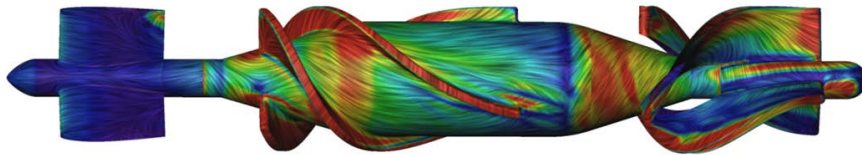


FIG. 3. Comparison of near-wall flow: (a) paint erosion method, (b) CFD-derived surface LIC. Pump state is at 13.5 (4.5) L/min and $\Delta p = 6.6$ (59) mm Hg. Numbers in brackets correspond to the values in original scale. WSS in the CFD image (b) range from 2 (18) (blue) to 13 (117) Pa (red). The visualization image (a) depicts regions with limited removal of surface flow visualization paint as blue regions toward regions of maximum paint erosion as red regions.

formulation of the turbulence model, namely the $k-\omega$ shear stress transport model (32). Our mesh for the upscaled geometry is based on the work of Thamsen et al. (20) and grid independence of the flow field solutions could be shown. Please refer to this article regarding grid independence and further details.

Blood was modeled as a Newtonian fluid with a density of 1050 kg/m^3 and a dynamic viscosity of 3.5 mPas . The boundary condition at the inlet was a mass flow inlet with a flow rate of 13.5 (4.5) L/min and fully developed turbulence. At the outlet an opening was defined with zero gradients.

The calculation was conducted using ANSYS CFX (Ansys Inc., Canonsburg, PA, USA). At first, a stable stationary solution was achieved using the frozen rotor approach. In the subsequent transient simulations the sliding mesh approach allows the rotation of the rotor domain. The angular position of the rotor is updated in 2° increments and computation continues until the variation in pump pressure head has become periodic and smooth. In each time step the residuals were kept below 10^{-5} . After the quasi-steady-state of the simulation has been reached, transient-averaged values of pressure and shear stresses are computed across three rotations of the rotor for further evaluation.

RESULTS

Pump performance curves

Pump performance curves for the explanted HMII and the 3:1 enlarged model are shown in Fig. 2. In

order to allow direct comparison between both scales and in order to show similarity between the 1:1 and 3:1 model, the 3:1 enlarged model data have been scaled according to the aforementioned similarity laws.

At 9000 rpm the performance curve of the 3:1 model shows a flatter trend compared to the original size explanted HMII, but is nonetheless in good agreement between 1 and 5.5 L/min volume flow.

Near-wall flow visualization results

The results of the near-wall flow visualizations on the rotor blades and hub are shown in Fig. 3. Figure 3a represents the experimental data based on gray scales that were converted into a “jet” color map as predefined in MATLAB (33). In our case, originally black pixels are represented by red colors and originally white pixels are represented by blue colors, whereas gray scales in between are colored as shown in the color bar in Fig. 3. Therefore, blue colors represent little washout (low WSS) and red colors represent high washout (high WSS), respectively. Increased levels of paint removal and increased WSS can be found, respectively, on the impeller blade surfaces as well as on the blade tip surface. Some increased WSS are also visible on the leading edges of the diffuser. The rotor is evenly covered with surface paint streaks which are initially directed tangential to the rotor curvature and then further downstream in axial direction. The surface paint thickens and indicates

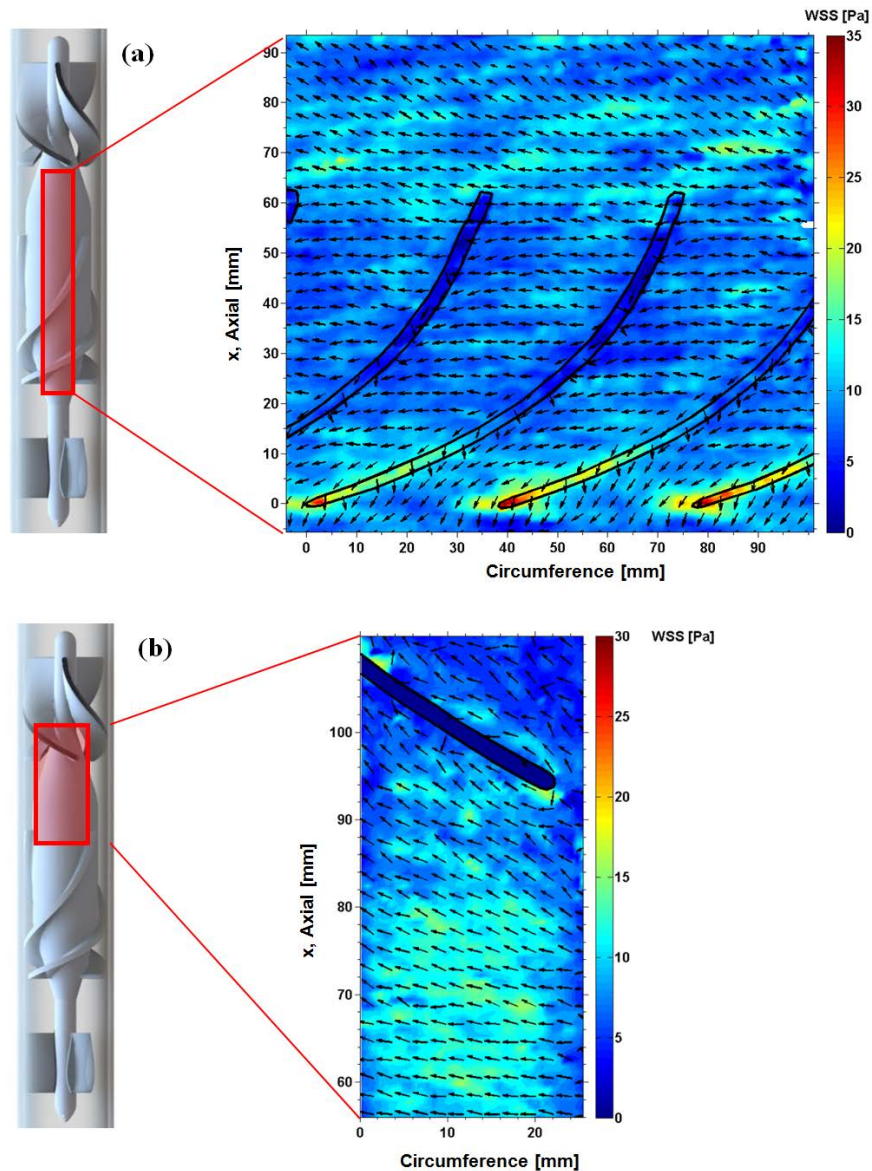


FIG. 4. WSS field at 1000 (9000) rpm and $\Delta p = 6.6$ (59) mm Hg on the rotor shroud (a) between $-5 < x < 90$ mm in the rotating frame and (b) between $60 < x < 110$ mm in the resting frame. The contours of the blade tips in (a) are projected across the tip gap onto the field of view. Numbers in brackets correspond to the values in original scale. The red shaded rectangular areas in the pump schematics correspond to the areas that were used for the generation of the WSS contours in postprocessing.

lower WSS (blue color) downstream of the rotor blades toward the onset of the diffuser part of the rotor. The diffuser shows surface paint streaks that are aligned tangentially to the stator blades. The timely progression of the paint washout (not shown here) reveals that the streaks on the diffuser part of the rotor are generated by a flow pointing in opposite direction of the main flow. On the diffuser blades, a separation line is seen in the middle of the blade with a thick layer of paint close to the

hub indicating higher WSS closer to the outer housing wall.

Figure 3b is a surface line integral convolution (LIC) image of the WSS and represents the direction of the flow in wall proximity based on the CFD simulation. The LIC image is generated by convolving the WSS field with white noise in order to obtain randomly seeded stream lines. For details, see Cabral and Leedom (34). The LIC image was colored with blue representing low and red

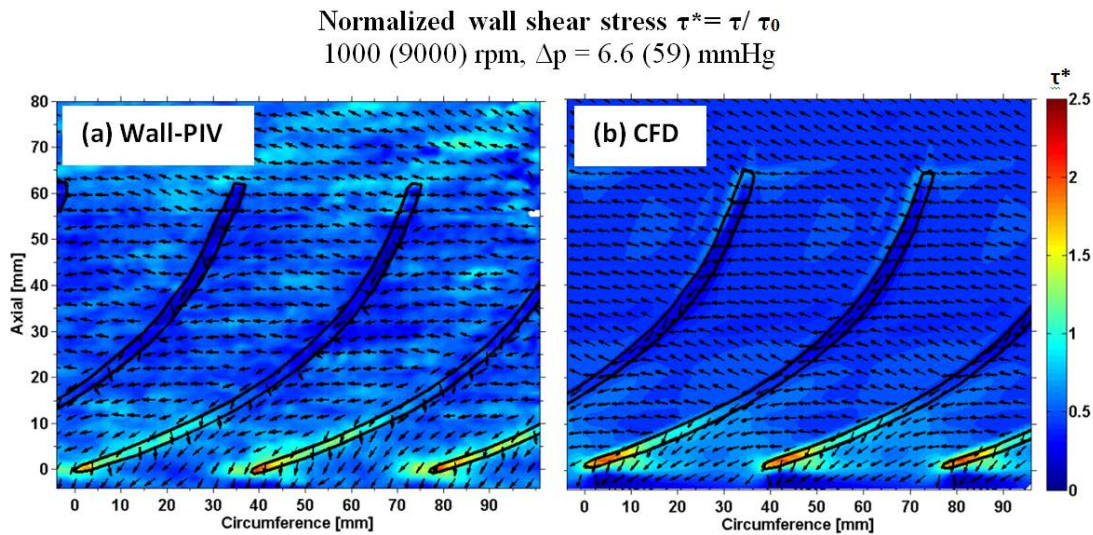


FIG. 5. Comparison of normalized WSS distributions between (a) wall-PIV and (b) CFD-based measurements for the inner pump casing. Normalization factor $\tau_0 = \mu u_r/h$.

representing high magnitudes of WSS in the same fashion as the experimentally generated pseudo-color map. Experimental and numerical results agree well in terms of direction of WSS and locations of maximum and minimum surface loads as described above for the experimentally observed flow structures.

Wall-PIV: WSS data

The analyzed regions which are zones close to the housing wall are shown in the graphics on the left-hand side in Fig. 4.

Data are shown in Fig. 4 for 1000 (9000) rpm and 6.6 (59) mm Hg as vector plots depicting the direction of the near-wall velocities and hence WSS. Color contours represent the magnitude of the WSS.

For the field of view in Fig. 4a, the WSS contours show a maximum of approximately 38 (342) Pa under and around the leading edge surface of the rotating blades. Slightly increased WSS are still present when moving further downstream along the tip gap. Those WSS become minimal for distances larger than 15 mm downstream of the rotor blade leading edges and are smaller than the lowest WSS on the surrounding inner pump housing surface. In summary, the maximum WSS occurred at the upstream third of the rotor blades. Because the data are presented in a nonrotating frame, most of the WSS point into the circumferential direction. Nonetheless, when approaching the side edges and

tips of the rotor blades, respectively, the flow is accelerated normal to the blade curvature.

Data at other states of operation present a very comparable distribution of WSS and are thus not shown. For comparison of the WSS between each state of operation, the average of 0.5% of the maximum measured WSS in the field of view at each operating point is calculated. A positive linear regression with $R^2 = 0.79$ between the maximum WSS and the pressure head can be found. This linear relationship was independent of volume flow and rotational speed (for 4.4 [40] $< \Delta p < 10.4$ [93.6] mm Hg and 777 [7000] $< \omega < 1000$ [9000] min^{-1}).

The second field of view (Fig. 4b) reaches from approximately 60 to 110 mm in axial direction. The time averaged flow field is presented in a stationary frame. Because the rotor is moving through the lower part of the image, it is being spatially averaged and does not reproduce the same flow field as shown in Fig. 4a. A maximum WSS of approximately 20 (180) Pa can be found at the leading edge of the stator.

Based on the assumed parabolic flow profiles in the tip gap flow, WSS distributions on the tip of the rotor blades were calculated. The maximum WSS were ~ 65 (585) Pa near the leading edge tip of the impeller blade. The WSS were reduced further downstream along the tip gap to values between 30 (270) and 40 (360) Pa.

When comparing the WSS fields with CFD, a very good qualitative agreement is achieved whereas the absolute maximum values of the

TABLE 1. Summary of maximum WSS at 1000 (9000) rpm and 6.6 (59) mm Hg, based on $h = 0.3$ mm. Numbers in brackets correspond to the values in original scale

Max. WSS: 1000 (9000) rpm, 6.6 (59) mm Hg	3:1		1:1	
	Wall-PIV (Pa)	CFD (Pa)	Wall-PIV (Pa)	CFD (Pa)
Inner pump housing	62	68	560	610
Rotor tip surface	90	120	810	1080

numerically obtained WSS are approximately 1.5 times larger than the measured ones. For better comparability between measurements and CFD, the WSS were normalized by the shear stress caused by linear shearing between the rotor blade tips and the casing wall $\tau_0 = \mu \frac{u_t}{h}$ with μ , dynamic viscosity; u_t , tangential blade tip velocity; and h , gap height. The resulting normalized WSS for the experimental data and the CFD simulations are depicted in Fig. 5. The difference between CFD and the experimental data of the maximum normalized WSS magnitudes is minimal on the pump housing, although the CFD-based maximum WSS extend a little bit further downstream in the rotor tip gap. A comparison of the maximum WSS between wall-PIV and CFD on the inner housing surface and the rotor tip surface for this operating point is listed in Table 1.

Differences can also be seen when comparing the direction of WSS. The numerical WSS at the center part of the tip gap flow point rather in blade tangential direction and further downstream into the circumferential direction. The direction of the WSS of the center part of the rotor blade tip flow based on experimental data, however, points rather normal to the local blade curvature.

The tip gap leakage flow was calculated by integrating the velocity components from the parabolic velocity profile normal to the blade contour obtained from the wall-PIV data. The leakage volume flow was for all measured states of operation between 3 and 4 L/min while at the same time the overall volume flow varied between almost 0 to 14 L/min. The data are presented in Table 2.

DISCUSSION

Similarity and scaling

Similarity between the 1:1 and the 3:1 HMII was shown by comparing the corresponding throttle curves in Fig. 2. The data of the 3:1 HMII model were scaled to its corresponding operating points at original size. It shows good agreement with the measured 1:1 data at 9000 rpm for volume flows between 1 and 5.5 L/min. At lower volume flows

and correspondingly larger pressure head, the pressure head is about 10–15% lower than for the corresponding original sized model. A possible reason is the difference in the rotor blade tip gap size, because the 3:1 HMII model has an actual tip gap height of approximately 0.45 mm instead of 0.3 mm and thus larger losses at large pressure heads than the original model. Nonetheless, the larger tip gap size does not seem to affect the overall pump performance significantly based on original-scale volume flows between 1 and 5.5 L/min.

Comparison of CFD with experiments: WSS

The measured WSS are close to the values which have been computed with the help of CFD and also to those which have been found in published data of HMII-like axial blood pumps based on CFD (20,21). However, it should be mentioned that the experimental and numerical data had been spatially averaged over a 4 mm² area. Especially in the region of maximum WSS (close to edges), local peaks at single cells in the CFD-based WSS were smoothed.

Regions of critical flow: flow separation and recirculation

The wall-PIV data do not show any flow separation or critically low WSS (<1 Pa for thrombus formation (35)) downstream of the impeller leading edges (axial locations >0 mm). However, upstream of the impeller leading edges (axial locations <0 mm), backflow with very low WSS was identified. Main causes for the backflow are the tip gap leakage flow which points into the opposite direction of the main flow due to the pressure gradient across the impeller blades and due to the positive pressure gradient between pump inlet and outlet.

There is some significant backflow at the diffuser on the rotor. A point with nearly stagnating flow of ~1 (9) Pa WSS (from CFD) can be seen in the flow visualization (Fig. 3a,b) at the onset of the diffuser. The diffuser generates an increase of cross-sectional area and causes an adverse pressure gradient driving the flow against the main flow along the rotor surface through the gap of the diffuser blades. At the onset of the cross-sectional widening of the

TABLE 2. Tip gap leakage flow in dependence of state of operation. The bold entries correspond to the values at the discussed state of operation (1000 [9000] rpm, 6.6 [59] mm Hg). The min and max values correspond to the minimum and maximum values of the respective values at one rotational speed. All values are given for the 3:1 up scaled model size

RPM	$V_t = \text{Tip}$ gap flow (L/min)		$V_0 = \text{Pump}$ volume flow (L/ min)		Δp (cmH ₂ O)		V_t/V_0	
	min	max	min	max	min	max	min	max
1000	3.5	3.8	0.45	13.8	9	14.2	0.27	7.8
888	3.3	3.5	1.5	14.1	7	11	0.23	2.3
777	3	3.2	0.15	8.1	6	8.2	0.37	21.3

rotor, boundary layer flows of main flow and diffuser backflow impinge and cause the observed region of low WSS.

Both major flow separation zones are inherent to the pump flow and will most likely be present independent of rotational speed and pressure head.

A region of low WSS (~ 1 [9] Pa) was identified in the flow visualization images and the simulations (Fig. 3) on the flow straightener, including the downstream end of the flow straightener shaft, right in front of the upstream bearing of the rotor. Especially, this region is critical to blood damage as friction heat is generated at the bearing. With the observed low WSS and thus prolonged residence time of the blood, this region is prone to local thrombus formation. The in-vivo formation of thrombi downstream of the described location were found, e.g., by Mokadam et al. (36) and Chiu et al. (37).

Dependencies on state of operation

The wall-PIV data show that the averaged maximum WSS depend mainly on the pressure head of the pump regardless of the volume flow or rotational speed. It is assumed that this is a direct effect of the increased mechanical blade loading and hence an increase of pressure gradient which is responsible for a larger velocity gradient across the blade tips, especially at the rotor gap. The same behavior for a HMII-like pump for the scalar shear stresses based on RANS-CFD was found by Fraser et al. (21).

The tip gap leakage flow is a measure for the hydrodynamic efficiency of the pump and has a major impact on hemolysis and thus blood damage (38). The resulting data are summarized in Table 2. Comparable relative tip leakage flows at or close to the corresponding pump design point were found

by other investigators for radial and axial blood pumps (5,14,39). The tip gap leakage flow measured presented in this work shows only a weak dependence on the different states of operation. This leads to the conclusion that the tip gap leakage flow can exceed the total pump volume flow multiple times at low overall volume flows (Table 2). This is critical with respect to blood damage because blood experiences the maximum mechanical loading close to surfaces in the tip gap. As shown in Table 1 for the investigated point of operation, the WSS exceed for most of the surfaces at the tip gap the critical values for hemolysis (450 Pa [1 ms]–560 [0.1 ms] Pa) (40,41), platelet activation (255 Pa [7 ms], 700 Pa [1 ms]–1400 [0.1 ms] Pa) (42,43), and vWF cleavage (>9 Pa) (44).

It is therefore rather unfavorable to run axial and centrifugal blood pumps at low volume flows, especially with fast rotational speeds or large pressure heads.

Study limitations

The pump geometry was manually taken from an explanted device and is thus underlying some uncertainty. Upscaling the pump results in unavoidable wall roughness differences between the original and model which can influence boundary layer growth and separations. Nevertheless, an attempt was made to generate very smooth surfaces and a good agreement between experiments and CFD was seen. Furthermore, the pump drive with an external motor and shaft in contrast to the original BLDC motor was realized. However, this mismatch did not influence the flow field inside the pump.

Additionally, the inflow of an implanted pump passes a 90° bend in the inflow cannula. Some flow separation or secondary flow might occur here depending on the volume flow, resulting in a non-homogeneous inflow field. In addition, flow in a VAD is naturally not constant. Nonetheless, this is not a limiter in terms of comparability between CFD and experiment.

CONCLUSIONS

Within the scope of this work a comparison between computational fluid dynamics and the corresponding experimental data for the relevant flow features inside a HeartMate II pump with respect to blood damage and thrombus formation was performed. Additionally, the dependence of relevant parameters on the state of operation was to be investigated. Zones of flow recirculation and separation are critical locations for thrombus formation and were found on the diffuser and on the housing

upstream of the impeller blade leading edges. It was shown that the peak wall shear stresses and thus critical locations of maximum mechanical blood loading were in the rotor tip gap close to the rotor leading edge and exceed in any case the hemolysis threshold. The maximum measured WSS at 1000 (9000) rpm and 6.6 (59) mm Hg were found to be 90 (810) Pa on the impeller blade surface and 62 (560) Pa on the housing wall. These values correspond to approximately 3 and 2.5 times the linear shearing between impeller tip and pump housing.

Besides that, the CFD-based k - ω RANS modeling of the HMII was shown to predict reliably the experimental data, and wall-PIV has been shown to be a good experimental technique for the measurement of WSS in enlarged axial blood pump models.

Acknowledgment: This work was sponsored by a grant from the Investitionsbank Berlin (IBB) (10153412) supported by the “Europäischer Fond für regionale Entwicklung” (EFRE).

REFERENCES

- Lima B, Mack M, Gonzalez-Stawinski G. Ventricular assist devices: the future is now. *Trends Cardiovasc Med* 2014;25:360–9.
- Giersiepen M, Wurzinger L, Opitz R, Reul H. Estimation of shear stress-related blood damage in heart valve prostheses—in vitro comparison of 25 aortic valves. *Artif Organs* 1990;13:300–6.
- Eckman P, John R. Bleeding and thrombosis in patients with continuous-flow ventricular assist devices. *Circulation* 2012;125:3038–47.
- Treichler J, Rosenow S, Damm G, et al. A fluid dynamic analysis of a rotary blood pump for design improvement. *Artif Organs* 1993;17:797–808.
- Chua L, Ong K, Yu C, Zhou T. Leakage flow rate and wall shear stress distributions in a biocentrifugal ventricular assist device. *ASAIO J* 2004;50:531–6.
- Mizunuma H, Nakajima R. Experimental study on shear stress distributions in a centrifugal blood pump. *Artif Organs* 2007;31:550–9.
- Pinotti M, Paone N. Estimating mechanical blood trauma in a centrifugal blood pump: laser Doppler anemometer measurements of the mean velocity fields. *Artif Organs* 1996;20:546–52.
- Day S, McDaniel J. PIV measurements of flow in a centrifugal blood pump: steady flow. *Trans ASME* 2005;127:244–53.
- Su B, Chua L, Wang X. Validation of an axial flow blood pump: computational fluid dynamic results using particle image velocimetry. *Artif Organs* 2012;36:359–67.
- Yang X, Gui X, Huang H, Shen Y, Yu Z, Zhang Y. Particle image velocimetry experimental and computational investigation of a blood pump. *J Therm Sci* 2012;21:262–68.
- Wu Z, Gottlieb R, Burgreen G, et al. Investigation of fluid dynamics within a miniature mixed flow blood pump. *Exp Fluids* 2001;31:615–29.
- Apel J, Neudel F, Reul H. Computational fluid dynamics and experimental validation of a microaxial blood pump. *ASAIO J* 2001;47:552–58.
- Kerrigan J, Yamazaki K, Meyer R, et al. High resolution fluorescent particle-tracking flow visualization within an intraventricular axial flow left ventricular assist device. *Artif Organs* 1996;20:534–39.
- Sieß T. *Systemanalyse und Entwicklung Intravasaler Rotationspumpen zur Herzunterstützung*, Aachen, Germany: Shaker Verlag GmbH, 1999.
- Pagani F, Miller L, Russell S. Extended mechanical circulatory support with a continuous flow rotary left ventricular assist device. *J Am Coll Cardiol* 2009;54:312–21.
- Thoratec Corporation. Pleasanton, CA 94588. Available at: http://www.fda.gov/ohrms/dockets/ac/07/briefing/2007-4333b2-18-%209_2%20HM%20II%20Operating%20Manual.pdf. Accessed May 19, 2015.
- Starling R, Moazami N, Silvestry S, et al. Unexpected abrupt increase in left ventricular assist device thrombosis. *N Engl J Med* 2014;370:33–40.
- Uriel N, Han J, Morrison K, et al. Device thrombosis in HeartMate II continuous-flow left ventricular assist devices: a multifactorial phenomenon. *J Heart Lung Transplant* 2014;33:51–9.
- Slaughter MS, Rogers JG, Milano CA, et al. Advanced heart failure with continuous-flow left ventricular assist devices. *N Engl J Med* 2009;361:2241–51.
- Thamsen B, Blümel B, Paschereit C, Affeld K, Kertzsch U. Numerical analysis of blood damage potential of the HeartMate II and Heartware HVAD rotary blood pumps. *Artif Organs* 2015;39:651–9.
- Fraser K, Zhang T, Taskin M, Griffith B, Wu Z. A quantitative comparison of mechanical blood damage parameters in rotary ventricular assist devices: shear stress, exposure time and hemolysis index. *J Biomech Eng* 2012;134:081002.
- Berthe A, Kondermann D, Garbe C, Affeld K, Jähne B, Kertzsch U. The wall-PIV measurement technique for near wall flow fields in biofluid mechanics. In: Nitsche W, Dobriloff C, eds. *Imaging Measurement Methods for Flow Analysis*. Berlin, Heidelberg: Springer, 2009:11–20.
- Goubergrits L. Numerical modeling of blood damage: current status, challenges and future prospects. *Expert Rev Med Devices* 2006;3:527–31.
- Garon A, Farinas M. Fast three-dimensional numerical hemolysis approximation. *Artif Organs* 2004;28:1016–25.
- Gülich J. *Centrifugal Pumps*. Springer Science & Business Media, Springer: Heidelberg, 2007.
- Schmidt RF, Lang F, Heckmann M. *Physiologie des Menschen mit Pathophysiologie*, Tokyo: Springer, 2007.
- Kertzsch U, Berthe A, Goubergrits L, Affeld K. Particle image velocimetry of a flow at a vaulted wall. *Proc Inst Mech Eng H* 2008;222:465–73.
- Affeld K, Kertzsch U, Goubergrits L. Experimental assessment of wall shear flow in models. *Biorheology* 2002;39:485–9.
- Pope S. *Turbulent Flows*. Cambridge University Press: Cambridge, UK, 2000.
- Affeld K, Zartnack F, Monhaupt R, Bücherl E. New methods for the in vitro investigations of the flow patterns in artificial hearts. *Trans Am Soc Intern Organs* 1976;22:460–7.
- Merzkirch W. *Visualization of Surface Flow*, 2nd Edition. Orlando, FL: Academic Press, Inc., 1987:82–7.
- Menter F. Zonal two equation k -turbulence models for aerodynamic flows. *23rd Fluid Dynamics, Plasmadynamics, and Lasers Conference*. AIAA: Orlando, FL, 1993.
- The MathWorks. Available at: <http://de.mathworks.com/help/matlab/ref/colormap.html?searchHighlight=jet%20colormap>. Accessed December 18, 2015.
- Carbal B, Leedom L. Imaging vector fields using line integral convolution. *SIGGRAPH'93 Proceedings of the 20th Annual Conference on Computer Graphics and Interactive Techniques*. ACM: Anaheim, CA, 1993:263–70.
- Hochareon P, Manning K, Fontaine A, Tarbell J, Deutsch S. Correlation of in vivo clot deposition with the flow

- characteristics in the 50 cc Penn State artificial heart: a preliminary study. *ASAIO J* 2004;50:537–42.
36. Mokadam N, Andrus S, Ungerleider A. Thrombus formation in a HeartMate II. *Eur J Cardiothorac Surg* 2011;39:414.
 37. Chiu W, Slepian M, Bluestein D. Thrombus formation patterns in the HeartMate II VAD-clinical observations can be predicted by numerical simulations. *ASAIO J* 2014;60:237–40.
 38. Mitamura Y, Yoshida T, Yozu R, Kawada S, Tanaka T. Relationship between hemolysis and design of an axial pump. In: Akutsu T, Koyangi H, eds., *Heart Replacement*. Tokyo, Japan: Springer, 1996;229–31.
 39. Chua L, Su B, Tau M, Zhou T. Numerical simulation of an axial blood pump. *Artif Organs* 2007;31:560–70.
 40. Rooney J. Hemolysis near an ultrasonically pulsating gas bubble. *Science* 1970;169:869–71.
 41. Williams A, Hughes D, Nyborg W. Hemolysis near a transversely oscillating wire. *Science* 1970;169:871–3.
 42. Colantuoni G, Hellums J, Moake J, Alfrey C. The response of human platelets to shear stress at short exposure times. *Trans Am Soc Artif Intern Organs* 1977;23:626–31.
 43. Wurzinger L, Opitz R, Blasberg P, Schid-Schönbein H. Platelet and coagulation parameters following millisecond exposure to laminar shear stress. *Thromb Hemost* 1985;54:381–86.
 44. Vergauwe E, Uji-i H, Ceunynck KD, Vermant J, Vanhoorelbeke K, Hofkens J. Shear-stress-induced conformational changes of von Willebrand factor in a water-glycerol mixture observed with a single molecule microscopy. *J Phys Chem B* 2014;118:5660–9.

2.3 Paper III:

A two-stage rotary blood pump design with potentially lower blood trauma: a computational study

Final objective of this thesis was to develop and investigate a novel pump design with decreased shear stresses to reduce blood trauma. The idea was to use two pump stages instead of a single stage to distribute the required pressure build-up. By using two stages, lower rotational speeds and consequently reduced circumferential velocities are possible.

Based on the principles of turbomachinery, two diagonal rotor stages were designed with a diffuser at the end of the first stage and a volute casing behind the second stage. Both stages are combined into one rotating part which is pivoted by two mechanical cup-socket bearings. The CFD method was applied to analyze the flow characteristics inside the new pump and to compare them with the flow features of the HM II and HVAD which are state-of-the-art blood pumps that contain only a single-stage. Furthermore, a functional model of the pump was fabricated with the help of rapid prototyping and the characteristic curves were measured in the test stand described in chapter 1.6.4 to capture the operational behavior of the new pump.

The measured curves indicated adequate physiological pressure heads and volume flows which are similar to centrifugal pumps. The CFD results revealed a pressure head of 70 mmHg at a flow rate of 5 L/min and a rotational speed of 3200 rpm and smooth flow fields with well-distributed pressures. Circumferential velocities were reduced to 3.7 m/s as compared to 6.2 m/s in the HM II pump. Consequently, lower shear stresses were calculated. Compared to the HM II and the HVAD, volumetric portions of the pump exposed to shear stresses as high as and above 150 Pa could be reduced by at least 70 %. This might reduce blood trauma and subsequent adverse events in LVAD patients.

A two-stage rotary blood pump design with potentially lower blood trauma: a computational study

Bente Thamsen¹, Ricardo Mevert¹, Michael Lommel¹, Philip Preikschat¹, Julia Gaebler¹, Thomas Krabatsch², Ulrich Kertzscher¹, Ewald Hennig², Klaus Affeld¹

¹Biofluid Mechanics Laboratory, Charité Universitätsmedizin Berlin, Berlin - Germany

²Department of Cardiothoracic and Vascular Surgery, Deutsches Herzzentrum Berlin, Berlin - Germany

ABSTRACT

Aim: In current rotary blood pumps, complications related to blood trauma due to shear stresses are still frequently observed clinically. Reducing the rotor tip speed might decrease blood trauma. Therefore, the aim of this project was to design a two-stage rotary blood pump leading to lower shear stresses.

Methods: Using the principles of centrifugal pumps, two diagonal rotor stages were designed with an outer diameter of 22 mm. The first stage begins with a flow straightener and terminates with a diffusor, while a volute casing behind the second stage is utilized to guide fluid to the outlet. Both stages are combined into one rotating part which is pivoted by cup-socket ruby bearings. Details of the flow field were analyzed employing computational fluid dynamics (CFD). A functional model of the pump was fabricated and the pressure-flow dependency was experimentally assessed.

Results: Measured pressure-flow performance of the developed pump indicated its ability to generate adequate pressure heads and flows with characteristic curves similar to centrifugal pumps. According to the CFD results, a pressure of 70 mmHg was produced at a flow rate of 5 L/min and a rotational speed of 3200 rpm. Circumferential velocities could be reduced to 3.7 m/s as compared to 6.2 m/s in a clinically used axial rotary blood pump. Flow fields were smooth with well-distributed pressure fields and comparatively few recirculation or vortices. Substantially smaller volumes were exposed to high shear stresses >150 Pa.

Conclusions: Hence, blood trauma might be reduced with this design. Based on these encouraging results, future *in vitro* investigations to investigate actual blood damage are intended.

Keywords: Blood trauma, Computational fluid dynamics, Rotary blood pump, Two-stage pump

Introduction

After the first implantation of a rotary blood pump in 1998, the use of rotary blood pumps as left ventricular assist devices (LVAD) has become an established treatment for patients with end-stage heart failure, even for destination therapy (1). However, complications related to blood trauma are frequently observed. Blood components on transit through these rotary blood pumps are subjected to different levels of shear stress for certain time periods. Depending on the specific flow path, some particles experience non-physiological high shear stress at prolonged exposure times, which lead to damaging effects

on erythrocytes, platelets, von Willebrand factor (vWF) proteins, and leukocytes. Fraser et al describe the types of blood damage in more detail (2). Briefly, hemolysis as damage to the erythrocytes occurs at very high shear stresses (above 150 Pa) (3) and is a known complication of LVADs (4). The activation of platelets (above shear stresses of 50 Pa) (2, 5), might lead to pump thrombosis or thromboembolic events, which are serious adverse events in LVAD patients (6, 7). vWF degradation already occurs at low shear stress (3-10 Pa) (8-10) and causes acquired von Willebrand syndrome which affects bleeding complications (11, 12). However, a region of very low shear stress below 1 Pa and subsequent flow stasis is critical for thrombus formation (2). Furthermore, damaged leukocytes form micro-particles which might play a role in thrombogenesis (13). Up to 36% of the adverse events summarized in the seventh INTERMACS (Interagency Registry for Mechanically Assisted Circulatory Support) report may be related to these processes (bleeding, arterial non-cerebral thrombosis, venous thrombotic event, hemolysis, stroke during 2012-2014) (14).

Currently, the LVADs clinically implanted most frequently are the Heartmate II (HM II; Thoratec Corp, Pleasanton, CA) and the Heartware HVAD (Heartware International Inc., Framingham, MA), which are an axial and a radial rotary blood

Accepted: February 29, 2016

Published online:

Corresponding author:

Bente Thamsen
Charité – Universitätsmedizin Berlin
Biofluid Mechanics laboratory
Augustenburger Platz 1
13353 Berlin, Germany
bente.thamsen@charite.de

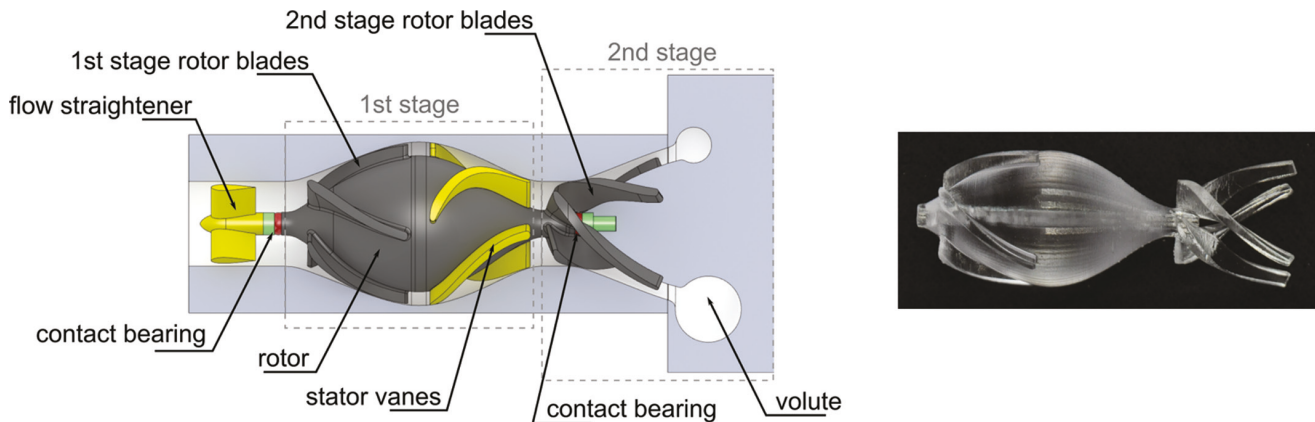


Fig. 1 - The application of more than one stage allows the reduction of rotational speed and thereby shear stresses. Left: the geometry of the developed two-stage rotary blood pump design. The dark gray colored rotor is the only moving part. Both stages use four diagonal blades. The first stage ends on a diffuser that guides the flow to the second stage. The second stage uses blades that are rotating on a stationary hub. The fluid is led to the outlet by a volute casing. Right: model of rotor that was manufactured via stereo-lithography and used for experimental acquisition of characteristic pump curves.

pump, respectively. These pumps consist of a single rotor that rotates relative to a static housing. High circumferential velocities of the blade tips in combination with a small gap between the rotor and the housing wall result in high velocity gradients and, thus, in high shear stresses. On one hand, a reduction of velocity gradients could be accomplished by increasing this gap; however, a larger gap needs to be compensated by a higher rotational speed to maintain the required operating point, namely pressure heads and flow rates in the physiological range. On the other hand, the velocity gradients could be decreased by reducing the circumferential velocity of the blade tips. Therefore, the aim of this work was to develop a rotary blood pump design with reduced circumferential velocities. This idea was realized by using two rotor stages in series instead of only one to allow for lower rotational speeds. A single rotating part was thereby maintained.

Material and methods

Pump design

Corresponding to the Euler equation of turbomachinery, the pressure head of a rotary pump can be calculated as follows.

$$\Delta p = \frac{\rho}{2} \cdot (v_3^2 - v_0^2 + u_3^2 - u_0^2 + w_0^2 - w_3^2) - J,$$

where v , u , and w denote the absolute, circumferential and relative velocities at the entry (index 0) and the exit (index 3) points of the rotor and J captures all losses (15). Thus, the pressure head is proportional to the squared circumferential velocity. By using two pump stages in series, the required pressure build-up is allocated to the two stages.

$$\Delta p = \Delta p_1 + \Delta p_2$$

so that the circumferential velocities of the blade tips can be reduced. In theory, two pump stages make a reduction of 30% feasible.

The pump developed here was composed of two pump stages with a single rotating part. Both stages employed four diagonal rotor blades which were designed using the principles of centrifugal pumps with an inlet outer diameter of 10 mm and an outlet outer diameter of 22 mm (15). Blade inlet angles were designed for a nominal flow rate of 5 L/min. To gently accelerate the fluid with an evenly distributed energy transfer, blades were designed with an axial length of 14 mm and a root-function-shaped hub was implemented. The diagonal design was chosen as a compromise between radial pumps, which are difficult to arrange as multiple stages, and axial pumps, which operate efficiently at higher speeds only. A flow straightener with three blades was placed at the inlet of the pump. The following first stage terminated with a diffuser utilizing four guide vanes fixed to the housing wall that guided the flow to the second stage. For the second stage, the blades rotated between a stationary hub and housing wall and were fixed to the rotating hub only in the region of the blade-inlet. All gaps were set to 100 μm . A volute casing following the second stage was utilized to guide fluid to the outlet. The design of the rotor and stator blades was optimized by altering blade angles and thickness iteratively and investigating the different designs using computational fluid dynamics (CFD) and measuring the characteristic curves of rapid-prototyped models. The best design with respect to the pressure head as well as the flow separation and stagnation zones is presented below. The bearing concept includes cup-socket bearings upstream of the first-stage rotor at the rear hub of the flow straightener and at the entry of the second stage. The shape of the rotor hub offers enough space to store magnets for a brushless DC motor drive. The final design shown in Figure 1 has a priming volume of 11 mL.

Measurements of characteristic curves

The hydraulic operational behavior of pumps is described by characteristic curves which capture the pressure head depending on the flow rate at different rotational speeds.

The characteristic curves were measured experimentally by obtaining the flow rate with an in-line magnetic-inductive flow probe (ifm electronic gmbh, Essen, Germany) and capturing the pressures at small distances from the inlet and outlet via two piezoresistive pressure transmitters (First Sensor AG, Berlin, Germany). A model fluid with a viscosity of 3.5 mPas, which corresponds to a hematocrit of 36% (16), was realized with a distilled water-glycerol mixture. The two-stage pump model was manufactured by stereolithography and driven by a shaft connected to a DC motor (dunkermotoren, Bonndorf/ Schwarzwald, Germany).

Computational fluid dynamics

Mesh set-up

Studies of the flow field were conducted with commercial CFD software STAR-CCM+ (CD-Adapco, Melville, New York), which uses a finite-volume approach. By utilizing its in-house advanced meshing capabilities, the computational domain was discretized using polyhedrons in the main flow section with a 0.22 mm base size and prismatic elements forming 10 inflation layers at the walls for a better resolution of high wall gradients.

To meet the challenging requirements of blade-fluid interaction, the grid in proximity to the blades was further refined. In contrast, the number of elements in the outlet domain was reduced, since high gradients were not likely to be seen in that region, and with intent to lower the computational effort. The entire domain consisted of about 4.3 M cells including extended inlet and outlet sections for more reliable numerical results. Mesh quality criteria were kept within the range advised by STAR-CCM+ guidelines (17). With regard to physical quality criteria, it was crucial to obtain values below 1 for the dimensionless wall distance y^+ in order to calculate the boundary layers instead of using wall models (17). The highest y^+ value in the entire field was 3.1 and 99.5% of the values ranged between 0 and 1. Proper resolution within the 100 μm gap between blades and housing was realized by providing at least 10 layers of cells. A preliminary mesh independence study was conducted, investigating change in pressure and wall shear stress with respect to the alteration of total cell numbers. Hence, the mesh contained the least number of cells, whereas an increase in cells would not result in different values.

Physical set-up

Several physical constraints are defined to translate the real conditions into a working numerical scheme. A mass flow inlet with a plug flow profile defines the flow rate for the specific operating point. Human blood is considered a shear thinning

fluid up to shear rates of 100 s^{-1} , beyond which its viscosity becomes independent of stress (18), which gives us a reason to model it as a Newtonian fluid with a viscosity of 3.5 mPas and density of 1050 kgm^{-3} . Average pressure at the outflow is set to 0 Pa. All remaining boundaries are slip-free walls.

The pump primes at a frequency of 3200 rpm. To model this behavior an actual motion of the rotor subdomains is applied, i.e., a sliding mesh approach with a frequency of one degree of rotation per time step. A frozen rotor simulation is used as an initial solution. If all residuals for continuity and momentum fall below 10^{-5} the next time step will be calculated. Turbulence is modeled using the $k-\omega$ -SST-model given by Menter (19).

Comparison to the HeartMate II® and the HVAD®

Significantly reduced stress to the blood cells is the main goal of this project. Accordingly, shear stresses need to be compared with clinically established rotary blood pumps. At an operating point of 5 L/min flow rate and approximately 70 mmHg pressure head the Thoratec HeartMate II LVAD and the HeartWare HVAD were compared to the two-stage pump under equal conditions, resulting in 9800 rpm (HM II) and 2600 rpm (HVAD) rotational speeds. These values were chosen based on measured characteristic curves with original HVAD and HM II pumps. The pump geometries were derived from explanted pumps as in Thamsen et al (20). The remaining physical and mesh parameters are akin to the ones described above.

The flow fields were compared with respect to different blood damage types and, respectively, different scalar shear stress levels below which no trauma was assumed, following previously suggested thresholds (2): For vWF degradation, a threshold of 9 Pa was used. For platelet activation the threshold was set to 50 Pa. Hemolysis was incorporated with a threshold of 150 Pa. Volume fractions exposed to viscous shear stresses above these thresholds were calculated for the pumps. This method was proposed by Fraser et al (2) and already employed by our group to compare the HM II and HVAD numerically at an operating point of 5 L/min and 80 mmHg (20). Geometrical and functional parameters for the two-stage pump design as well as for the two established rotary blood pumps are summarized in Table I.

Results

Characteristic curves

The experimentally obtained characteristic curves are presented in Figure 2. The two-stage pump achieves typical operating points for ventricular assist devices, thus it yields

TABLE I - Geometrical and functional parameters of the developed two-stage pump, the HM II and the HVAD

	Outer rotor diameter [mm]	Priming volume [mL]	Narrowest gap [μm]	Rot. speed at ~70 mmHg and 5 L/min [rpm]	Circumferential velocity [m/s]	Number of computational cells [M.]	Minimum number of cells in gap
Two-stage pump	22	10.7	100	3200	3.7	4.3	10
HVAD	34	11.2	50	2600	4.6	3.3	14
HM II	12	7.7	100	9800	6.2	4.4	10

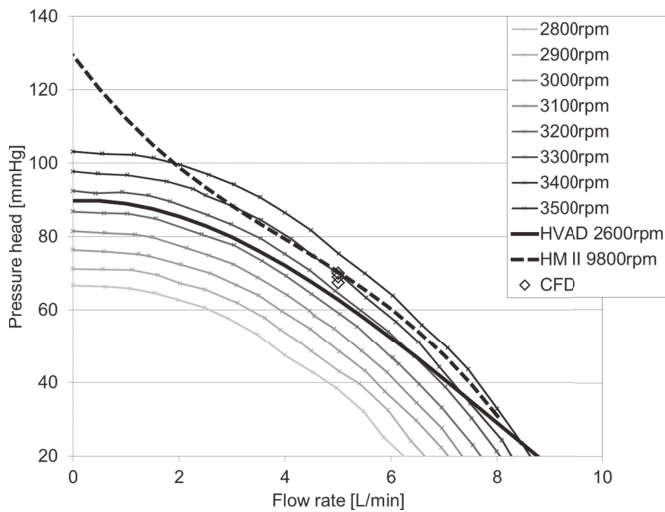


Fig. 2 - Experimentally assessed characteristic curves of the two-stage pump in comparison to curves of the HVAD and HM II pumps. The two-stage pump achieves similar operating points and shows a flat trend comparable to centrifugal pumps. The operating points for the numerically investigated condition are marked by \diamond , depicting pressure heads at 5 L/min and 2600 rpm for the HVAD (68 mmHg), 3200 rpm for the two-stage pump (69 mmHg), and 9800 rpm for the HM II (70 mmHg).

sufficient output to support a failing left ventricle. The curves show a flat trend predominantly at lower flow rates comparable to the behavior of centrifugal pumps.

CFD

The pressure head of the two-stage pump at 3200 rpm and 5 L/min flow rate was predicted by CFD to 69 mmHg and thus deviates from the measured value by 10 mmHg.

In Figure 3, the course of pressure generation in the pump is shown by area-averaged pressures at specific locations in the pump. A uniform gradual pressure build-up in both stationary and rotating parts is thereby indicated. The static pressure distributions on an axially aligned section plane, on the rotor and hub surface are shown on the right side in Figure 3. A general increase of static pressure from the pump inlet to the outlet was observed along with well-distributed pressure fields. The lowest pressure was seen on the blades' surfaces at the rotor inlet of the first stage. This is due to the high suction force in this region. Relatively higher pressures were noticed on the outer ends of the blades.

Streamlines of the main flow field, as displayed in Figure 4, indicate no irregular flow behavior. The fluid enters the rotor blade channels of both stages smoothly without areas of reversed flow and follows the shape of the blades. Correspondingly, the contact bearing sites, where a rise in temperature might appear, are washed out well. Helical flow develops in the volute casing.

The circumferential velocities at the investigated operating point were 3.7 m/s (3200 rpm) for the two-stage pump, 6.2 m/s (9800 rpm) for the HM II and 4.6 m/s (2600 rpm) for the HVAD. The streamlines as shown in Figure 4 reveal much lower velocities generally in the two-stage pump.

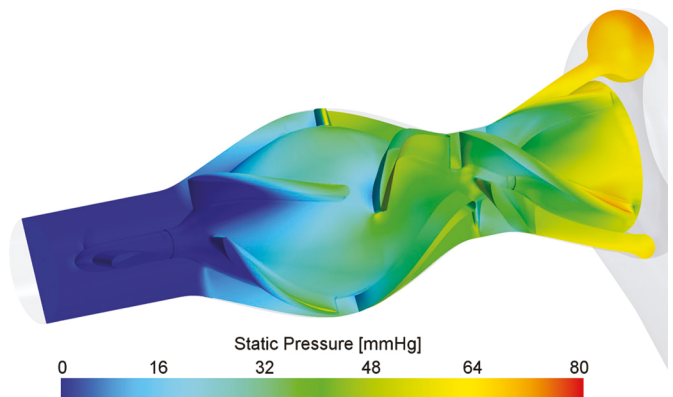
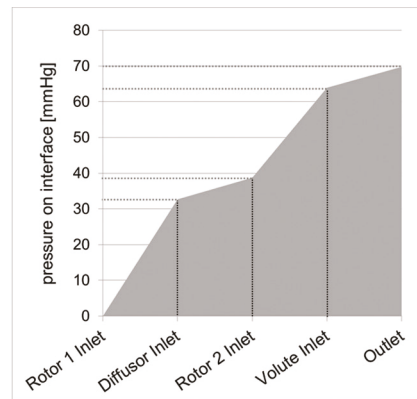


Fig. 3 - Upper: course of pressure increase in the two-stage pump. Area-averaged static pressures at different locations in the pump demonstrate that the pressure increases gradually. Lower: distribution of static pressure. The pressure is low at the inlet and reaches higher values at the outlet while it is well-distributed in the pump.

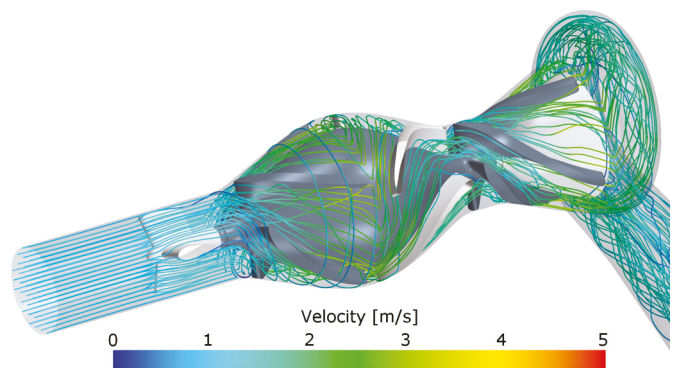


Fig. 4 - Streamlines in the two-stage pump. The fluid enters the pump from the left and leaves via the volute. The calculated flow fields appear smooth as the flow follows the shape of the blades. Highest velocities are below 4 m/s.

Figure 5 shows the comparison of the volumetric shear stress distributions for the two-stage pump and the clinically established HM II and HVAD.

Evaluating the lowest threshold of 9 Pa, which is associated with vWF degradation, the two-stage pump and the HM II feature similar characteristics while the HVAD has larger volumes exposed to shear stresses above this threshold. For the platelet

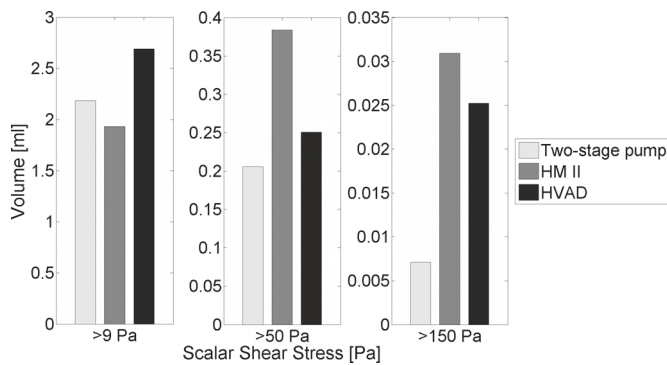


Fig. 5 - Volumetric portions of the two-stage pump, the HM II, and the HVAD that are exposed above different shear stress levels. These thresholds which were adapted from Fraser et al (2) are associated with von-Willebrand-Factor degradation (9 Pa), platelet activation (50 Pa), and hemolysis (150 Pa). The volume exposed to shear stresses above 150 Pa is reduced by more than 70% in the two-stage pump compared to the clinically used HM II and HVAD. Note the different scales for the different thresholds.

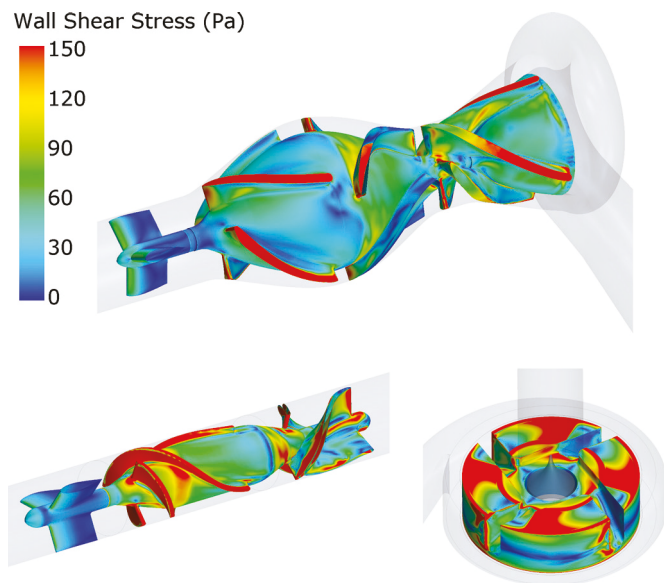


Fig. 6 - Wall shear stresses on the rotor, and stator surfaces of the two-stage pump, the HM II, and HVAD. Wall shear stresses are displayed in a range between 0 and 150 Pa. However, maximum wall shear stresses are higher: 988 Pa, 2018 Pa and 2198 Pa for the two-stage pump, the HM II and the HVAD, respectively.

activation threshold, the two-stage pump presents with lower volumes compared to the HM II but is similar to the HVAD. Above 150 Pa, which is assumed as the threshold for hemolysis, the volumetric portion of the two-stage pump is less than a third compared to the clinically used HM II and HVAD.

The calculated maximum shear stresses are 766 Pa, 1559 Pa and 3440 Pa for the two-stage pump, the HM II and the HVAD, respectively.

In Figure 6 wall shear stresses on the surfaces of the rotor, the flow straightener, and the stator are shown for the two-stage pump and the HM II and HVAD. In the two-stage pump, values as high as or higher than 150 Pa occur mainly on the

blade tips, while in the HM II the entire rotor blades' surface areas lie within this range. In the HVAD, the hydrodynamic bearing gaps as well as the blade channel inlet region show very high wall shear stress. Maximum wall shear stresses are much higher than 150 Pa: 988 Pa, 2018 Pa and 2198 Pa, for the two-stage pump, the HM II and the HVAD, respectively. Very low wall shear stresses below 1 Pa exist on a total surface area of 21.1 mm² for the two-stage pump, and 19.2 and 22.6 mm² for the HM II and HVAD, respectively. Thus, the surface area, which is potentially critical for thrombus formation, is in the same range for all three pumps.

Discussion and conclusion

Rotary blood pumps have become standard therapy for patients with severe heart failure and are increasingly applied also as destination therapy as reported in the seventh INTERMACS report (14). Kirklin et al (14) also observed a slight decrease in the total adverse event burden for the recent era. Nevertheless, the percentage of adverse events that are related to blood trauma did not decrease. In fact, the event rates for hemolysis and strokes even increased. High circumferential velocities of the rotor and consequently high shear stresses are a major cause of blood trauma and related adverse events. Therefore, the aim of this paper was to develop a rotary blood pump with reduced shear stresses where the pressure generation and consequently the blood acceleration is allocated to two stages. Such a multi-stage approach is common practice for industrial pumps, to increase the pressure head while keeping rotational speeds and rotor diameters at the same level. This advantage has already been exploited for the design of a pediatric rotary blood pump. Wu et al described how using a second set of rotor blades increased pressure heads and efficiency for the PediaFlow PF4 (21). Otherwise, the rotational speed and subsequently the circumferential velocities can be decreased when maintaining the same pressure head. To the author's knowledge, an adult two-stage rotary blood pump as presented here to reduce shear stresses has not yet been investigated.

The designed two-stage pump achieves adequate operating curves for ventricular assist devices as shown by the measured characteristic curves. Possible inaccuracies in the geometric shape of the experimental prototype along with rather rough surfaces caused by the nature of the manufacturing process might have led to increased losses and could explain the deviation from the numerically predicted pressure head. However, pressure heads of the HM II and HVAD determined both experimentally and numerically were in good agreement supporting the assumption that the applied numerical method was appropriate for the problem investigated here.

Although two stages were employed in this setup, the pump consisted of a single rotating part only. Furthermore, the bearing technology was adapted from other clinically well-established rotary blood pumps (HM II). Therefore, it can be assumed that the bearing and mechanical reliability would be similar. It must be noted that the disadvantages of this bearing technology might also lead to problems comparable to those observed in clinical studies with the HM II (22). However, the present pump was carefully designed in a way that ensured sufficient washout of the bearing regions in or-

der to decrease the likelihood of thrombus formation due to stagnation zones and temperature effects.

Velocities in general and circumferential velocities in particular, are lower in the two-stage pump compared to current single-stage axial and radial rotary blood pumps. As listed in Table I, the circumferential velocity of the blade tips was substantially decreased. Compared to the HVAD a reduction of 20% was achieved, while in comparison to the HM II even a reduction of 40% was possible. The difference was due to different hydraulic efficiency levels of the axial and radial pump designs.

Lower circumferential velocities yield lower shear stresses. Specifically, the blood volume exposed to very high shear stresses above 150 Pa could be significantly reduced by at least 70%. Thus, blood trauma related to such very high shear stresses may be reduced with the two-stage pump design presented here. However, blood volumes exposed to moderate shear stresses above 9 Pa were not reduced, so that vWF cleavage may not be diminished. It must be noted that blood trauma is known to be dependent on both shear stress and residence time, and residence times may be higher in a two-stage pump. Nevertheless, the impact of shear stresses on blood trauma is more critical in the first place based on well-established power law exponents for blood damage (23, 24). Secondly, the priming volume of the developed pump is in the same range as those for current rotary blood pumps (see Table I), so that with the same flow rate a similar range of exposure times is suggested. Furthermore, comparatively few critical regions of recirculation or vortices were revealed, which could lead to thrombus formation. Although velocities and high shear stress volumes have been reduced, the surface area with very low wall shear stresses is similar to the HM II and the HVAD.

Based on these promising results, further *in vitro* investigation of the actual blood trauma of the device is required. It must also be noted that the current design is not easy to manufacture and would need considerable revision in order to be suitable for a clinical device. Furthermore, a final prototype would presumably be somewhat larger compared to current single-stage devices. Therefore, the higher burden for manufacturing and implantation must be justified. However, the two-staged approach could be the right way to reduce blood trauma in rotary blood pumps.

Disclosures

Financial support: The project was funded by the Federal Ministry of Education and Research, Grant number 13EZ1202B.

Conflict of interest: None of the authors has financial interest related to this study to disclose.

References

- McMurray JJV, Adamopoulos S, Anker SD, et al. ESC Guidelines for the diagnosis and treatment of acute and chronic heart failure 2012. *Eur Heart J*. 2012;33:1787-847.
- Fraser KH, Zhang T, Taskin ME, et al. A quantitative comparison of mechanical blood damage parameters in rotary ventricular assist devices: shear stress, exposure time and hemolysis index. *J Biomech Eng*. 2012;134:08100201-08100211.
- Leverett LB, Hellums JD, Alfrey CP, et al. Red blood cell damage by shear stress. *Biophys. J*. 1972;12:257-73.
- Katz JN, Jensen BC, Chang PP, et al. A multicenter analysis of clinical hemolysis in patients supported with durable, long-term left ventricular assist device therapy. *J Hear Lung Transplant*. 2014;34:701-9.
- Hellums JD. 1993 Whitaker Lecture: biorheology in thrombosis research. *Ann Biomed Eng*. 1994;22:445-55.
- Uriel N, Han J, Morrison K a, et al. Device thrombosis in HeartMate II continuous-flow left ventricular assist devices: A multifactorial phenomenon. *J Heart Lung Transplant*. 2014; 33:51-9.
- Najjar SS, Slaughter MS, Pagani FD, et al. An analysis of pump thrombus events in patients in the HeartWare ADVANCE bridge to transplant and continued access protocol trial. *J Heart Lung Transplant*. 2014;33:23-34.
- Siedlecki CA, Lestini BJ, Kottke-Marchant KK, et al. Shear-dependent changes in the three-dimensional structure of human von Willebrand factor. *Blood*. 1996;88:2939-50.
- Tsai HM, Sussman II, Nagel RL. Shear stress enhances the proteolysis of von Willebrand factor in normal plasma. *Blood*. 1994;83:2171-9.
- Di Stasio E, De Cristofaro R. The effect of shear stress on protein conformation: Physical forces operating on biochemical systems: The case of von Willebrand factor. *Biophys Chem*. 2010;153:1-8.
- Geisen U, Heilmann C, Beyersdorf F, et al. Non-surgical bleeding in patients with ventricular assist devices could be explained by acquired von Willebrand disease. *Eur J Cardiothorac Surg*. 2008;33:679-84.
- Heilmann C, Geisen U, Beyersdorf F, et al. Acquired Von Willebrand syndrome is an early-onset problem in ventricular assist device patients. *Eur J Cardiothorac Surg*. 2011;40:1328-33.
- Chan CHH, Hilton A, Foster G, et al. The evaluation of leukocytes in response to the *in vitro* testing of ventricular assist devices. *Artif. Organs*. 2013;37:793-801.
- Kirklin JK, Naftel DC, Pagani FD, et al. Seventh INTERMACS annual report: 15,000 patients and counting. *J Hear Lung Transplant*. 2015;123:1-10.
- Pfleiderer C, Petermann H. *Strömungsmaschinen*. 6th ed. Berlin, Springer Berlin Heidelberg; 2013.
- Guyton AC, Hall JE. Overview of the circulation; medical physics of pressure, flow, and resistance. In: *Textbook of medical physiology*, 11th ed. Philadelphia, Elsevier Saunders, 2006, pp. 161-170.
- CD-ADAPCO. STAR-CCM+ documentation. Melville, New York; 2014.
- Merrill EW. Rheology of blood coagulation. *Physiol Rev*. 1969;49:863-117.
- Menter FR. Two-equation eddy-viscosity turbulence models for engineering applications. *AIAA J*. 1994;32:1598-605.
- Thamsen B, Blümel B, Schaller J, et al. Numerical analysis of blood damage potential of the HeartMate II and HeartWare HVAD rotary blood pumps. *Artif Organs*. 2015;39:651-9.
- Wu J, Antaki JF, Verkaik J, et al. Computational fluid dynamics-based design optimization for an implantable miniature maglev pediatric ventricular assist device. *J Fluids Eng*. 2012; 134:0411011-0411019.
- Chiu W-C, Slepian MJ, Bluestein D. Thrombus formation patterns in the heartmate ii ventricular assist device: clinical observations can be predicted by numerical simulations. *ASAIO J*. 2014;60:237-40.
- Heuser G, Opitz R. Couette viscometer for short time shearing of blood. *Biorheology*. 1980;17:17-24.
- Giersiepen M, Wurzingler LJ, Opitz R, et al. Estimation of shear-related blood damage in heart valve prostheses – *in vitro* comparison of 25 aortic valves. *Int J Artif Organs*. 1990;13:300-6.



3 Discussion

The first aim of this thesis was to gain deeper insights into the flow characteristics of established rotary blood pumps regarding potential blood trauma and resulting clinical complications. Therefore, clinically established rotary blood pumps have been numerically and experimentally investigated. These studies were described in the first two papers presented in this thesis [90,91] and will be discussed in the first part of this discussion in more detail.

As a second aim, these results should be used to develop a less-traumatic blood pump. To achieve this, a two-stage blood pump design was developed, examined and compared to the established blood pumps, which was presented in the third paper [92]. By using a diagonal design and reducing the circumferential velocities, volumetric proportions exposed to high shear stress were substantially reduced making this a potentially less traumatic blood pump. In the second part of this discussion, the concept of the two stage blood pump will be described in further detail and aspects that were not provided in the context of the publication, will be mentioned. The acquired results will be critically reviewed and limitations will be discussed. Finally, the results are evaluated and an outlook of the project is given.

3.1 Investigation of established pumps

3.1.1 Shear stresses, platelet activation and blood trauma

In the first paper, the flow fields in the HM II and in the HVAD were calculated and occurring shear stress levels in the pumps were analyzed. As described in section 1.4, all kinds of blood damage are related to high shear stresses. Three different thresholds for the different types of blood trauma were introduced to allow for a simple comparison of both pumps: Already slightly elevated shear stresses may lead to cleavage of vWF (9 Pa), higher shear stresses might trigger the activation of platelets (50 Pa) and hemolysis occurs at highest thresholds (150 Pa). As presented in Figure 5 in the first paper, exposed volumes were not substantially different in both pumps regarding the higher thresholds for hemolysis and platelet activation. However, the volumetric histograms that were shown in Figure 4, Paper I, indicated a difference in shear stress distribution. In the investigated operating point (5 L/min flow rate, 80 mmHg pressure head), the HVAD had larger volumes exposed to shear stresses up to 100 Pa, while in the HM II larger volumetric proportions were found at shear stress values between 100 and 150 Pa. Additionally, the HM II showed a much higher range of turbulent Reynolds shear stresses. The reason for that might be the fundamental difference in structure and function of both pumps: The radial HVAD pump incorporates a hydrodynamic bearing including wide blades and consequently large gap areas, which leads to larger volumes in the moderate shear stress range. The HM II is an axial pump operating at higher rotational speeds, presenting generally higher velocities which

are a result from the higher circumferential velocities and smaller flow cross sections. Consequently, both pumps also behave differently in the clinical setting. Birschmann et al. [88] reported a significant difference in hematologic effects: on one hand, there is a higher activation of the coagulation system with the HVAD, on the other hand, a higher LDH level, which is linked to stronger trauma of cells, in the pump occurred with the HMII. These observations are also in line with the findings of Tarzia et al. who reported higher platelet destruction with an axial rotary blood pump (Jarvik 2000) compared to patients supported with the HVAD who presented with higher platelet activation levels [89]. Since platelet activation is known to occur at lower shear stress levels than hemolysis, the clinical findings and the numerically derived shear stress distributions in both pumps that were presented in the first paper indicate a similar trend. Further experimental results of blood trauma with those pumps were reported by Pieper et al. who compared blood damage of the HM II, the HVAD and two other pumps in an in-vitro flow loop using animal blood in a slightly different operating point (5 L/min, 100 mmHg). In these experiments, higher hemolysis was demonstrated for the HM II [93].

In contrast to these experimental and in-vivo studies, the numerically calculated hemolysis index (Paper I) was equal in both pumps. While this result can be explained by the inherent function of the approach to calculate the hemolysis index, the disagreement indicates that this approach did not entirely reflect the real situation.

The equal hemolysis index can be explained by different residence times in the pumps which were analyzed in paper I as well. Based on cell volumes and velocities, as it was suggested by Fraser et al. [94], longer residence times were calculated in the HVAD. Since the employed approach to calculate hemolysis incorporated not only shear stresses but also exposure times, this explains the discrepancy between the lower shear stresses in the HVAD and the equal hemolysis index in both pumps.

It must be noted that the presented time values did not take the flow path into account, meaning that cell residence times were considered independently from the cell location and velocity direction. Another possibility to derive exposure times would be based on streamline or pathline computations. But pathlines depend on the seeding location and will not enter regions of vortices or low flow, so that pathlines do not represent the entire flow field equally. Consequently, there is no optimal way to calculate and compare residence times. However, with the presented approach the time values in combination with the larger total volume of the HVAD suggested higher residence times than in the HMII.

One limiting factor, that affects the used hemolysis approach, was the exclusion of turbulent characteristics. Due to the lack of experimental data linking blood damage to turbulent flow features only viscous shear stresses were considered. The effect of turbulence needs to be further investigated and included in the numerical calculation of hemolysis in the future to reflect reality more closely.

Another issue lies in the fact that blood is non-homogeneously composed of plasma and cells. Therefore, cell migration and separation as known from the Fahraeus-Lindquist effect might potentially happen in the tiny gaps of a blood pump. Antaki et al. showed a decrease of 30 % in erythrocyte concentration inside the gaps, when they visualized the blood flow in this region for a radial impeller and decreased the gap from 200 μm to 50 μm [95]. Thus, high shear stresses in these regions might not contribute to hemolysis as strong as they would in the main flow path. Correspondingly, when James et al. found no increase in hemolysis in the VentrAssist pump with smaller gaps, they suspected that less erythrocytes entered the gap [96]. Since this must be further investigated in future research, it could not be considered in the presented CFD approach.

3.1.2 Flow patterns and thrombosis

Pump thrombosis and thromboembolic events are major clinical complications in patients with rotary blood pumps. As described in section 1.4.2, not only the activation of platelets but also specific flow conditions may lead to the formation of a thrombus. It is a common strategy to avoid stagnant, slow or recirculating flows with low shear stresses. Furthermore, smooth streamlined flow fields are also required for good hydraulic efficiency.

The flow patterns in the HM II pump and the HVAD pump have been captured in detail by CFD. Areas of recirculation and vortex formation were identified in both pumps. In the HVAD, such a flow region was seen in all of the four flow channels, as shown in Figure 18 by a Line Integral Convolution (LIC) illustration on a sectional view of the pump.

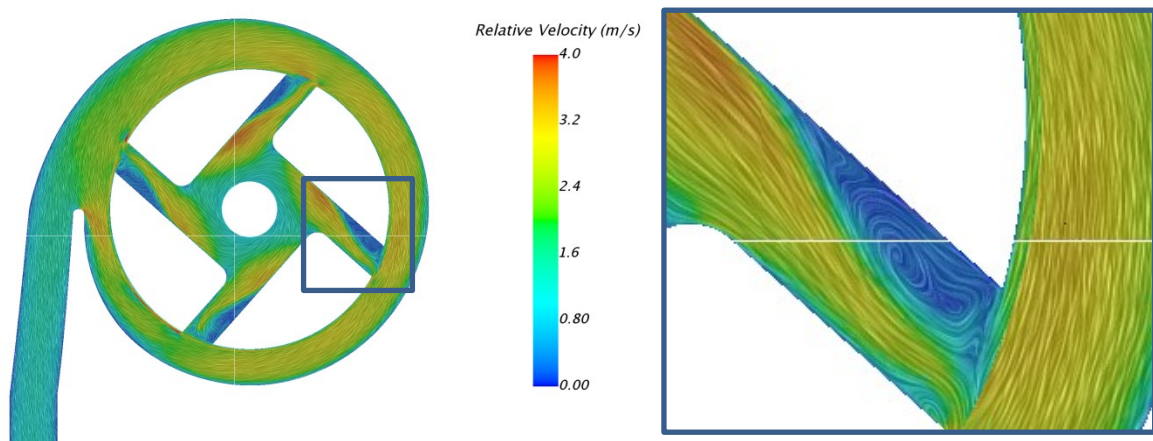


Figure 18: Recirculation zone in the flow channels of the HVAD pump. A Line Integral Convolution (LIC) illustration of the relative velocity on a sectional view through the impeller and the volute casing of the HVAD is shown, and a detail of the right channel (right). A vortex structure is seen in every blade channel on the longer suction side of the blade. The cause for this might be the inertia of the fluid that is pushed to the short side of the blade when the impeller rotates leading to a flow separation. Furthermore, the gap leakage flow entering the blade channel might contribute to this zone.

This zone is likely to be caused by the inertia of the fluid which is pushed to one side of the channel while the impeller rotates leading to a flow separation. The consequent stalled and swirling zone might be further affected by the leakage flow that enters the channel from the hydrodynamic bearing gap. However, no thrombus formations have been reported from clinics at this location.

For the HM II pump, a recirculation was identified between the flow straightener and the impeller inlet close to the housing wall, as can be seen on a sectional view in Figure 19. This might be caused by the gap leakage flow which is a backflow in opposite direction to the mean flow from the gap between the impeller blades and the housing. Furthermore, the blockage of the inlet flow cross section by the blades might prevent a portion of the inlet flow from entering the blade channels leading to a recirculated flow. Another area of recirculation was seen in the inlet area of the diffuser, most likely resulting from a flow separation caused by the sudden increase in flow cross-section due to the decrease in impeller diameter. Both these patterns were also revealed by the paint erosion method, as presented in the second paper of this thesis [91]: the flow straightener blade showed a triangular washout downstream on the outer corner and the backflow on the hub in the diffuser led to an accumulation of paint between the impeller and the diffuser. Furthermore, both these locations – the bearing site between flow straightener and impeller as well as the impeller hub that is part of the diffuser - have been reported to show thrombus formations in-vivo which can be found in literature as presented in Figure 10, section 1.4.2.

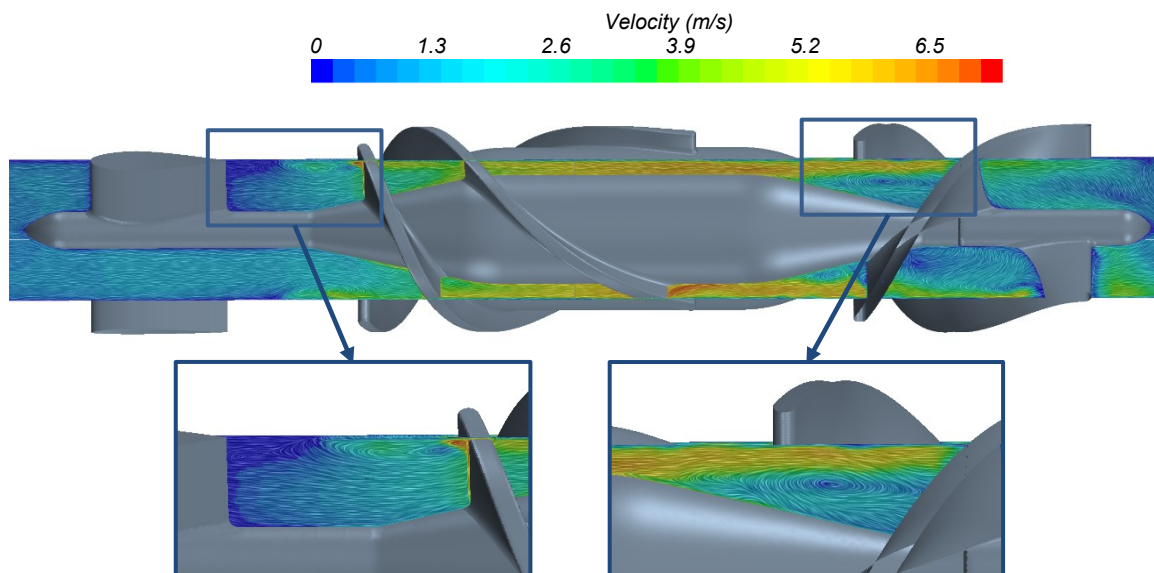


Figure 19: Flow patterns in the HMII. A vortex can be seen in the space between the flow straightener and the impeller at the housing wall. This results from a backflow from the impeller inlet and gap region. Another vortex is found close to the hub in the diffuser which might be caused mainly by the rapid decrease of the flow cross-section in this area.

3.1.3 Critical view on the used methods

Generally, a good agreement of numerical and experimental results in terms of the flow field was shown by the study presented in Paper II [91]. This suggests the CFD approach as a valid tool to investigate rotary blood pumps. However, this tool has its limitations. Whereas flow patterns derived from CFD can provide indications for potential thrombotic regions, the real thrombogenic potential of a specific pump design can only be confirmed in-vitro or in-vivo. Calculated shear stress distributions in the pumps are helpful for comparison and are valuable indicators for blood damage potential. The derivation of a hemolysis index based on CFD incorporates a relation of exposure times and shear stresses to blood trauma according to experimental results. Nevertheless, the question of turbulent effects remains open and the influence of cell migration is still unclear. Thus, state-of-the-art numerical studies are not able to mimic the real blood flow in its entire complexity, including effects like hemolysis and thrombus formation. Therefore, further in-vitro investigations using blood are necessary.

It must be noted, that the consideration of a single and constant operating point only, while the flow characteristics in connection with the cardiovascular system are far more complex, is a further limitation. However, the chosen operating conditions are typical mean flow rates and pressure heads which can be expected to be seen very frequently in the clinical application. Hence, these methods enable to indicate potential critical zones and specific trends. Accordingly, CFD is a helpful tool to describe the performance of rotary blood pumps and to capture the flow characteristics, such as shear stress levels and flow patterns. Thus, this method was employed to support the development process of a new pump design and to evaluate its traumatic potential.

3.2 A design for a less-traumatic rotary blood pump

Most state-of-the-art rotary blood pumps are single stage pumps deploying only one impeller to generate the required pressures and flows. The circumferential velocities of the impeller blade tips contribute not only to the energy transfer but also to the highest shear stresses occurring in the flow field. In the HM II, the circumferential velocity was around 6 m/s, which leads to shear stresses around 200 Pa, calculated based on a gap size of 100 μm and the assumption of a linear velocity profile in the gap as in Eq. 4. As described earlier, blood damage is related to high shear stresses. To reduce the blood damage, circumferential velocities must be drastically decreased. This can only be achieved with a pump composed of multiple stages.

Already in 1995, it was shown that a significant reduction of hemolysis can be achieved if two pumps are operated in series. Wakisaka et al. [97] compared the hemolysis index of a single miniature axial pump with two similar axial pumps in series at the same operating point using goat blood. The experimental setup is partially illustrated in Figure 20. The pumps in series configuration had a 50 % lower hemolysis index at 40 % reduced rotational speed. This was a very simple approach where the pumps were driven via a shaft connected to an external motor making sealings necessary which produce friction and might therefore have an influence on hemolysis as well. Furthermore, geometric accuracy of the manufactured pumps and reproducibility of the results were not reported. But still, the results indicate a less-traumatic potential of the series approach.

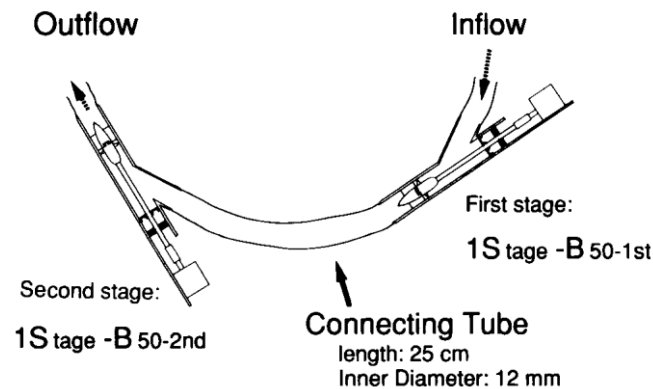


Figure 20: Two miniature axial pumps in series operation [97]. Wakisaka et al showed that two axial pumps in series have a substantially lower hemolysis index (<50 %) compared to one axial pump in the same operating point.

An example for a rotary blood pump employing more than one stage is the Pediaflow PF4 pump that is described in reference [98]. In this pump, a first set of diagonal impeller blades is followed by an additional set of axial blades before the blood enters the diffuser. Compared to a version without the second set of blades, the PF4 achieved similar pressure heads with by around 40 % reduced rotational speeds. Nevertheless, this pump differs from a “real” two-stage pump design

because no guide apparatus was applied between the two sets of impeller blades. The PF4 was intended for pediatric use and was never introduced into clinic.

Recently, a two-stage radial rotary blood pump concept was presented by Horiguchi et al. [99]. The pump was proposed for extracorporeal use, which requires higher pressure heads due to the long tubes connecting the pump to the circulatory system as well as additional resistances caused by oxygenators. Thus, extracorporeal pumps involve a higher rotational speed. The authors suggested to use two radial impellers in series configuration to reduce the speed and consequently blood trauma. Although this is an interesting concept, size restrictions prohibit potential use as an implantable pump which was the goal of this thesis.

Different design concepts were considered for the development of a multi-stage rotary blood pump. The main aim was to achieve an improved hemocompatibility. Most importantly, the impeller circumferential velocity should be reduced while still achieving physiological operating points. Moreover, flow characteristics in the pump should be hydrodynamically optimized for smooth flow fields free of critical recirculation or low flow regions. A further requirement was a device volume suitable for an implantable device. In addition, the development had to consider manufacturing requirements. As complex designs with multiple parts and functions are increasingly difficult to produce, the complexity of the final design should be kept in a reasonable range. Although this thesis focused on the flow characteristics, the integration of a bearing and a motor drive had to be considered as well. An overview of the objectives is given in the following Figure 21.

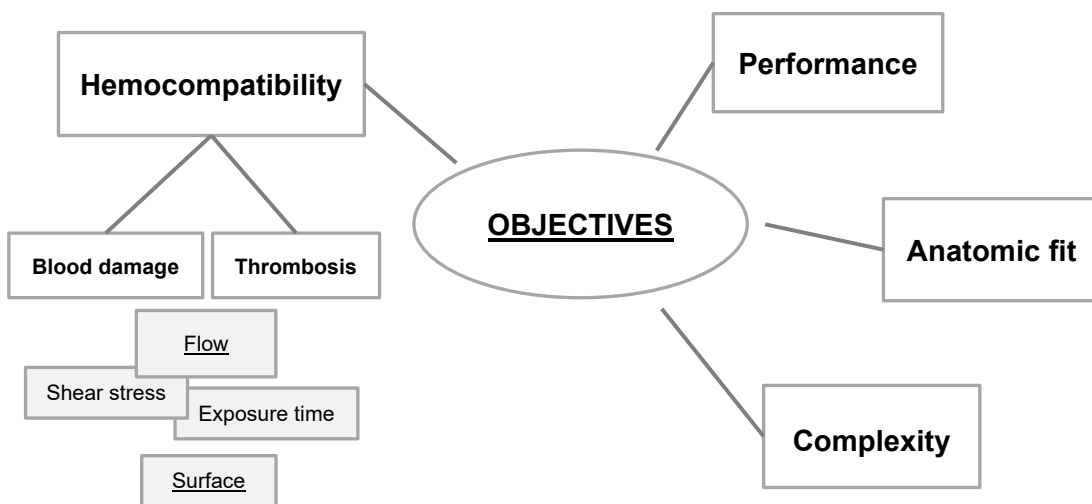


Figure 21: Overview of objectives considered the development of a multistage rotary blood pump. While a good hemocompatibility was the main objective, a physiologic performance, anatomic fit, a manageable complexity as well as good manufacturability were also required.

Based on theoretical considerations, the extent, to which the circumferential velocity might be reduced, shall be estimated. It can be derived from Eq. 12 that the transmitted energy by an impeller and subsequently the pressure head Δp depend on the square of the velocities:

$$\Delta p \propto u^2 \quad \text{Eq. 21}$$

Thus, when the pressure head is evenly distributed to the number of stages, the circumferential velocity of each stage u_{stage} might be calculated by multiplying the respective single stage circumferential velocity u_{orig} by the square root of the number of stages:

$$u_{orig}^2 = n \cdot u_{stage}^2 \Rightarrow u_{orig} \cdot n^{-1/2} = u_{stage} \quad \text{Eq. 22}$$

Consequently, for four stages a reduction of the original circumferential velocity u_{orig} of 50 % might be feasible, for three stages it can theoretically be decreased to 58 %, and a number of two stages allows for a decrease to 70 % compared to a single stage. In the following section, different design options are discussed.

3.2.1 Possible configurations

In the framework of this thesis, different concepts of multiple stage configurations for a rotary blood pump have been considered and revised. For this purpose, a matrix of possible permutations was set up. As a first step, the number of stages was defined. Although the possible reduction of circumferential velocity increases with the number of stages, the design becomes larger and more complex. Therefore, the number of stages was limited to two.

In a second step, impossible or undesired configurations were rejected. For instance, a volute as guide apparatus for the first stage would be disadvantageous. Remaining possible combinations are listed and evaluated in Table 2.

Table 2: Possible design configurations for a two-stage rotary blood pump. The permutations were evaluated using -, 0, or + meaning bad, neutral or good properties, respectively.

First stage	Second stage	Performance	Size (anatomic fit)	Complexity
Axial + diffuser	Axial + diffuser	-	0	+
Axial + diffuser	Radial + diffuser	0	-	-
Axial + diffuser	Radial + volute	0	+	-
Radial + diffuser	Axial + diffuser	0	-	-
Diagonal + diffuser	Diagonal + diffuser	+	0	0
Diagonal + diffuser	Diagonal + volute	+	+	0

One possibility was to compose the pump of fully axial stages. However, axial pumps operate best at high rotational speeds and become inefficient for the intended lower speeds. Consequently, it was advisable to incorporate a radial component in the impeller design. The corresponding increase of the mean circumferential velocity of the fluid on transit through the impeller allows for higher pressure heads at equal diameters, as can be seen from Eq. 12. A combination of a first axial and a second radial stage with volute seemed adequate for anatomic fitting with an outer structure comparable to the design of the HVAD. The disadvantage of this concept was the lower impeller diameter of the axial stage compared to that of the radial impeller which subsequently required different rotational speeds for both stages to achieve a well distributed pressure generation via the pump. This led to a very complex system. In fact, this configuration was examined and the possibility of opposite directions of rotation for the two stages was investigated as shown in Figure 22.



Figure 22: Two-stage pump design with an axial and a radial stage that rotate in opposite directions. Such design configurations were evaluated in the early stage of the development of a multi-stage blood pump.

In this case, the whirling fluid from the first stage was directly taken up and redirected by the second stage, thereby allowing for a high pressure generation while the stator between both stages could be small or even left out. Nevertheless, this option was discarded due to the very high complexity of the drive system and bearing.

Hence, it was preferred to use two similar stages with the same outer diameter which should be combined into one rotating part only. Diagonal stages were the intuitive choice as they represent a compromise between axial and radial versions and have several advantages: As an important aspect, the outlet flow direction of diagonal impellers is not fully radial so that they are more practical to be arranged as two stages [64]. Furthermore, diagonal impellers have a specific speed of about 50 which is the specific speed with the highest effective output, as shown in Figure 23 [65].

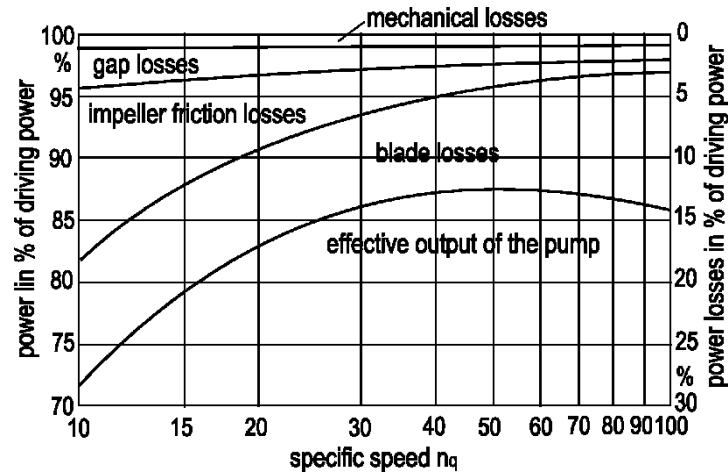


Figure 23: Power balance of centrifugal pumps (radial and diagonal) in their best efficiency point depending on the specific speed [65]. Diagonal pumps with a specific speed of around 50 generate highest effective outputs and are therefore the most frequently used types.

The reason for this is that diagonal impellers have an optimum relation between wetted surface and flow rate which makes them the most frequently used pump type. Consequently, a diagonal impeller design was selected and a specific speed of around 50 was aspired.

3.2.2 Pump design

The pump design was already briefly presented in paper III [92]. Additionally, it shall be described in more detail in this section. Figure 24 shows the schematic design of the developed two stage pump in a sectional view with the blade edges projected onto the view plane. The outer diameter of the pump was set to 22 mm, inlet and outlet diameters were set to 11 mm and 12 mm, respectively. Both stages used diagonal impeller blades. A diagonal diffuser was chosen to complete the first stage and guide the fluid to the second stage in a way that the inlet flow to the second stage is axial again. A volute behind the second stage blades was selected because of two major advantages: First, the outflow direction of the volute is perpendicular to the inflow of the pump, which is beneficial to create the connection to the aorta. Furthermore, a volute casing is known to be more forgiving in off-design conditions. This is an important point, since the operating point of a centrifugal pump connected to the circulatory system is not constant due to the remaining activity of the heart. Consequently, a range of operating points must be considered for the design of a rotary blood pump and the design point must be chosen as a mean operating point which is expected to occur most frequently during operation. Thus, the design point was specified at a flow rate of 5 L/min.

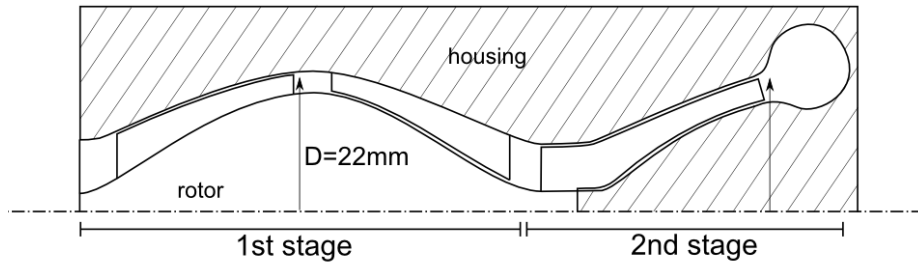


Figure 24: Schematic design of the hydrodynamic parts of the two-stage blood pump. In this sectional view the blade edges have been projected to the view plane so that the flow channel becomes apparent.

With the known diameters and the design point flow rate, the blade angles at inlet and outlet of the impeller and the diffuser were calculated based on the theory presented in section 1.5. The remaining design parameters could not be calculated, but were defined to the author's best knowledge:

- The blade shape: The shape of the impeller and diffuser blades was designed so that the course of the blade angle from inlet to outlet was linear. Furthermore, the axial length of the blades was chosen to be 14 mm which is relatively long compared to standard diagonal impeller designs but results in a slower pressure build-up and thereby, a more gentle energy transfer.
- The number of blades: The flow straightener was designed with three blades which was adapted from the Heartmate II pump. The number of rotor blades was set to four. The diffuser had four blades as well which eased manufacturing and assembly.
- The shape of the hub: The hub was shaped based on a square root function which determines the increase of the circumferential velocity from inlet to outlet. Thereby, a uniform energy transfer is implemented since the transmitted work by the impeller depends on the square of the velocity.
- The shape of the inner housing: Based on the hub shape, the housing shape was designed to obtain a linearly changing flow cross-section with a minimum channel height of 2 mm.
- The gap between impeller and stationary parts. The gap width was set to 100 μm which is a commonly used gap width in rotary blood pumps.

The resulting two-stage pump was achieved a pressure head of 70 mmHg at 3200 rpm for the design point flow rate of 5 L/min. This led to a specific speed of 53, which was very close to the desired specific speed.

3.2.3 Operating behavior

The development process was supported by measuring the characteristic curves of rapid prototyping manufactured models, as described in paper III [92]. For this purpose, the pump model was manufactured using stereolithography and the characteristic curves were measured in the test stand, as depicted in section 1.6.4.

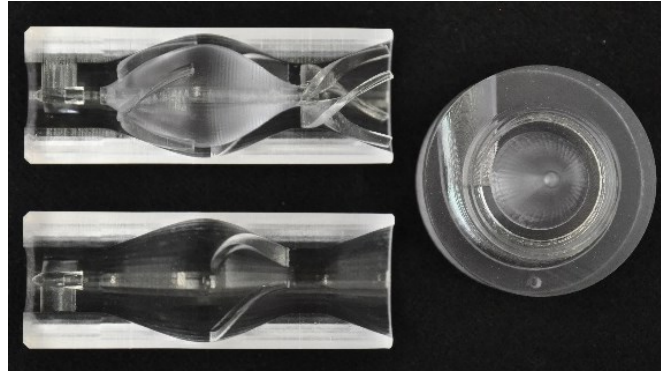


Figure 25: Stereolithography fabricated pump parts that were used for measuring the characteristic curves. The surface of the models was manually finished with sand paper in preparation of the measurements.

The stereolithography technique uses a polymer resin that is solidified in successive layers by an ultraviolet laser light. This printing process reaches accuracies of $50\ \mu\text{m}$ [100] which results in a relatively rough surface and can be considered quite inaccurate regarding the gap width of $100\ \mu\text{m}$. Therefore, the models fabricated in this way were not suitable to pump blood and were used only to qualitatively capture the hydrodynamic performance. Figure 25 shows the parts of the pump that were integrated into the test stand. The surface of the models was manually finished with fine sand paper (P1200-2000) in preparation of the measurements.

The measured characteristic curves, as presented in paper III [92], were used to describe the operating behavior of the pump. The attained characteristic curves showed a pressure head that steadily falls with increasing flow rate without showing any instabilities. This behavior is termed stable in contrast to a behavior where the pressure head at zero flow is not the maximum pressure head. In such a case, a given pressure head is related to different flow rates which might lead to a disadvantageous oscillating operation of the pump [101].

In comparison to the established blood pumps, the characteristic curves of the two-stage pump were very similar to those of the HVAD, which is a radial pump. Hydrodynamic performance of axial and radial pumps basically differs (see section 1.5): While radial pumps have a flat curve, axial pump curves are steeper. The hydrodynamic performance or more specifically the slope of the characteristic curve represents the pressure head sensitivity of a pump and therefore the interaction between the cardiovascular system and the device. Since the pump is connected to a pumping heart, pressure conditions at the inlet and outlet are varying. For the same pressure

conditions during a cardiac cycle, the flatter characteristics of a radial pump lead to a higher flow variation compared to axial pumps, as illustrated in Figure 26. This higher flow variations might result in higher blood pressure pulsatility which is suspected to be beneficial for endothelial function and bleeding [13,102]. Furthermore, due to the steep characteristic of the axial flow pumps the pressure head at zero flow is higher even when the mean operating points match that of a radial pump. In patients with rotary blood pumps, a sudden suction of the ventricular septum or the ventricular wall towards the pump inlet is frequently observed. Such a suction event results from excessive emptying of the ventricle and/or misplacement of the inflow cannula and might lead to myocardial damage, increased blood damage and cardiac arrhythmia [103]. Consequently, it might be reasonable to speculate that a radial pump with a lower zero-flow pressure leads to less suction-related complications [104].

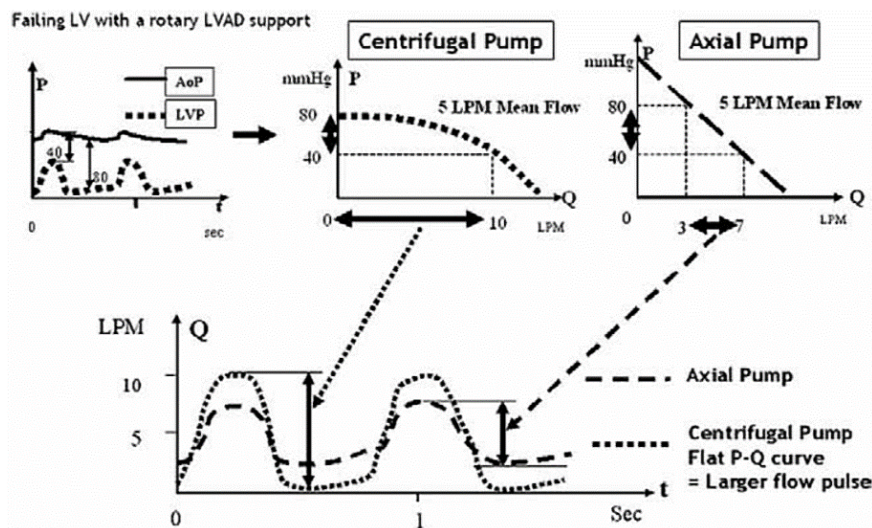


Figure 26: A: Time course of aortic pressure (AoP) and left ventricular pressure (LVP) during two cardiac cycles of a heart failure patient. B: Typical flat characteristic curve of a radial pump. C: Typical steep characteristics of an axial pump. D: Translation of different hydrodynamic characteristic to pump output during two cardiac cycles [105]. The flatter slope of radial pumps translates into a higher pulsatility of the volume flow.

Another advantage of such a flat characteristic curve is a high sensitivity of the pump to the ventricular pressure, which is referred to as pre-load sensitivity. This means that the pump flow increases in case of an increased filling pressure, which is similar to the behavior of the native heart. In contrast, the function of a native heart is only slightly dependent on the aortic pressure or after-load. Although, there is no ideal characteristic curve that would lead to a physiologic hydrodynamic behavior similar to the native heart, a flat curve as achieved with the two-stage blood pump was considered advantageous compared to the steeper axial curves due to the previously described reasons.

During experimental and numerical investigations in this thesis, a dynamic viscosity of 3.5 mPas was assumed to be representative for the average patient blood viscosity. Nevertheless, the blood viscosity of an LVAD patient may vary widely in case of bleeding, hypovolemia or excessive hemolysis. Thus, the influence of the viscosity on the pump's characteristic curve was investigated by adjusting the mixing ratio of the water-glycerol mixture. The resulting curves for 1, 3 and 5 mPas are shown in Figure 27.

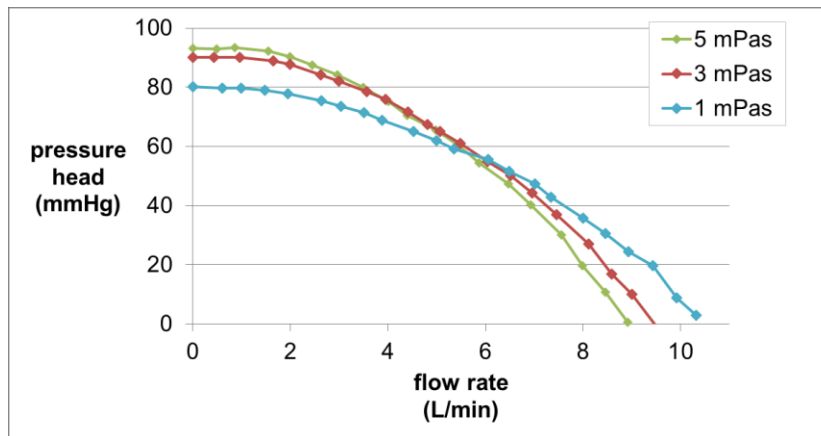


Figure 27: Measured characteristic curves of the two-stage pump model for different dynamic viscosities.

While pressure heads around the mean operating point at 5 L/min flow rate do not change substantially, a slight shift to higher slopes with increasing viscosity can be seen. The overall flat characteristic remains.

3.2.4 The bearing concept

The bearing concept for the presented pump, which is a mechanical cup-socket bearing, was adapted from the HM II. In this bearing, very hard materials such as ruby or ceramics are in mechanical contact. The contact is established through a sphere that rotates in a socket. A good thermal conductivity of the material is required to quickly remove friction heat. By such a mechanical bearing, the suspension of the rotating impeller is ensured for all directions and independent of the operating conditions. This bearing design is simple in structure and could easily be integrated into the pump design. However, as already discussed in paper III [92], this bearing is suspected of causing thrombus formation due to friction heat and not optimal washing of the bearing site. Thus, during pump design it was tried to ensure good washing of this area. The front bearing was placed between the flow straightener and the impeller with a distance of approximately 3 mm to the straightener vanes as well as one rotor blade height to the rotating blades. In this way, a direct interaction of the flow around the bearing with the more complex flow at the flow straightener outlet and the impeller inlet should be prevented. With the help of

CFD, this area was investigated for recirculation zones as occurring in the HM II upstream of the rotor as shown in papers I and II [90,91]. Compared to the HM II, flow in this area is smoother suggesting an improved washing. The rear bearing was placed downstream of the inlet of the second stage in the first third of the blade channel. Although the flow appears to be more disturbed in this area due to the direct interaction with the impeller flow, blood velocities are higher and additional washing is produced by the blades of the second stage which rotate around the bearing. However, these areas should be further investigated in more detail regarding low flow operating conditions and heat generation in the future.

During the concept phase, alternative bearing concepts were evaluated as well and shall be discussed in this section. A brief overview of bearing concepts used in rotary blood pumps is given by Moazami et al [104]. Besides mechanical bearings, also magnetic or hydrodynamic bearings or a combination of both have been used in rotary blood pumps. The advantage of these bearing types is that they eliminate mechanical contact and thus, potentially life-limiting wear.

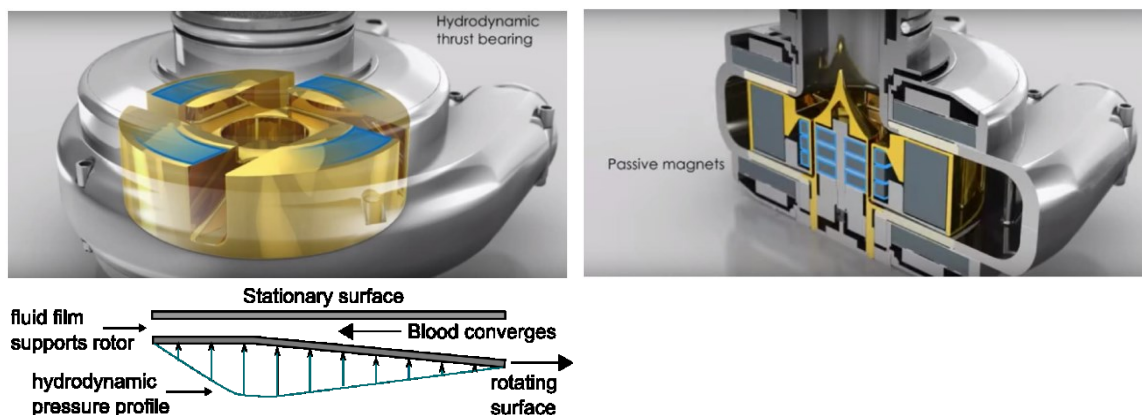


Figure 28: Bearing concepts used to suspend the rotor of the HVAD. Left, upper: The tapered upper surface of the impeller creates a hydrodynamic bearing [106]. Lower: Working principle of an axial hydrodynamic bearing, adapted from [104]. Right: passive magnetic bearing in the HVAD. [106]

In a hydrodynamic bearing as in the HVAD, the impeller surface is tapered so that a wedge structure is created and fluid is pushed into the bearing when the rotor rotates. Thereby, a thin fluid film between the stationary wall and the rotating impeller is created generating a pressure force, as shown in Figure 28. However, a minimum rotational speed is required to stabilize the bearing. Furthermore, shear stresses in the bearing gap are usually high, leading to excessive load on the blood.

Magnetic bearings use magnetic forces to suspend the impeller. In a passive magnetic bearing, permanent magnets inside of the rotor and the stator are either attracting or repelling each other creating a unidirectional force. This is the case for the center post of the HVAD (Figure 28). In contrast, electromagnetic forces by additional stator coils can actively control the position of

the permanent rotor magnets like it is the case in the HM 3 (see section 1.2.3). Larger gaps and theoretically zero rotational speed are possible, but active electromagnetic bearings are very complex and make use of sensors. In general, both bearing concepts would require substantial redesign of the two-stage pump.

3.2.5 Manufacturability

The current design was not easy to manufacture due to the complex three-dimensional shape of the rotor and stators. Thus, the construction would need considerable revision in order to be suitable for a commercial clinical device in series production. However, this was not an objective of this thesis.

For a detailed in-vitro investigation of blood damage with the presented two-stage pump design, a functional biocompatible prototype will be required and therefore, a few remarks on manufacturability of the design shall be made: To manufacture the impeller from titanium which has acceptable biocompatible properties, a 5-axis mill is needed. The housing can be produced in several parts: two halves separated along the axis around the impeller, one cylinder containing the flow straightener, and two radially separated parts for the volute. The volute would need slight revision to remove undercuts. Surface finishing of all parts would be an elaborate manual process. Due to the large number of parts, the final assembly is susceptible for steps and gaps at all junctions. Figure 29 shows some parts of a prototype for blood testing which will be carried out in future work.



Figure 29: *Parts of a prototype of the two-stage pump for in-vitro measurements of blood damage. The two-part impeller was milled from titanium, the housing was composed of six different parts made from plastics (polymethyl methacrylate) and stainless steel.*

3.2.6 Efficiency

The diagonal design was chosen for the two-stage pump based on the empirical relationship presented in Figure 23 which shows diagonal pumps with specific speeds around 50 to have the

best efficiency. The hydraulic efficiency were obtained from CFD results: Based on the torque that is transmitted through the impeller and the rotational speed the mechanical power was derived, and the hydrodynamic power was calculated from the pressure head and the volume flow. In this way, for the operating point of 5 L/min and 69 mmHg at 3,200 rpm a hydraulic efficiency of 47 % was obtained, which is high compared to other devices. The efficiency of the HVAD was calculated to be 32 %, and the HMII had an efficiency of 25 % at the same hydrodynamic conditions. A good efficiency implies good flow conditions, meaning flow that is tangential to the blades with less flow separations since these are associated with higher hydraulic losses [101]. Consequently, a good efficiency might be related to less critical flow patterns regarding blood trauma and thrombus formation.

3.2.7 Blood trauma in the two-stage pump

In paper III [92], volumetric portions of fluid inside the two-stage pump that were exposed to three different shear stress thresholds (9 Pa for vWF degradation, 50 Pa for platelet activation, and 150 Pa for hemolysis) were computed. These values were compared to the HVAD as well as the HM II and it was shown that volumes exposed to very high shear stresses were reduced by 70 %. At lower shear stress levels, the two stage pump could not achieve decisively better results. At the level related to platelet activation the two stage pump was only slightly better than the HVAD, though still almost 50 % better than the HM II. At lower shear stresses the volumes in the three pumps were similar with the HM II presenting smaller volumes than the other two and the HVAD having the largest proportion. Thus, based on these numeric results, the two-stage approach achieved a significant reduction of very high shear stresses but showed no substantial improvement at lower shear stress levels. An investigation of actual blood trauma in-vitro using blood in a flow loop driven by the pump is required to confirm these indications. Particularly, such experiments include all effects that could not completely be covered by the numerical approach, such as exposure times and turbulent effects. Since a good correlation was seen between clinical findings and numerical results of the HVAD and HM II, it can be expected that the CFD results will be proven by in-vitro experiments.

Regarding the activation of platelets and the degradation of vWF which were observed in all patients with rotary blood pumps so far, only slight improvements seem to be possible with the presented design variation.

3.3 Summary and outlook

In the frame of this thesis, three main achievements have been accomplished:

Numerical descriptions of the flow fields in the two most frequently used rotary blood pumps were provided, giving new insights into the flow characteristics and shear stress levels of both pumps.

The wall-PIV technique and the paint erosion method were employed to capture flows close to the housing wall and to visualize flow patterns on the inner pump parts of the HM II. The flow close to the surface is most critical with regard to blood damage. Very good agreement of numerical and experimental results formed a valid basis for a numerical investigation of a new pump design.

Finally, a new two-stage diagonal blood pump design was developed, examined and compared to the established pumps indicating a lower potential to cause blood damage due to reduced circumferential speed.

In-vitro investigations of the actual blood trauma will be conducted in the future to confirm the numerical results.

References

- [1] A. C. Guyton and J. E. Hall, "Heart Muscle; The Heart as a Pump and Function of the Heart Valves," in *Textbook of Medical Physiology*, 11th ed., Philadelphia: Elsevier Saunders, 2006, pp. 103–114.
- [2] G. G. Belz, "Elastic properties and Windkessel function of the human aorta.," *Cardiovasc. Drugs Ther.*, vol. 9, no. 1, pp. 73–83, 1995.
- [3] A. C. Guyton and J. E. Hall, "Overview of the Circulation; Medical Physics of Pressure, Flow, and Resistance," in *Textbook of Medical Physiology*, 11th ed., Philadelphia: Elsevier Saunders, 2006, pp. 161–170.
- [4] A. C. Guyton and J. E. Hall, "The Microcirculation and the Lymphatic System," in *Textbook of Medical Physiology*, 11th ed., Philadelphia: Elsevier Saunders, 2006, pp. 181–194.
- [5] K. T. Patton, "Blood vessels," in *Anatomy and Physiology*, 9th ed., St. Louis, Missouri: Elsevier, 2015, p. 1264.
- [6] C. Michiels, "Endothelial cell functions," *J. Cell. Physiol.*, vol. 196, no. 3, pp. 430–43, 2003.
- [7] L.-E. Copstead-Kirkhorn and J. L. Banasik, "Heart Failure and Dysrhythmias: Common Sequelae of Cardiac Diseases," in *Pathophysiology*, 5th ed., St. Louis, Missouri: Elsevier Saunders, 2013, pp. 408–431.
- [8] "State & society - Causes of death - Federal Statistical Office (Destatis)." [Online]. Available: <https://www.destatis.de/EN/FactsFigures/SocietyState/Health/CausesDeath/CausesDeath.html>. [Accessed: 25-Jan-2016].
- [9] Eurotransplant International Foundation, "Annual Report 2014," Leiden, 2014.
- [10] J. K. Kirklin, D. C. Naftel, F. D. Pagani, R. L. Kormos, L. W. Stevenson, E. D. Blume, S. L. Myers, M. a. Miller, J. T. Baldwin, and J. B. Young, "Seventh INTERMACS annual report: 15,000 patients and counting," *J. Hear. Lung Transplant.*, vol. 123, pp. 1–10, 2015.
- [11] E. A. Rose, A. J. Moskowitz, M. Packer, J. A. Sollano, D. L. Williams, A. R. Tierney, D. F. Heitjan, P. Meier, D. D. Ascheim, R. G. Levitan, A. D. Weinberg, L. W. Stevenson, P. A. Shapiro, R. M. Lazar, J. T. Watson, D. J. Goldstein, and A. C. Gelijns, "The REMATCH trial: rationale, design, and end points. Randomized Evaluation of Mechanical Assistance for the Treatment of Congestive Heart Failure.," *Ann. Thorac. Surg.*, vol. 67, no. 3, pp. 723–30, Mar. 1999.
- [12] J. J. V McMurray, S. Adamopoulos, S. D. Anker, A. Auricchio, M. Böhm, K. Dickstein, V. Falk, G. Filippatos, C. Fonseca, M. A. Gomez-Sanchez, T. Jaarsma, L. Køber, G. Y. H. Lip, A. Pietro Maggioni, A. Parkhomenko, B. M. Pieske, B. a Popescu, P. K. Rønnevik, F. H. Rutten, J. Schwitter, P. Seferovic, J. Stepinska, P. T. Trindade, A. a Voors, F. Zannad, and A. Zeiher, "ESC Guidelines for the diagnosis and treatment of acute and chronic heart failure 2012," *Eur. Heart J.*, vol. 33, pp. 1787–847, Jul. 2012.
- [13] T. Hasin, Y. Matsuzawa, R. R. Guddeti, T. Aoki, T. G. Kwon, S. Schettle, R. J. Lennon, R. G. Chokka, A. Lerman, and S. S. Kushwaha, "Attenuation in peripheral endothelial function after continuous flow left ventricular assist device therapy is associated with cardiovascular adverse events," *Circ. J.*, vol. 79, no. 4, pp. 770–777, 2015.
- [14] O. Marseille, "Entwicklungs- und Bewertungsverfahren für Rotationsblutpumpen," RWTH Aachen, 2001.
- [15] C. A. Milano and A. A. Simeone, "Mechanical circulatory support: Devices, outcomes and complications," *Heart Fail. Rev.*, vol. 18, pp. 35–53, 2013.
- [16] S. Sathishkumar, R. Kodavatiganti, S. Plummer, and K. High, "Perioperative management of a patient with an axial-flow rotary ventricular assist device for

- laparoscopic ileo-colectomy,” *J. Anaesthesiol. Clin. Pharmacol.*, vol. 28, no. 1, pp. 101–5, 2012.
- [17] D. Timms, “A review of clinical ventricular assist devices,” *Med. Eng. Phys.*, vol. 33, no. 9, pp. 1041–7, Nov. 2011.
- [18] F. D. Pagani, L. W. Miller, S. D. Russell, K. D. Aaronson, R. John, A. J. Boyle, J. V Conte, R. C. Bogaev, T. E. MacGillivray, Y. Naka, D. Mancini, H. T. Massey, L. Chen, C. T. Klodell, J. M. Aranda, N. Moazami, G. a Ewald, D. J. Farrar, and O. H. Frazier, “Extended mechanical circulatory support with a continuous-flow rotary left ventricular assist device,” *J. Am. Coll. Cardiol.*, vol. 54, no. 4, pp. 312–21, Jul. 2009.
- [19] M. S. Slaughter, J. G. Rogers, C. a Milano, S. D. Russell, J. V Conte, D. Feldman, B. Sun, A. J. Tatooles, R. M. Delgado, J. W. Long, T. C. Wozniak, W. Ghumman, D. J. Farrar, and O. H. Frazier, “Advanced heart failure treated with continuous-flow left ventricular assist device,” *N. Engl. J. Med.*, vol. 361, no. 23, pp. 2241–51, Dec. 2009.
- [20] “Thoratec Corporation - Trials & Outcomes - Clinical Outcomes - HeartMate II LVAD.” [Online]. Available: <http://www.thoratec.com/vad-trials-outcomes/clinical-outcomes/heartmate-ii-lvad.aspx>. [Accessed: 21-Jan-2016].
- [21] “Image Library | HeartWare.” [Online]. Available: <http://www.heartware.com/resources>. [Accessed: 21-Jan-2016].
- [22] J. A. LaRose, D. Tamez, M. Ashenuga, and C. Reyes, “Design concepts and principle of operation of the HeartWare ventricular assist system,” *ASAIO J.*, vol. 56, no. 4, pp. 285–289, 2010.
- [23] K. D. Aaronson, M. S. Slaughter, L. W. Miller, E. C. McGee, W. G. Cotts, M. a Acker, M. L. Jessup, I. D. Gregoric, P. Loyalka, O. H. Frazier, V. Jeevanandam, A. S. Anderson, R. L. Kormos, J. J. Teuteberg, W. C. Levy, D. C. Naftel, R. M. Bittman, F. D. Pagani, D. R. Hathaway, and S. W. Boyce, “Use of an intrapericardial, continuous-flow, centrifugal pump in patients awaiting heart transplantation,” *Circulation*, vol. 125, no. 25, pp. 3191–200, Jun. 2012.
- [24] I. Netuka, P. Sood, Y. Pya, D. Zimpfer, T. Krabatsch, J. Garbade, V. Rao, M. Morshuis, S. Marasco, F. Beyersdorf, L. Damme, and J. D. Schmitto, “Fully Magnetically Levitated Left Ventricular Assist System for Treating Advanced HF: A Multicenter Study,” *J. Am. Coll. Cardiol.*, vol. 66, no. 23, pp. 2579–2589, 2015.
- [25] D. J. Farrar, K. Bourque, C. P. Dague, C. J. Cotter, and V. L. Poirier, “Design features, developmental status, and experimental results with the Heartmate III centrifugal left ventricular assist system with a magnetically levitated rotor,” *ASAIO J.*, vol. 53, no. 3, pp. 310–5, 2007.
- [26] A. Cheung, K. Chorpenning, D. Tamez, C. Shambaugh, A. E. Dierlam, M. E. Taskin, M. Ashenuga, C. Reyes, and J. A. Larose, “Design Concepts and Preclinical Results of a Miniaturized Heartware Platform: The MVAD System,” *Innovations*, vol. 10, no. 3, pp. 151–156, 2015.
- [27] A. C. Guyton and J. E. Hall, “Blood Cells, Immunity, and Blood Clotting,” in *Textbook of Medical Physiology*, 11th ed., Philadelphia: Elsevier Saunders, 2006, pp. 417–467.
- [28] Z. M. Ruggeri, “The role of von Willebrand factor in thrombus formation,” *Thromb. Res.*, vol. 120 Suppl, pp. 5–9, Jan. 2007.
- [29] V. Huck, M. F. Schneider, C. Gorzelanny, and S. W. Schneider, “The various states of von Willebrand factor and their function in physiology and pathophysiology,” *Thromb. Haemost.*, vol. 111, no. 4, pp. 598–609, Apr. 2014.
- [30] M. W. Rampling, “Compositional Properties of Blood,” in *Handbook of Hemorheology and Hemodynamics*, Amsterdam: IOS Press, 2007.
- [31] E. W. Merrill, “Rheology of blood coagulation,” *Physiol. Rev.*, vol. 49, no. 4, pp. 863–117,

- 1969.
- [32] J. R. Cokelet and H. J. Meiselman, "Macro- and Micro-Rheological Properties of Blood," in *Handbook of Hemorheology and Hemodynamics*, Amsterdam: IOS Press, 2007, pp. 45–71.
- [33] N. L. Gershfeld and M. Murayama, "Thermal instability of red blood cell membrane bilayers: temperature dependence of hemolysis.," *J. Membr. Biol.*, vol. 101, no. 1, pp. 67–72, Jan. 1988.
- [34] L. B. Leverett, J. D. Hellums, C. P. Alfrey, and E. C. Lynch, "Red blood cell damage by shear stress.," *Biophys. J.*, vol. 12, no. 3, pp. 257–273, 1972.
- [35] P. L. Blackshear and G. L. Blackshear, "Mechanical hemolysis," in *Handbook of Bioengineering*, R. Skalak and S. Chien, Eds. New York: McGraw-Hill, 1987, pp. 15.1–15.19.
- [36] M. V. Kameneva and J. F. Antaki, "Mechanical Trauma to Blood," in *Handbook of Hemorheology and Hemodynamics*, Amsterdam: IOS Press, 2007, pp. 206–227.
- [37] R. Paul, J. Apel, S. Klaus, F. Schügner, P. Schwindke, and H. Reul, "Shear stress related blood damage in laminar Couette flow," *Artif. Organs*, vol. 27, no. 6, pp. 517–529, 2003.
- [38] G. Heuser and R. Opitz, "Couette viscometer for short time shearing of blood," *Biorheology*, vol. 17, pp. 17–24, 1980.
- [39] H. Herwig, *Strömungsmechanik A-Z: Eine systematische Einordnung von Begriffen und Konzepten der Strömungsmechanik*, 1st ed. Hamburg: Springer-Verlag Berlin Heidelberg, 2004.
- [40] L. J. Wurzinger, R. Opitz, and H. Eckstein, "Mechanical Blood Trauma. An Overview," *Angiologie*, vol. 38, pp. 81–97, 1986.
- [41] R. K. Paul, "Untersuchungen zur Blutschädigung durch laminare Strömung im Couette-System," RWTH Aachen, 2000.
- [42] M. Giersiepen, L. J. Wurzinger, R. Opitz, and H. Reul, "Estimation of shear-related blood damage in heart valve prostheses – in vitro comparison of 25 aortic valves," *Int J Artif Organs*, vol. 13, no. 5, pp. 300–06, 1990.
- [43] S. Klaus, R. Paul, H. Reul, K. Mottaghy, and B. Glasmacher, "Investigation of flow and material induced hemolysis with a Couette type high shear system," *Materwiss. Werksttech.*, vol. 32, no. 12, pp. 922–925, Dec. 2001.
- [44] L. Goubergrits and K. Affeld, "Numerical Estimation of Blood Damage in Artificial Organs," *Artif. Organs*, vol. 28, no. 5, pp. 499–507, May 2004.
- [45] M. S. Slaughter, "Hematologic effects of continuous flow left ventricular assist devices.," *J. Cardiovasc. Transl. Res.*, vol. 3, no. 6, pp. 618–24, Dec. 2010.
- [46] J. N. Katz, B. C. Jensen, P. P. Chang, S. L. Myers, F. D. Pagani, and J. K. Kirklin, "A multicenter analysis of clinical hemolysis in patients supported with durable, long-term left ventricular assist device therapy," *J. Hear. Lung Transplant.*, vol. 34, no. 5, pp. 701–709, 2014.
- [47] F. Pagani, A. Tautoles, G. Bhat, M. Slaughter, E. Birks, S. Boyce, S. Najjar, V. Jeevanandam, A. Anderson, I. Gregoric, R. Delgado, K. Leadley, K. Aaronson, J. Rogers, and C. a Milano, "Heartware HVAD for the Treatment of Patients with Advanced Heart Failure Ineligible for Cardiac Transplantation: Results of the ENDURANCE Destination Therapy Trial," ISHLT Conference, Nice, 2015.
- [48] M. H. Kroll, J. D. Hellums, L. V. Mcintire, A. I. Schafer, J. L. M. Updated, A. Society, W. Dc, and T. A. Society, "Platelets and shear stress," *Blood*, vol. 88, no. Review article, pp. 1525–1541, 1996.
- [49] J. D. Hellums, "1993 Whitaker Lecture: biorheology in thrombosis research.," *Ann. Biomed. Eng.*, vol. 22, no. 5, pp. 445–55, 1994.

- [50] P. Hochareon, K. B. Manning, A. a. Fontaine, J. M. Tarbell, and S. Deutsch, "Correlation of In Vivo Clot Deposition With the Flow Characteristics in the 50 cc Penn State Artificial Heart: A Preliminary Study," *ASAIO J.*, vol. 50, no. 6, pp. 537–542, 2004.
- [51] R. Zhao, J. N. Marhefka, F. Shu, S. J. Hund, M. V Kameneva, and J. F. Antaki, "Micro-flow visualization of red blood cell-enhanced platelet concentration at sudden expansion.," *Ann. Biomed. Eng.*, vol. 36, no. 7, pp. 1130–41, Jul. 2008.
- [52] D. Bluestein, K. B. Chandran, and K. B. Manning, "Towards non-thrombogenic performance of blood recirculating devices.," *Ann. Biomed. Eng.*, vol. 38, no. 3, pp. 1236–56, Mar. 2010.
- [53] L. D. C. Casa, D. H. Deaton, and D. N. Ku, "Role of high shear rate in thrombosis.," *J. Vasc. Surg.*, no. 1, pp. 1–13, Feb. 2015.
- [54] A. Blitz, "Pump thrombosis-A riddle wrapped in a mystery inside an enigma.," *Ann. Cardiothorac. Surg.*, vol. 3, no. 5, pp. 450–71, 2014.
- [55] N. A. Mokadam, S. Andrus, and A. Ungerleider, "Thrombus formation in a HeartMate II," *Eur. J. Cardio-thoracic Surg.*, vol. 39, no. 3, p. 414, 2011.
- [56] T. Hasin, S. Deo, J. J. Maleszewski, Y. Topilsky, B. S. Edwards, N. L. Pereira, J. M. Stulak, L. Joyce, R. Daly, S. S. Kushwaha, and S. J. Park, "The role of medical management for acute intravascular hemolysis in patients supported on axial flow LVAD," *ASAIO J.*, vol. 60, no. 1, pp. 9–14, Jan. .
- [57] A. Vincentelli, S. Susen, T. Le Tourneau, I. Six, O. Fabre, F. Juthier, A. Bauters, C. Decoene, J. Goudemand, A. Prat, and B. Jude, "Acquired von Willebrand syndrome in aortic stenosis.," *N. Engl. J. Med.*, vol. 349, no. 4, pp. 343–9, Jul. 2003.
- [58] B. Steinlechner, M. Dworschak, B. Birkenberg, M. Duris, P. Zeidler, H. Fischer, L. Milosevic, G. Wieselthaler, E. Wolner, P. Quehenberger, and B. Jilma, "Platelet dysfunction in outpatients with left ventricular assist devices.," *Ann. Thorac. Surg.*, vol. 87, no. 1, pp. 131–7, Jan. 2009.
- [59] S. Crow, D. Chen, C. Milano, W. Thomas, L. Joyce, V. Piacentino, R. Sharma, J. Wu, G. Arepally, D. Bowles, J. Rogers, and N. Villamizar-Ortiz, "Acquired von Willebrand syndrome in continuous-flow ventricular assist device recipients.," *Ann. Thorac. Surg.*, vol. 90, no. 4, pp. 1263–9; discussion 1269, Oct. 2010.
- [60] U. Geisen, C. Heilmann, F. Beyersdorf, C. Benk, M. Berchtold-Herz, C. Schlensak, U. Budde, and B. Zieger, "Non-surgical bleeding in patients with ventricular assist devices could be explained by acquired von Willebrand disease.," *Eur. J. Cardiothorac. Surg.*, vol. 33, no. 4, pp. 679–84, Apr. 2008.
- [61] C. A. Siedlecki, B. J. Lestini, K. K. Kottke-Marchant, S. J. Eppell, D. L. Wilson, and R. E. Marchant, "Shear-dependent changes in the three-dimensional structure of human von Willebrand factor.," *Blood*, vol. 88, no. 8, pp. 2939–50, Oct. 1996.
- [62] H. M. Tsai, I. I. Sussman, and R. L. Nagel, "Shear stress enhances the proteolysis of von Willebrand factor in normal plasma.," *Blood*, vol. 83, no. 8, pp. 2171–9, Apr. 1994.
- [63] E. Di Stasio and R. De Cristofaro, "The effect of shear stress on protein conformation: Physical forces operating on biochemical systems: The case of von Willebrand factor," *Biophys. Chem.*, vol. 153, no. 1, pp. 1–8, 2010.
- [64] J. F. Gülich, *Centrifugal Pumps*, 1st ed. Springer-Verlag Berlin Heidelberg, 2008.
- [65] C. Pfleiderer and H. Petermann, *Strömungsmaschinen*, 6th ed. Berlin: Springer-Verlag Berlin Heidelberg, 1991.
- [66] J. F. Gülich, "Pump types and performance data," in *Centrifugal pumps*, 1st ed., Berlin: Springer-Verlag Berlin Heidelberg, 2008, pp. 39–68.
- [67] J. F. Gülich, "Pump hydraulics and physical concepts," in *Centrifugal pumps*, Berlin:

- Springer-Verlag Berlin Heidelberg, 2008, pp. 69–144.
- [68] H. E. Siekmann and P. U. Thamsen, “Ähnlichkeitsgesetze der Strömungslehre,” in *Strömungslehre für den Maschinenbau: Technik und Beispiele*, Berlin: Springer Berlin Heidelberg, 2008, p. 273.
- [69] U. Kertzscher, A. Berthe, L. Goubergrits, and K. Affeld, “Particle image velocimetry of a flow at a vaulted wall,” *Proc. Inst. Mech. Eng. Part H J. Eng. Med.*, vol. 222, no. 4, pp. 465–473, 2008.
- [70] A. Berthe, “Wandnahe Particle Image Velocimetry: Weiterentwicklung und Anwendung in der Biofluidmechanik,” 2012.
- [71] A. Berthe, D. Kondermann, C. Garbe, K. Affeld, B. Jähne, and U. Kertzscher, “The wall-PIV measurement technique for near wall flow fields in biofluid mechanics,” *Notes Numer. Fluid Mech. Multidiscip. Des.*, vol. 106, pp. 11–20, 2009.
- [72] W. Merzkirch, “Visualization of surface flow,” in *Flow Visualization*, 2nd ed., Orlando: Academic Press, Inc, 1987, p. 260.
- [73] T. Sieß, *Systemanalyse und Entwicklung intravasaler Rotationspumpen zur Herzunterstützung*. Shaker, 1999.
- [74] M. Behbahani, M. Behr, M. Hormes, U. Steinseifer, D. Arora, O. Coronado, and M. Pasquali, “A review of computational fluid dynamics analysis of blood pumps,” *Eur. J. Appl. Math.*, vol. 20, no. 04, pp. 363–397, Mar. 2009.
- [75] K. H. Fraser, M. E. Taskin, B. P. Griffith, and Z. J. Wu, “The use of computational fluid dynamics in the development of ventricular assist devices,” *Med. Eng. Phys.*, vol. 33, no. 3, pp. 263–80, Apr. 2011.
- [76] J. H. Ferziger and M. Peric, “Finite Volume Method,” in *Computational Methods for Fluid Dynamics*, 3rd ed., Berlin: Springer Berlin & Heidelberg, 2012, pp. 71–90.
- [77] M. E. Taskin, K. H. Fraser, T. Zhang, B. Gellman, A. Fleischli, K. a Dasse, B. P. Griffith, and Z. J. Wu, “Computational characterization of flow and hemolytic performance of the UltraMag blood pump for circulatory support,” *Artif. Organs*, vol. 34, no. 12, pp. 1099–1113, Dec. 2010.
- [78] H. K. Versteeg and W. Malalasekera, “Turbulence and its modeling,” in *An Introduction to Computational Fluid Dynamics: The Finite Volume Method*, 2nd ed., Harlow: Pearson Education Limited, 2007, pp. 90–114.
- [79] B. Su, L. P. Chua, T. M. Lim, and T. Zhou, “Evaluation of the impeller shroud performance of an axial flow ventricular assist device using computational fluid dynamics,” *Artif. Organs*, vol. 34, no. 9, pp. 745–59, Sep. 2010.
- [80] F. R. Menter, “Two-equation eddy-viscosity turbulence models for engineering applications,” *AIJA J.*, vol. 32, no. 8, pp. 1598–1605, Aug. 1994.
- [81] M. Grigioni, C. Daniele, U. Morbiducci, G. D’Avenio, G. Di Benedetto, and V. Barbaro, “The power-law mathematical model for blood damage prediction: analytical developments and physical inconsistencies,” *Artif. Organs*, vol. 28, no. 5, pp. 467–75, May 2004.
- [82] A. Garon and M.-I. Farinas, “Fast three-dimensional numerical hemolysis approximation,” *Artif. Organs*, vol. 28, no. 11, pp. 1016–25, Nov. 2004.
- [83] L. Goubergrits, “Numerical modeling of the blood damage: current status, challenges and future prospects,” *Futur. Drugs*, pp. 1–5, 2006.
- [84] M. E. Taskin, K. H. Fraser, T. Zhang, C. Wu, B. P. Griffith, and Z. J. Wu, “Evaluation of Eulerian and Lagrangian models for hemolysis estimation,” *ASAIO J.*, vol. 58, no. 4, pp. 363–72, 2012.
- [85] M. V. Kameneva, G. W. Burgreen, K. Kono, B. Repko, J. F. Antaki, and M. Umezu,

- “Effects of Turbulent Stresses upon Mechanical Hemolysis: Experimental and Computational Analysis,” *ASAIO J.*, vol. 50, no. 5, pp. 418–423, Sep. 2004.
- [86] L. Ge, L. P. Dasi, F. Sotiropoulos, and A. P. Yoganathan, “Characterization of hemodynamic forces induced by mechanical heart valves: Reynolds vs. viscous stresses,” *Ann. Biomed. Eng.*, vol. 36, no. 2, pp. 276–97, Feb. 2008.
- [87] N. J. Quinlan and P. N. Dooley, “Models of flow-induced loading on blood cells in laminar and turbulent flow, with application to cardiovascular device flow,” *Ann. Biomed. Eng.*, vol. 35, no. 8, pp. 1347–56, Aug. 2007.
- [88] I. Birschmann, M. Dittrich, T. Eller, B. Wiegmann, A. J. Reininger, U. Budde, and M. Strüber, “Ambient hemolysis and activation of coagulation is different between HeartMate II and HeartWare left ventricular assist devices,” *J. Heart Lung Transplant.*, vol. 33, no. 1, pp. 80–7, Jan. 2014.
- [89] V. Tarzia, E. Buratto, G. Bortolussi, M. Gallo, J. Bejko, R. Bianco, T. Bottio, and G. Gerosa, “Hemorrhage and thrombosis with different LVAD technologies: a matter of flow?,” *Ann. Cardiothorac. Surg.*, vol. 3, no. 6, pp. 582–584, 2014.
- [90] B. Thamsen, B. Blümel, J. Schaller, C. O. Paschereit, K. Affeld, L. Goubergrits, and U. Kertzsch, “Numerical Analysis of Blood Damage Potential of the HeartMate II and HeartWare HVAD Rotary Blood Pumps,” *Artif. Organs*, vol. 39, no. 8, pp. 651–659, 2015.
- [91] C. Y. Schüle, B. Thamsen, B. Blümel, M. Lommel, T. Karakaya, C. O. Paschereit, K. Affeld, and U. Kertzsch, “Experimental and numerical investigation of an axial rotary blood pump,” *Artif. Organs*, vol. accepted f, 2016.
- [92] B. Thamsen, R. Mevert, M. Lommel, P. Preikschat, J. Gaebler, T. Krabatsch, U. Kertzsch, E. Hennig, and K. Affeld, “A two-stage rotary blood pump design with potentially lower blood trauma: a computational study,” *Int J Artif Organs*, vol. accepted f, 2016.
- [93] I. Pieper, “In vitro Benchmarking Study of Ventricular Assist Devices,” Conference of the International Society for Rotary Blood Pumps (ISRBP), Dubrovnik, 2015.
- [94] K. H. Fraser, T. Zhang, M. E. Taskin, B. P. Griffith, and Z. J. Wu, “A quantitative comparison of mechanical blood damage parameters in rotary ventricular assist devices: shear stress, exposure time and hemolysis index,” *J. Biomech. Eng.*, vol. 134, no. 8, pp. 081002–1–11, Aug. 2012.
- [95] J. F. Antaki, C.-G. Diao, F.-J. Shu, J.-C. Wu, R. Zhao, and M. V. Kameneva, “Microhaemodynamics within the blade tip clearance of a centrifugal turbodynamic blood pump,” *Proc. Inst. Mech. Eng. Part H J. Eng. Med.*, vol. 222, no. 4, pp. 573–581, May 2008.
- [96] N. L. James, C. M. Wilkinson, N. L. Lingard, A. L. van der Meer, and J. C. Woodard, “Evaluation of hemolysis in the VentrAssist implantable rotary blood pump,” *Artif. Organs*, vol. 27, no. 1, pp. 108–13, Jan. 2003.
- [97] Y. Wakisaka, T. Nakatani, H. Anai, K. Araki, Y. Taenaka, and E. Tatsumi, “A Two Stage Axial Flow Pump - New Approach to Reduction of Hemolysis,” *ASAIO J.*, vol. 41, no. 3, pp. 584–7, 1995.
- [98] J. Wu, J. F. Antaki, J. Verkaik, S. Snyder, and M. Ricci, “Computational Fluid Dynamics-Based Design Optimization for an Implantable Miniature Maglev Pediatric Ventricular Assist Device,” *J. Fluids Eng.*, vol. 134, no. April 2012, p. 041101, 2012.
- [99] H. Horiguchi, T. Tsukiya, T. Nomoto, T. Takemika, and Y. Tsujimoto, “Study on the development of two-stage centrifugal blood pump for cardiopulmonary support system,” *Int. J. Fluid Mach. Syst.*, vol. 7, no. 4, pp. 142–150, 2014.
- [100] “Stereolithografie - tobaTEC; Rapid Prototyping spezialist für Stereolithographie.” [Online]. Available: <http://www.tobatec.net/stereolithografie.html>. [Accessed: 26-Feb-

- 2016].
- [101] J. F. Gülich, “Partload operation, impact of 3-D flow phenomena performance,” in *Centrifugal pumps*, 1st ed., Berlin: Springer-Verlag Berlin Heidelberg, 2008, pp. 187–256.
- [102] O. Wever-Pinzon, C. H. Selzman, S. G. Drakos, A. Saidi, G. J. Stoddard, E. M. Gilbert, M. Labedi, B. B. Reid, E. S. Davis, A. G. Kfoury, D. Y. Li, J. Stehlik, and F. Bader, “Pulsatility and the risk of nonsurgical bleeding in patients supported with the continuous-flow left ventricular assist device heartmate II,” *Circ. Hear. Fail.*, vol. 6, no. 3, pp. 517–526, 2013.
- [103] M. Vollkron, P. Voitl, J. Ta, G. Wieselthaler, and H. Schima, “Suction events during left ventricular support and ventricular arrhythmias,” *J. Heart Lung Transplant.*, vol. 26, no. 8, pp. 819–25, Aug. 2007.
- [104] N. Moazami, K. Fukamachi, M. Kobayashi, N. G. Smedira, K. J. Hoercher, A. Massiello, S. Lee, D. J. Horvath, and R. C. Starling, “Axial and centrifugal continuous-flow rotary pumps: A translation from pump mechanics to clinical practice.,” *J. Heart Lung Transplant.*, vol. 32, no. 1, pp. 1–11, Jan. 2013.
- [105] F. D. Pagani, “Continuous-Flow Rotary Left Ventricular Assist Devices with ‘3rd Generation’ Design,” *Semin. Thorac. Cardiovasc. Surg.*, vol. 20, no. 3, pp. 255–263, 2008.
- [106] “Pump Design | HeartWare.” [Online]. Available: <http://www.heartware.com/products-technology/pump-design>. [Accessed: 25-Feb-2016].

List of figures

- Figure 1: Schematic overview of the heart with the left and right ventricles and atria, the four valves and major vessels [1]. The direction of the blood flow is indicated as well: Blood from the body returns to the right heart through the vena cava, is then pumped through the lung to the left heart and further pumped into the aorta back to the tissues. 2
- Figure 2: Time courses of pressures and volumes of the left heart and aorta during two cardiac cycles [1]. At the end of diastole, the atria contract and transmit the rest of blood into the ventricles. During systole, the ventricles contract so that the atrioventricular (A-V) valve closes and pressure increases. When pressures are high enough, the aortic valve opens and blood flows into the aorta until the aortic pressure exceeds the ventricular pressure and the aortic valve closes. After that the ventricle relaxes and diastole begins again. The electrocardiogram (ECG) and heart tones are also shown. 3
- Figure 3: Normal blood pressures in the circulation [3]. Pressures in the aorta and large and small arteries are high and pulsatile between 80-120 mmHg, falling to much lower and non-pulsatile pressures in capillaries and veins. The pulmonary arteries leaving the right heart have pulsatile low pressure in the range of 10-20 mmHg. 4
- Figure 4: Distribution of left ventricular assist device (LVAD) types by year of implant, from the seventh Intermacs (Interagency Registry for Mechanically Assisted Circulatory Support) report [10]. Today, continuous flow LVADs (rotary blood pumps) are the mainly implanted devices compared to pulsatile positive displacement pumps. A further distinction is made between axial and radial (centrifugal) pumps, intracorporeal (pump implanted inside the body), paracorporeal (pump placed outside the body), and total artificial heart (TAH). 6
- Figure 5: Actuarial Survival of patients with axial or radial (centrifugal) continuous flow LVAD (rotary blood pump) or BiVAD (Bi-Ventricular Assist Device), from the seventh Intermacs report [10]. One-year survival with a rotary blood pump is around 85 % with slightly better values for radial (centrifugal) pumps. The survival rates with BiVADs are worse. 7
- Figure 6: Split view of HeartMate II (HM II) pump along with inflow and outflow cannulae [16]. The HM II is an axial rotary blood pump composed of a flow straightener, an impeller that is mechanically suspended, and a diffuser. Possible operational speeds are between 6,000 and 16,000 rpm [17]..... 8
- Figure 7: The Heartware HVAD [21]. Left: The assembled pump with the inflow cannula and the radial outlet. Right: The wide-blade radial impeller with front and rear housing. The impeller surface is tapered to create an axial hydrodynamical bearing at rotational speeds higher than 1,800 rpm. 9
- Figure 8: The HeartMate 3 (left) [24] consists of a radial impeller that is active magnetically levitated and features large gaps (0.5-1 mm). The Heartware MVAD (right) [21] has a very small axial impeller that rotates with high speeds (8,000-18,000 rpm) and uses hydrodynamic bearings in combination with passive magnetic bearings to suspend the impeller. 10
- Figure 9: Effect of hematocrit and shear rate on blood viscosity [32]. Blood is non-Newtonian and its viscosity decreases with the hematocrit and with an increasing shear rate. 12

- Figure 10: Thrombus formations in a HeartMate II pump. Left: A thrombus around the front bearing at the impeller inlet region [55]. Right: Attached thrombus formations in the second half of the blade channels and in the diffuser gap region [56]...... 15
- Figure 11: Basic construction of a centrifugal pump with a radial impeller. The main part is the rotor or impeller, which is composed of a front and rear shroud and the blades. The impeller rotates inside of the housing and is completed by a guide apparatus (here a diffuser with guide vanes). Furthermore, the common indexing of pumps according to the energy status of the fluid is depicted. 16
- Figure 12: Velocity triangles for the inlet and outlet of a blade. The absolute velocity \boldsymbol{v} is the vectorial sum of the circumferential velocity \boldsymbol{u} and the relative velocity \boldsymbol{w} . The relative velocity is tangential to the blade shape with the blade angle β to the circumferential direction. At the inlet, a non-spinning flow is commonly assumed and the index 1 is used, while the outlet is denoted with the index 2. 18
- Figure 13: Composition of the characteristic curve. The ideal pressure-flow relation is linear but losses resulting from shock in off-design points and friction have to be subtracted so that a curve emerges [65]. 19
- Figure 14: Typical characteristic curves for radial and axial pumps. Radial pumps have a flat curve while axial pumps have a steeper, almost linear curve. 19
- Figure 15: Principle of the wall-PIV method [71]: On the left hand side, the illuminated region of the fluid and three tracer particles A, B and C with the corresponding distances R are shown. On the right hand side, a representative image recorded by the camera with the corresponding particle intensities is displayed. 22
- Figure 16: Paint patterns on the surface of the impeller of a micro-axial blood pump [73]. The flow is entering the pump from the left side. One blade, the rear end of a second blade and a part of the hub are displayed. Except for the area on the hub close to the inlet and the blade, a uniform washout can be seen which is likely to correspond to a uniform wall shear stress. 23
- Figure 17: Test setup for the measurement of characteristic curves. The flow loop includes a long inlet tube to ensure fully developed inlet flow to the pump model. Pressures are measured via pressure transducers close to the in- and outlet, and flow is regulated with the help of a throttle and measured via a magnetic inductive flow sensor. An assistant pump overcomes the resistance of the flow loop at higher flow rates so that a wider range of flow rates is possible. 24
- Figure 18: Recirculation zone in the flow channels of the HVAD pump. A Line Integral Convolution (LIC) illustration of the relative velocity on a sectional view through the impeller and the volute casing of the HVAD is shown, and a detail of the right channel (right). A vortex structure is seen in every blade channel on the longer suction side of the blade. The cause for this might be the inertia of the fluid that is pushed to the short side of the blade when the impeller rotates leading to a flow separation. Furthermore, the gap leakage flow entering the blade channel might contribute to this zone. 63
- Figure 19: Flow patterns in the HMII. A vortex can be seen in the space between the flow straightener and the impeller at the housing wall. This results from a backflow from the impeller inlet and gap region. Another vortex is found close to the hub in the diffuser which might be caused mainly by the rapid decrease of the flow cross-section in this area. 64

Figure 20: Two miniature axial pumps in series operation [97]. Wakisaka et al showed that two axial pumps in series have a substantially lower hemolysis index (<50 %) compared to one axial pump in the same operating point.	66
Figure 21: Overview of objectives considered the development of a multistage rotary blood pump. While a good hemocompatibility was the main objective, a physiologic performance, anatomic fit, a manageable complexity as well as good manufacturability were also required.	67
Figure 22: Two-stage pump design with an axial and a radial stage that rotate in opposite directions. Such design configurations were evaluated in the early stage of the development of a multi-stage blood pump.....	69
Figure 23: Power balance of centrifugal pumps (radial and diagonal) in their best efficiency point depending on the specific speed [65]. Diagonal pumps with a specific speed of around 50 generate highest effective outputs and are therefore the most frequently used types.	70
Figure 24: Schematic design of the hydrodynamic parts of the two-stage blood pump. In this sectional view the blade edges have been projected to the view plane so that the flow channel becomes apparent.....	71
Figure 25: Stereolithography fabricated pump parts that were used for measuring the characteristic curves. The surface of the models was manually finished with sand paper in preparation of the measurements.....	72
Figure 26: A: Time course of aortic pressure (AoP) and left ventricular pressure (LVP) during two cardiac cycles of a heart failure patient. B: Typical flat characteristic curve of a radial pump. C: Typical steep characteristics of an axial pump. D: Translation of different hydrodynamic characteristic to pump output during two cardiac cycles [105]. The flatter slope of radial pumps translates into a higher pulsatility of the volume flow.....	73
Figure 27: Measured characteristic curves of the two-stage pump model for different dynamic viscosities.....	74
Figure 28: Bearing concepts used to suspend the rotor of the HVAD. Left, upper: The tapered upper surface of the impeller creates a hydrodynamic bearing [106]. Lower: Working principle of an axial hydrodynamic bearing, adapted from [104]. Right: passive magnetic bearing in the HVAD. [106]	75
Figure 29: Parts of a prototype of the two-stage pump for in-vitro measurements of blood damage. The two-part impeller was milled from titanium, the housing was composed of six different parts made from plastics (polymethyl methacrylate) and stainless steel.....	76

List of tables

Table 1: Pump components and designs [66].....	20
Table 2: Possible design configurations for a two-stage rotary blood pump. The permutations were evaluated using -, 0, or + meaning bad, neutral or good properties, respectively.	68